SEASONAL AIR AND WATER MASS REDISTRIBUTION AND ITS EFFECT ON SATELLITE AND POLAR MOTION

APPROVED BY DISSERTATION COMMITTEE:

Clark R. Wilson, Chairman

Mark P. Cloos

David Sandwell

Bob E. Schutz

Douglas Smith

Certainly, it is heaven upon earth to have a man's minde move in charitie, rest in providence, and turne upon the poles of Truth.

Francis Bacon, *The Essayes*

Dedicated to my parents and

to my wife, Gay Nell

SEASONAL AIR AND WATER MASS REDISTRIBUTION AND ITS EFFECT ON SATELLITE AND POLAR MOTION

by

Roberto Gutiérrez, B.S.

DISSERTATION

Presented to the Faculty of the Graduate School of

The University of Texas at Austin

in Partial Fulfillment

of the Requirements

for the Degree of

Doctor of Philosophy

THE UNIVERSITY OF TEXAS AT AUSTIN

DECEMBER, 1990

Acknowledgements

This work was supported by NASA Crustal Dynamics Project Grant NAG5–756, NASA Minority Training Grant NGT–70029 and a NSF Minority Graduate Fellowship. I thank Richard Eanes and Cheng Minkang of the UT Center for Space Research for the Lageos and Starlette orbital data and their critical comments. I also thank John Kuehne for his comments on spectral analysis and polar motion, and his water storage data; Eric Benedict for his work on the wind stress ocean model; John Wahr for providing the NMC air pressure data; and Jeff Corrigan for being student editor of this dissertation. I would also like to express graditude for the support of other graduate students; especially Steve Dworkin, Karen Carter, Karen Havholm, Jeff and Mary Crabaugh, and Denise Apperson. And of course, I wish to acknowledge the help and patient guidance provided by Clark Wilson.

SEASONAL AIR AND WATER MASS REDISTRIBUTION AND ITS EFFECT ON SATELLITE AND POLAR MOTION

Publication No._____

Roberto Gutiérrez, Ph.D.

The University of Texas at Austin, 1990

Supervisor: Clark R. Wilson

The laser geodetic satellites Lageos and Starlette exhibit residual orbital motion with an unexplained seasonal component. In addition, recognized polar motion excitation sources do not account for a large portion of observed polar motion. It is hypothesized that air and ocean mass redistribution is the primary source of seasonal perturbations in satellite motion, and that wind–driven ocean mass redistribution is a major source for polar motion excitation.

Average monthly variations in zonal spherical harmonic geopotential coefficients are estimated from NMC air pressure for 1958 through 1973, and from variations in continental water storage predicted by a global hydrologic model. These coefficients are used to predict average monthly perturbations in the longitude of the ascending node (Ω) for Lageos and Starlette, and in the eccentricity vector (Ψ) for Starlette. WMO monthly air pressures and twice–daily Navy sea level pressures are used to predict time series of Ω and Ψ perturbations for Lageos during 1976 through 1985, and for Starlette during 1980 through 1983. In addition, the Hellerman and Rosenstein wind stress

field for world oceans and the Gill–Niiler bottom pressure equation are used to estimate annual and semi–annual ocean mass redistribution, and to predict polar motion excitation vectors and Lageos Ω perturbations.

Comparison of predicted Ω and Ψ perturbations with observed Lageos and Starlette behavior indicate that air pressure may be responsible for much of the unmodeled seasonal variation in the Earth's geopotential. In contrast, the water storage contribution is very small. Year–to–year variability in the observed Lageos and Starlette Ω times series is well matched by predicted perturbations. Even after the removal of annual and semi–annual components, significant coherence remains between predicted and observed Ω time series for both Lageos and Starlette at periods of less than one year. Comparison of predicted polar motion with ILS observations suggest that the effect of ocean mass redistribution is significant, and second only to air pressure in magnitude. Lageos Ω perturbations predicted from ocean mass redistribution indicate that non–isostatic sea level fluctuations should be readily observable by satellite laser ranging.

Table of Contents

1. Introduction

Over the past 20 years, space geodetic techniques such as satellite laser ranging (SLR; see appendix A) and Very Long Baseline Interferometry (VLBI) have advanced to the point where phenomena such as the relativistic effects of the Earth's mass and the motion of ground stations due to plate tectonics are directly detectable. A major advantage of systems like VLBI and SLR over conventional geodetic techniques is their sensitivity to global–scale phenomena. Satellite behavior is, in large part, a response to the total mass distribution of the Earth, and changes in mass distribution are perceptable as perturbations in the satellite's expected motion. Likewise, highly accurate measurements of Earth orientation and rotation from VLBI and SLR reflect the distribution of the Earth's mass, torques exterted by winds and ocean currents on the Earth's topography, and the angular momentum of the atmosphere and oceans. This dissertation addresses several current problems in geodesy: the excitation of annual polar motion, the seasonal perturbation of laser geodetic satellites, and the response of the oceans to seasonal changes in winds and atmospheric pressure. The work described here is an investigation of the effects of the seasonal redistribution of air and water mass on geopotential and Earth orientation, and the evaluation of these predicted effects against observed satellite orbit perturbations and the Earth's observed polar motion.

The orbits of the laser geodetic satellites Lageos and Starlette have been analyzed at the University of Texas Center for Space Research for a number of years using very comprehensive force and measurement models (see sections 2.3, 3.3.3 and Appendix A). Nonetheless, the residual orbital motion, the difference between the observed and

predicted satellite motion, of both satellites exhibit coherent seasonal perturbations that are currently unexplained. The first part of this dissertation is a discussion of the nature of this residual orbital motion and the contribution that atmospheric mass redistribution and continental water storage may make to satellite motion.

Computing gravity fluctuations due to atmospheric mass redistribution involves the ocean response to changes in atmospheric pressure. The conventional hypothesis is that the oceans respond isostatically (or like an inverted barometer) to variations in air pressure: sea level is depressed 1 cm for each 1 mbar rise of air pressure, and rises 1 cm for each 1 mbar fall in pressure. The inverted barometer model assumes that regional air pressure variations induce flow between oceans, and thus force a global re–adjustment of sea level. The inverted barometer response averages out horizontal bottom pressure gradients, although bottom pressure will vary as the fraction of total air mass over the oceans varies. The available sea level data are not adequate to decisively test the inverted barometer model; therefore it's of interest to compare observed satellite residual motion to predicted satellite motion computed first from an unmodified air pressure field (i.e. non–isostatic or "rigid" oceans), and then computed from an air pressure field adjusted for the isostatic ocean response.

Average monthly surface air pressures are used to compute the seasonal perturbations in the Earth's geopotential assuming both rigid and isostatic oceans. Seasonal perturbations in geopotential are also computed from average monthly fluctuations in continental water storage. Orbital perturbations of Lageos and Starlette, predicted from these geopotential variations, are compared to observed average seasonal perturbations of these two satellites. Predicted annual Lageos and Starlette orbital perturbations estimated assuming rigid oceans are quite comparable to the observed annual pertubations, and are in better agreement with observations than the

isostatic ocean predictions. The isostatic response reduces the amplitude of the predicted satellite residuals by about a factor of 2 compared to the non–isostatic ocean prediction. The semi–annual component of residual satellite motion is poorly matched by the air pressure predictions. The contribution of water storage to the gravity field and satellite motion is very much smaller than air mass at the annual period, but of comparable size at the semi–annual. This comparison indicates that air mass redistribution is responsible for a large part of the currently unmodeled annual variation in Earth's gravity field and the resulting annual component of residual satellite motion.

The second part of the dissertation is a more detailed examination of the relationship between air mass and the satellite behavior. Air pressure data from 1976 through 1985 is used to compute time series of residual orbital motion for Lageos and Starlette. The inter– and intra–annual variability of the air pressure derived time series are compared to observed Lageos behavior for 1976 through 1985, and with Starlette observations during 1980 through 1983. The agreement between the observed and predicted satellite perturbations for individual years is very good for that component of orbital motion influenced by the even zonal geopotential coefficients. Agreement is poorer for the odd zonal contribution to orbital motion, especially for Starlette. The non–isostatic ocean predictions of satellite motion are in better agreement with the observations than the isostatic ocean predictions.

The good agreement between predicted satellite orbit residuals for a non–isostatic ocean and the observed satellite motion implies that the inverted barometer effect is at least partially compensated for by a non–isostatic redistribution of ocean mass. To test this hypothesis the seasonal variation in non–isostatic sea level due to Ekman transport is estimated. Ekman transport is the water movement in the upper portion of the water column driven by wind stress and the Coriolis force. The net transport in the Ekman

layer is 90° to the wind stress direction, and is to the right in the Northern Hemisphere and to the left in the Southern Hemisphere. Because of Ekman transport, ocean water tends to diverge from regions of low air pressure and converge toward regions of high pressure. The seasonal variations in wind stress–driven sea level are computed using the bottom pressure equation described by Gill and Niiler [1973] and the average monthly wind stress field of Hellerman and Rosenstein [1983]. The Gill–Niiler bottom pressure equation relates Ekman flow in the upper portion of the water column to changes in ocean bottom pressure; a 1 mbar change in bottom pressure is equivalent to a 1 cm change in non–isostatic sea level.

The third part of the dissertation is an examination of the role that non–isostatic ocean mass redistribution has on Earth wobble and satellite motion. The Earth's rotational axis is not fixed with respect to the Earth. The pole position, the intersection of the rotation axis with the Earth's surface, exhibits a fairly circular motion, and is composed of two major components: an annual motion and the 14–month period Chandler wobble. Annual polar motion is a forced wobble with an amplitude of about 3 m (0.10 arcsec) on the Earth's surface [Lambeck, 1980]. The Chandler wobble is a resonant motion associated with the Earth's elastic properties and its oblateness. Only the annual motion will be examined in this dissertation. A number of excitation sources for the annual wobble have been identified, including the seasonal redistribution of air mass, the horizontal pressures exerted by winds on topography and variations in continental water storage. An additional polar motion excitation source is the seasonal movement of ocean mass; however previous estimates for the annual wobble excitation due to the seasonal wind–driven ocean mass redistribution are rather small [O'Connor, 1980; Wahr,1983]. Summing all estimated polar motion sources still leaves a large portion of the observed polar motion unexplained.

The excitation in annual polar motion, and the average annual and semi–annual orbital perturbations for Lageos are estimated from non–isostatic sea level fluctuations. Predicted annual polar motion excitation is significantly larger than the earlier estimates of O'Connor and Wahr. Comparision of predicted and observed annual polar motion excitation suggest that the effect of ocean mass redistribution is significant and second only to air pressure in magnitude. The size of the predicted annual and semi–annual Lageos orbital perturbations indicate that variations in non–isostatic sea level should be readily observable by satellite laser ranging and may offset the inverted barometer effect.

If air and ocean mass redistribution is indeed responsible for most of the seasonal residual motion of Lageos and Starlette, then there are several important implications and potential applications. The possiblity exists to refine satellite force models, and thus increase the accuracy of orbit determination, by adding a time–variable component, derived from meteorological data, to the conventional Earth geopotential model. Conversely, orbit residuals could be used to estimate the global distribution of air and ocean mass. Monitoring long–term change in the atmosphere and ocean using satellite laser ranging could be important for evaluating such events as global warming and may provide fundamental constraints on future atmospheric and ocean models. Because SLR does not respond to the steric (thermal and haline) component of sea level change, we may eventually be able to separate the components of sea level change by combining satellite laser ranging with sea surface radar altimetry.

2. Seasonal Air and Water Mass Redistribution Effects on Lageos and Starlette

Abstract. We compute zonal geopotential coefficients from average seasonal variations in global air and water mass distribution. These coefficients are used to predict the seasonal variations of Lageos' and Starlette's orbital node, $\delta\Omega$, and the seasonal δJ_3 for Starlette. A comparison of these predictions with the observed values indicates that air pressure and, to a lesser extent, water storage may be responsible for a large portion of the currently unmodeled variation in the Earth's gravity field.

2.1 Introduction

Over the past ten years, observations of the geodetic satellites Starlette and Lageos have increased knowledge of the earth's gravity field and provided information on basic earth parameters such as mantle anelasticity [Merriam,1985] and mantle viscosity [Peltier,1985]. The unique designs of Lageos and Starlette, developments in laser ranging and in the measurement of UT1, and the increasing sophistication of satellite force and measurement models make possible satellite ephemerides precise enough to detect faint changes in the Earth's rotation and gravity field. Although the force models used in orbit analysis attempt to incorporate all the important influences on satellite motion, orbit residuals persist and the identification of the sources of these residuals is a current problem. We demonstrate that seasonal variations in global water and atmospheric mass distribution are a likely source for a large portion of the annual and semi-annual orbit residuals for Lageos and Starlette. Observed seasonal perturbations of Lageos' ascending node and variations in the second and third degree geopotential

coefficients estimated from Starlette agree well with variations predicted from seasonal changes in global water storage and air pressure.

2.2 Theory

An orbit is conventionally described by Keplerian orbit elements: the semi-major axis of the orbit (a), the orbit eccentricity (e), the orbit's inclination (i) with respect to the equatorial plane, the argument of the perigee (ω), and the longitude of the ascending node (Ω); see Figure 2.1 and Table 2.1. The intersections of the orbit with the equatorial plane are the orbital nodes; the ascending node is passed as the satellite moves northward. The angle ω is measured from the ascending node to the satellite's perigee. Ω is measured from the direction of the Vernal Equinox to the ascending node.

The Earth's gravity field may be expressed as a sum of spherical harmonic functions with coefficients in the expansion denoted usually as C_{lm} and S_{lm}, where l and m denote degree and order. For an Earth-orbiting satellite, those terms of degree greater than 1 will cause both secular and harmonic variations in satellite orbital elements. The even zonal terms ($l \geq 2$, $m = 0$) cause the satellite's nodes to precess. The precession rate, $d\Omega/dt$, is proportional to a weighted sum of the even zonal terms. Using the conventional notation for zonal harmonics, $C_{l,0} = -J_l$:

$$\frac{d\delta\Omega}{dt} = -n \cos i \,.(\delta J_2 f_2 + \delta J_4 f_4 + \delta J_6 f_6 + \ldots) \qquad (2.1)$$

$$f_2 = (R_e/a)^2 . \frac{3}{2} . \frac{1}{(1- e^2)^2}$$

$$f_4 = (R_e/a)^4 . \left(\frac{105}{16} \sin^2 i - \frac{15}{4}\right) . \frac{(1+ 3e^2/2)}{(1- e^2)^4}$$

$$f_6 = (R_e/a)^6 . \left(\frac{105}{16} - \frac{945}{32} \sin^2 i + \frac{3465}{128} \sin^4 i\right) . \frac{(1+ 5e^2 + 15e^4/8)}{(1- e^2)^6}$$

where $\delta\Omega$ is the node residual, δJ_l is the variation in the l^{th} degree zonal coefficient, n is $2\pi/P$, P being the orbital period, and R_e is the earth equatorial radius [Kaula, 1966]. The eccentricity, e, and the argument of the perigee, ω, are perturbed by the odd zonal harmonic terms. An expression describing the perturbation of e and ω for the case of an orbit with small e can be written using the complex variable $\Psi = e \exp(-j\omega)$ where j is the imaginary unit [Yoder et al., 1983].

$$\frac{d\Psi}{dt} + j\dot{\omega}_0 p \approx n\,(\delta J_3 f_3 + \delta J_5 f_5 + \delta J_7 f_7 + \dots) \tag{2.2}$$

$$\dot{\omega}_0 \approx n\,(R_e/a)^2.(3 - \frac{15}{4}\sin^2 i\,)\,J_2$$

$$f_3 = (R_e/a)^3.(\frac{3}{2}\sin i - \frac{15}{8}\sin^3 i\,).\frac{1}{(1-e^2)^2}$$

$$f_5 = (R_e/a)^5.(-\frac{15}{8}\sin i + \frac{105}{16}\sin^3 i - \frac{315}{64}\sin^5 i\,).\frac{(2+3e^2/2)}{(1-e^2)^4}$$

$$f_7 = (R_e/a)^7.(\frac{35}{16}\sin i - \frac{945}{64}\sin^3 i + \frac{3465}{128}\sin^5 i - \frac{15015}{1024}\sin^7 i\,).\frac{(3+15e^2/2+15e^4/8)}{(1-e^2)^6}$$

$\dot{\omega}_0$ is the average precessional rate of the perigee.

The expression for $d\Psi/dt$ is a linear function of the harmonic coefficients of the gravity field, hence a set of odd zonal coefficients is equivalent to the weighted sum we define as:

$$\delta J_O(\Psi) = \frac{1}{f_3}\,.\,(\delta J_3 f_3 + \delta J_5 f_5 + \delta J_7 f_7 + \dots) \tag{2.3}$$

Customarily, satellite orbit residuals are fit by least squares to a force model in which only J_2 and J_3 are allowed to vary. This, in effect, forces all even degree zonal variation to contribute to an apparent δJ_2 and all odd degree zonal variation to an apparent δJ_3. Here we assume that δJ_O is this apparent δJ_3. Thus, we may compute δJ_O from observations of global air and water distribution and compare its value with δJ_3 determined from laser ranging to Starlette.

TABLE 2.1 Orbit Parameters

satellite	a (km)	e	i (deg)	P (hr)
Lageos	12270.0	.0044	109.94	3.758
Starlette	7330.0	.020	49.8	1.735

TABLE 2.2 Observed and Predicted $\delta\Omega$ Residual in milliarc sec

	Annual		Semi-annual	
	cos	sin	cos	sin
Lageos				
observed (1976-81)	12.2	-13.8	-2.6	-4.4
non-isostatic ocean	15.9	-5.2	0.5	-3.8
isostatic ocean	7.9	-5.5	0.5	-2.3
water storage only	-0.7	1.1	0.9	-0.5
Starlette				
observed (1976-77)	-299.5	-15.6	-65.1	97.6
(1983-84)	-362.4	-50.7	-6.7	29.5
non-isostatic ocean	-133.9	8.3	-22.4	28.4
isostatic ocean	-55.9	56.6	-13.6	12.9
water storage only	8.7	-16.1	-13.5	10.2

Solar angle = 0° on 1 January

TABLE 2.3 Observed δJ_3 and Predicted δJ_O in cm water

		Annual		Semi-annual	
		cos	sin	cos	sin
Starlette					
δJ_3	(1976-77)	-7.05	-0.38	2.16	-2.85
	(1983-84)	-2.05	-2.26	0.71	0.52
$\delta J_O(\Psi)$		-1.29	-0.22	-1.73	0.89

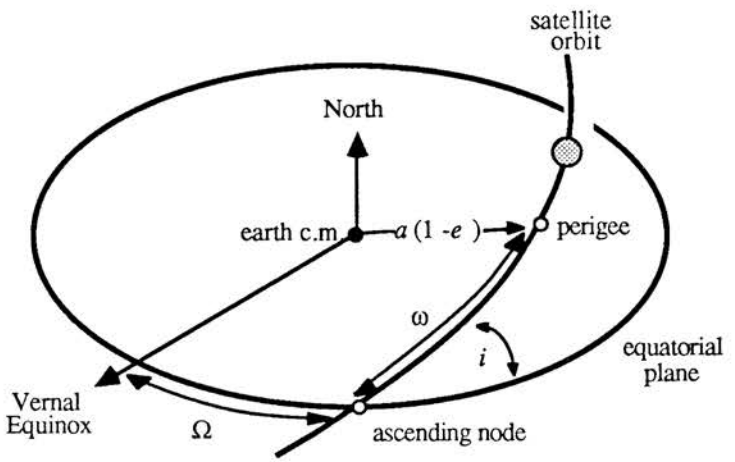

Figure 2.1. The geometrical relationships of the Keplerian orbital elements: the satellite orbit is an ellipse with semi-major axis a, eccentricity e, and with the earth occupying one of the foci. The argument of the perigee, ω, is measured from the ascending node to the satellite's point of closest approach to the earth. The distance from the earth's center of mass to the perigee is $a(1 - e)$. The orientation of the satellite's orbit is determined by the longitude of the ascending node, Ω, measured from the direction to the Vernal Equinox, and the inclination, i .

2.3 Data

The average seasonal air pressure variations were estimated from 180 months of monthly mean surface pressure data taken at individual stations from May, 1958 to April, 1973 and compiled by the National Meteorological Center. A mean station pressure was subtracted from observed pressure and the residual pressure variations were then interpolated onto a 5° longitude by 2.5° latitude global grid [Wahr, 1983].

The average monthly change in water storage was estimated for all land areas, excluding Antarctica. The global land area was divided into nearly 600 drainage basins defined on a 1° by 1° grid. An average seasonal water storage time series was then estimated for each basin using about 1.6 million station-months of mean monthly precipitation observations collected at over 4000 stations from 1900 to the present. The major data source was the National Center for Atmospheric Research (NCAR) mean monthly climatology tape, supplemented with unpublished Chinese records.

Within each basin, total annual precipitation (P_{ann}) is the sum over the 12 months of average monthly precipitation (P_{mon}); total annual runoff (R_{ann}) is P_{ann} scaled by an annual runoff coefficient.; total annual evapotranspiration (E_{ann}) is P_{ann} minus R_{ann}, assuming no net water storage change on average. For each basin, a runoff coefficient and the fraction of total annual evapotranspiration (e_{mon}) and of runoff (r_{mon}) for each month were read from the UNESCO Atlas of World Water Balance [1978]. Therefore, the mean monthly change in water storage is:

$$\Delta S_{mon} = P_{mon} - r_{mon} R_{ann} - e_{mon} E_{ann}$$

Satellite orbital variations are taken from two sources. Yoder et al.[1983] presented an analysis of 5.5 years of Lageos laser range data from May, 1976 to December, 1981. The range data were fit with a dynamical orbit model that incorporated the gravitational effects of the earth, Sun, Moon and planets, the effects of

atmospheric drag and solar radiation pressure, and tidal perturbations including the effects of a nominal annual and semi-annual tide. Table 2.2 gives the annual and semi-annual variations in the $\delta\Omega$ residual as reported by Yoder et al. [1983].

Workers at the University of Texas Center for Space Research have computed several one year arcs from Starlette range data, estimating δJ_2, δJ_3 and the $\delta\Omega$ residual for each year. The annual and semi-annual variations in the $\delta\Omega$ residuals for 1976-1977 and 1983-1984 are shown in Table 2.2 and the δJ_3 annual and semi-annual components are shown in Table 2.3 [M. K. Cheng et al., 1989].

2.4 Data Analysis

Unnormalized zonal spherical harmonic coefficients were estimated for each of the 12 months from the surface air pressure and water storage data. These coefficients, in centimeters of water (a pressure change of 1 millibar = 1 cm water), were then translated into unnormalized geopotential coefficients using the relationship:

$$J_l = -\frac{4\pi G\rho_w}{g} \cdot \frac{1 + k_l'}{2l + 1} \cdot a_{l,0}$$

where G is the gravitational constant, g is the average gravitational acceleration, ρ_w is the density of water and k_l' is the surface load deformation coefficient or Love load number [Longman,1963]. Monthly values for $d\delta\Omega/dt$ and $\delta\Omega$ were then predicted for Lageos and Starlette from the air pressure and water storage zonal coefficients using equation 2.1 and the orbit parameters in Table 2.1. Annual and semi-annual sinusoidal components were then fit for comparison with the values of Table 2.2. In addition δJ_O, expressed in centimeters of water, was computed using equations 2.2 and 2.3 for comparison with δJ_3, estimated from Starlette.

If oceans respond isostatically to changes in atmospheric pressure, sea level will be depressed as local atmospheric pressure rises. This so-called inverted barometer behavior means that the net change in pressure at the ocean bottom is the average atmospheric pressure change over all oceans [Jeffreys, 1916]. Similarly, in an isostatic ocean, the water received in any ocean basin will be distributed uniformly over all oceans. The isostatic ocean assumption appears to be reasonable for annual and semi-annual periods but it has not been proven conclusively to be correct and it would be desirable to test its validity.

The water storage estimates were, by necessity, based on an isostatic ocean model; water losses from land were accompanied by uniform increases in overall ocean water levels and vice-versa. For the air mass contribution it was possible to do the calculation in two ways because surface pressure data were available over both ocean and land areas. For the isostatic ocean (inverted barometer) calculation, average surface air pressure over all the oceans was calculated and substituted for the observed pressure at each ocean grid point. The non-isostatic ocean calculation for the air mass effect was performed simply by using grid point values for air pressure.

2.5 Results and Discussion

In Table 2.2 the predicted annual and semi-annual Lageos and Starlette $\delta\Omega$ residuals for both the non-isostatic and isostatic ocean cases are shown below the observed amplitudes. In Figures 2.2 and 2.3 observed and predicted Lageos and Starlette $\delta\Omega$ are plotted in a coordinate system where the cosine and sine components are the horizontal and vertical components of a vector. There is good agreement between observed and predicted annual Lageos $\delta\Omega$ residuals: the non-isostatic ocean prediction explains 90% of the amplitude of the observed $\delta\Omega$ and differs in phase by

31°. The isostatic ocean prediction accounts for 52% of the observed annual amplitude and differs by only 14° in phase. The agreement between the observed and predicted Lageos semi-annual $\delta\Omega$ residuals is poorer: the non-isostatic estimate has 75% of the amplitude and agrees to within 39° in phase. The isostatic ocean estimate contains 47% of the amplitude and differs by 43 ° in phase.

The agreement between observed Starlette $\delta\Omega$ residuals and the non-isostatic prediction of $\delta\Omega$ is poorer in amplitude but better in phase than for Lageos: the non-isostatic prediction of $\delta\Omega$ accounts for only 45-37% of the observed amplitude (1976-77 vs. 1983-84) but differs in phase by just 7°-12°. The non-isostatic Starlette semi-annual $\delta\Omega$ explains 31-120% of observed amplitude and only differs by 4°-25° in phase. For the isostatic case, the predicted Starlette annual $\delta\Omega$ accounts for 26-22% of the observed amplitude and diverges in phase by 48°-53°. The isostatic Starlette semi-annual $\delta\Omega$ accounts for only 16-62% of the observed amplitude and differs in phase by 13°-34° from the observed.

Also shown in Table 2.2 is the water storage contribution to the predicted Lageos and Starlette $\delta\Omega$. At the annual frequency, predicted water storage effects on $\delta\Omega$ are only 7 to 12% (Lageos non-isostatic vs. isostatic case) or 6 to 16% (Starlette) as large as the air pressure effects and nearly opposed in phase. Water storage is a major component of the semi-annual predicted $\delta\Omega$ with amplitude of 30 to 52% (Lageos) or 60 to 100% (Starlette) of the air pressure contribution.

In Table 2.3 the annual and semi-annual δJ_O determined for the Starlette orbit are shown below the observed Starlette δJ_3. Figure 2.4 shows Starlette δJ_3 and δJ_O plotted in the same manner as the $\delta\Omega$ residuals. The annual δJ_O agrees with the annual δJ_3 components in phase but has only about a third of the observed amplitude. The

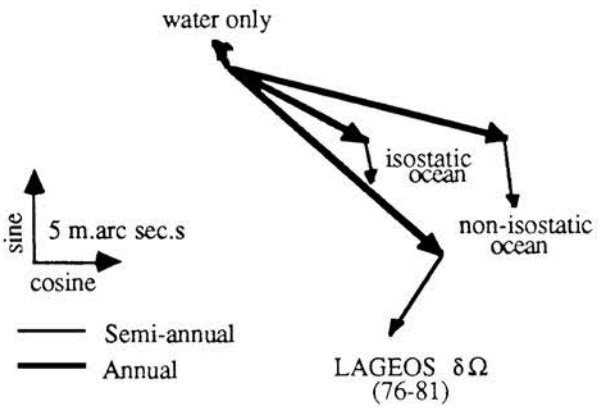

Figure 2.2. The cosine and sine terms of the observed and predicted Lageos $\delta\Omega$ residual are plotted as vector components; cosines horizontally with increasing positive values toward the right and sines vertically with increasing positive values upward. The annual and semi-annual components are shown as heavy lines and thin lines respectively. The scale bars indicate 5 milliarc sec.

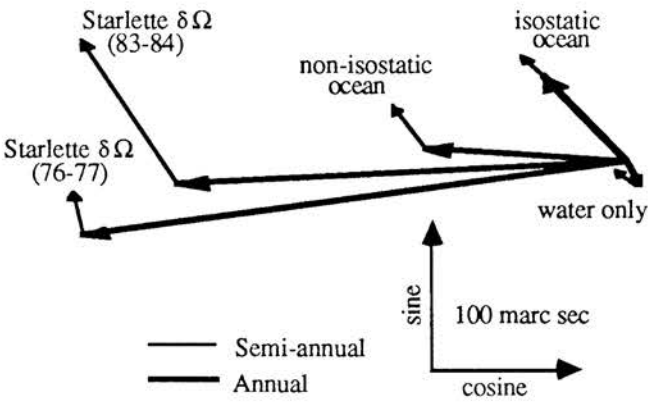

Figure 2.3. The cosine and sine terms of the observed and predicted Starlette $\delta\Omega$ residual are plotted as in Figure 2.2. The scale bars indicate 100 milliarc sec.

observed semi-annual δJ_3 and semi-annual δJ_O are comparable in amplitude but are well out of phase; semi-annual δJ_O differ in phase from δJ_3 by about 90° to 180°.

The predicted $\delta\Omega$ and δJ_O were computed from 15 years of surface air pressure and over 80 years of precipitation records. In contrast, the observed values were derived from considerably shorter time series; 1 year arcs for Starlette and a 5.5 year arc for Lageos. Thus, year to year variablities in meteorological parameters, which are largely averaged out in the predicted values, will still contribute to the observed satellite values. Hence, part of the disparity between Starlette's predicted $\delta\Omega$ and δJ_O and observed $\delta\Omega$ and δJ_3 is likely to be due to this effect. The longer Lageos arc tends to average out this variability, and shows better agreement with predictions from long-term average meteorological data.

An additional source of apparent discrepancy comes from the use of monthly mean meteorological data. We suspect that, with monthly data, the phase of the sinusoidal components may be uncertain by as much as 1 month, which translates into ±15° for the annual and ±30° for the semi-annual period. In fact, we observe larger phase discrepancies for the semi-annual.

Another factor which may lead to a discrepancy is the unknown degree to which the oceans are isostatic. The two predictions for Lageos and Starlette (Figures 2.2 and 2.3) show that this is an important question, since the amplitude and phase are strongly dependent on this assumption. Here we find better phase agreement with the inverted barometer assumption but better amplitude agreement without it for Lageos. The Starlette prediction is better, both in amplitude and phase, without the inverted barometer assumption. The question of whether the oceans are isostatic remains unsettled, but future studies similar to this one may resolve the issue.

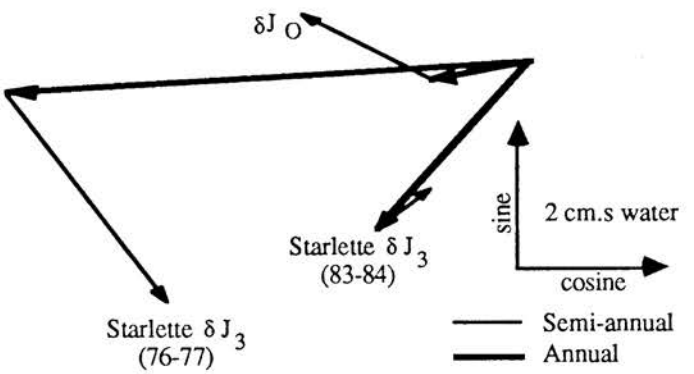

Figure 2.4. The cosine and sine terms for the observed 1976-1977 and 1983-1984 Starlette δJ_3 and estimated δJ_O are plotted as in Figure 2.2. The scale bars indicate 2 centimeters of water.

2.5 Conclusions

From the discussion, it is obvious that we could not expect precise agreements between observations and predictions. Nevertheless, several conclusions can be drawn from the above comparisons. The good agreement between observations and predictions for the annual Lageos $\delta\Omega$ suggests that seasonal water and atmospheric mass redistributions are a major part of the unmodeled annual J_2 term. As for Starlette, predicted annual $\delta\Omega$ and δJ_0 and semi-annual $\delta\Omega$ agree well in phase with observed $\delta\Omega$ and δJ_3 but there is no obvious explanation for the larger amplitude of the observed Starlette $\delta\Omega$ and δJ_3.

The poorer agreement between observed and predicted semi-annual Lageos and Starlette $\delta\Omega$ and the lack of agreement between observed and predicted semi-annual Starlette δJ_3 suggest that additional unmodeled forces are contributing to their associated orbit perturbations; incompletely modeled semi-annual earth and ocean tides are one possibility [Cheng et al., 1985]. The poor agreement of the semi-annual components may also reflect the larger contribution of water mass at this frequency. Water storage, being more complexly coupled to the seasonal meteorological cycle than air pressure, may be more variable from year to year.

3. Global Air Mass Redistribution Effects on the Laser Geodetic Satellites Lageos and Starlette

Abstract. Orbital motion of the laser geodetic satellites Lageos and Starlette exhibit residual orbital motion with a coherent seasonal component and it is hypothesized that air mass redistribution is the major source of these seasonal perturbations. Zonal spherical harmonic geopotential coefficients are computed from WMO monthly air pressure data and twice–daily Navy sea level pressures. These coefficients are used to predict a time series of the perturbation the longitude of ascending node Ω and the eccentricity vector Ψ of Lageos for 1976 through 1985. Similar time series are estimated for Starlette for 1980 through 1983. Comparison of predicted and observed Ω and Ψ time series indicate that air pressure may be responsible for much of the unmodelled seasonal variation in the Earth's gravity field. Year–to–year variability in the observed Lageos and Starlette Ω times series is well matched by the predicted perturbations. Even after the removal of annual and semi–annual components, significant coherence remains between predicted and observed Ω time series for both Lageos and Starlette.

3.1 Introduction

3.1.1 Satellite Geodesy

Over the past fifteen years, observations of the geodetic satellites Starlette and Lageos have increased knowledge of the Earth's gravity field [Cheng, 1988; Cheng et al., 1989] and provided information on fundamental Earth parameters such as mantle anelasticity [Merriam, 1985] and mantle viscosity [Peltier, 1985]. The unique design of geodetic satellites, the centimeter accuracy of satellite laser ranging (SLR), the accurate measurement of UT1 by Very Long Baseline Interferometry (VLBI), and the

increasing sophistication of satellite force and measurement models make possible satellite ephemerides precise enough to detect small changes in the Earth's orientation, length of day, and gravity field [Cheng et al., 1985; Cheng, 1988; Ries et al., 1989] and to directly measure plate tectonic motion [Tapley et al., 1985; Stolz et al., 1989; Watkins, 1990]. The force models used in orbit analysis attempt to incorporate all the significant influences on satellite motion; however, orbit residuals persist and the identification of the sources of these residuals is a current problem. The accuracy of orbit analysis has increased over the decade to the point where forces ignored when Lageos and Starlette were launched must now be addressed. These include various relativistic effects [Vincent, 1984; Ciufolini, 1986; Ries et al., 1989], the Yarkovsky effect [Vincent, 1984; Rubicam,1987] and the redistribution of air and water mass [Gutierrez and Wilson, 1987].

3.1.2 Purpose of this Study

Gutierrez and Wilson [1987] demonstrated that the average seasonal variation in global water and atmospheric mass distribution are a likely source for changes in gravitational potential which cause a significant portion of the average observed annual variations in orbit residuals for Lageos and Starlette. In a more detailed analysis, we examine here global air mass redistribution during 1976-1985 and compare the predicted variations in the orbits of Lageos and Starlette with observed residuals for the same period. Variations in geopotential due to air mass result from air redistribution within the hemispheres, especially between the mid- and high latitude bands, and between the northern and southern hemispheres. They also reflect a seasonal variation in global water vapor content of about 10^{15} kg which corresponds to a surface pressure variation of 0.2 millibar [Trenberth et al., 1987]. The average variation in the Earth's center of mass due to the variations in air pressure are extremely small, even assuming

non–isostatic oceans: about ±4 mm along the z and y–axis and no appreciable shift along the x–axis. Perturbations in Lageos's and Starlette's ascending node (Ω) predicted from air pressure variations agree well with observed node perturbations; however there is significantly less agreement between observed and predicted perturbations in the eccentricity vector (Ψ).

3.2 Theory

3.2.1 Orbit Elements

Orbits are typically described by classical or Keplerian orbital elements: the eccentricity, semi-major axis, inclination, longitude of the ascending node, argument of the periapsis and a sixth parameter describing the satellite's position in time such as the true anomaly or the mean anomaly. See Figure 3.1. The eccentricity e and semi–major axis a describe the orbit's shape; e^2 equals $(a^2 - b^2)/a^2$ where b is the semi–minor axis. The inclination i is the angle between the Earth's equatorial plane and the satellite's orbital plane. The longitude of the ascending node Ω is the angle, measured in the equatorial plane, between a fixed direction (toward the Vernal Equinox) and the point where the satellite crosses the equatorial plane in the northernly direction (the ascending node). The argument of the periapsis ω is the angle, measured in the orbital plane, between the ascending node and the perigee. The orbital period P is equal to $\mu^{-1/2}a^{3/2}$, where μ is the product of the gravitational constant and Earth's mass, GM_e. The reciprocal of the period is the mean motion n, which is equal to $2\pi/P$. The mean anomaly M is a fictitious parameter that describes the angular position at time t, of an equivalent satellite in a circular orbit of radius a. M is measured in the orbital plane and is equal to $n(t - t_0)$ where t_0 is the time when the satellite was at periapsis. Table 1 lists the orbital parameters of both Lageos and Starlette.

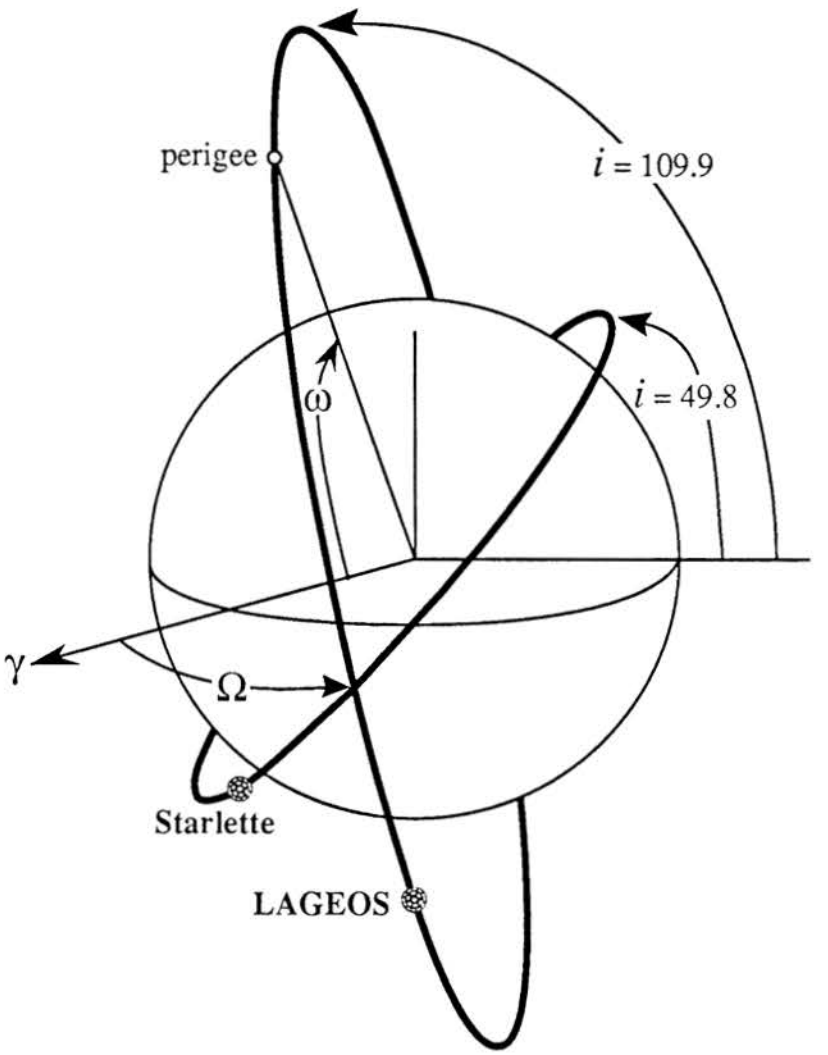

Figure 3.1. Geometric relationships of the Keplerian orbit elements and the Lageos and Starlette orbits. Ω is the longitude of the ascending node measured from γ, the direction of the Vernal Equinox, ω is the argument of the perigee and i is the inclination.

3.2.2 Orbit Perturbation Theory

In connection with satellite dynamics, the Earth's gravitational potential V may be expressed as a sum of spherical harmonic functions with coefficients in the expansion denoted as C_{lm} and S_{lm}, where l and m denote degree and order, after Kaula [1966]:

$$V = \frac{\mu}{r}\left\{1 - \sum_{l=1}^{\infty}\sum_{m=0}^{l}\left(\frac{a_e}{r}\right)^l P_{lm}(\sin\phi)\left[C_{lm}\cos m\lambda + S_{lm}\sin m\lambda\right]\right\}$$

ϕ and λ are latitude and longitude, a_e is the Earth's equatorial radius, r is the distance from the satellite to the Earth's center of mass and $P_{lm}\sin(\phi)$ are the associated Legendre functions. For an Earth-orbiting satellite, those terms of degree greater than 1 will cause both secular and periodic variations in satellite orbital elements. The even zonal terms, those C_{lm} with $l \geq 2$ and $m = 0$, cause the satellite's nodes to precess. The precession rate, $d\Omega/dt$, is proportional to a weighted sum of the even zonal terms:

$$\frac{d\delta\Omega}{dt} = \delta J_2 f_2 + \delta J_4 f_4 + \delta J_6 f_6 + \ldots \qquad (3.2.1)$$

$$f_2 = -n.(a_e/a)^2.\frac{3}{2}.\frac{1}{(1-e^2)^2}.\cos i$$

$$f_4 = -n.(a_e/a)^4.\left(\frac{105}{16}\sin^2 i - \frac{15}{4}\right).\frac{(1+3e^2/2)}{(1-e^2)^4}.\cos i$$

$$f_6 = -n.(a_e/a)^6.\left(\frac{105}{16} - \frac{945}{32}\sin^2 i + \frac{3465}{128}\sin^4 i\right).\frac{(1+5e^2+15e^4/8)}{(1-e^2)^6}.\cos i$$

where $\delta\Omega$ is the node residual, J_l equals $-C_{l,0}$, and δJ_l is a small variation in the l^{th} degree zonal coefficient [Kaula, 1966].

3.2.3 Eccentricity Vector.

If we imagine that the orbital plane defines a complex plane, with the real axis being the line of nodes and the imaginary axis being the perpendicular to the line of nodes, then we can define a complex quantity $\Psi = e\exp(-j\omega)$ where j is $-1^{1/2}$. Ψ corresponds to the vector in the complex plane with magnitude e and direction ω [Yoder

et al., 1983]. The significance of Ψ is that for satellites with small eccentricity, the odd zonal terms of the geopotential fluctuations only contribute to the real part of the Ψ excitation, $d\Psi/dt$ (see Appendix B):

$$\frac{d\Psi}{dt} \approx \delta J_3 f_3 + \delta J_5 f_5 + \delta J_7 f_7 + \ldots - j\,\dot{\omega}_0 \Psi \qquad (3.2.2)$$

$$\dot{\omega}_0 \approx n\,.(a_e/a)^2.(3 - \frac{15}{4}\sin^2 i\,)\,J_2$$

$$f_3 = n\,.(a_e/a)^3.(\frac{3}{2}\sin i - \frac{15}{8}\sin^3 i\,)$$

$$f_5 = n\,.(a_e/a)^5.(-\frac{15}{4}\sin i + \frac{105}{8}\sin^3 i - \frac{315}{32}\sin^5 i\,)$$

$$f_7 = n\,.(a_e/a)^7.3.(\frac{35}{16}\sin i - \frac{945}{64}\sin^3 i + \frac{3465}{128}\sin^5 i - \frac{15015}{1024}\sin^7 i\,)$$

$\dot{\omega}_0$ is the average precession rate of the perigee.

3.2.4 Satellite Sensitivity to Air Mass Redistribution.

Equations 3.2.1 and 3.2.2 show that the orbit parameters determine a satellite's sensitivity to the perturbing effect of individual zonal geopotential coefficients. A global air pressure field $f(\phi,\lambda)$ can be described as a sum of surface spherical harmonics with a_{lm} and b_{lm} representing the conventional (unnormalized) spherical harmonic coefficients:

$$f(\phi,\lambda) = \sum_{l=0}^{\infty}\sum_{m=0}^{l} P_{lm}(\sin\phi)\left[a_{lm}\cos m\lambda + b_{lm}\sin m\lambda\right]$$

In turn, zonal coefficients of barometric pressure can be translated into unnormalized geopotential coefficients using the relationship from McCarthy et al.[1989]:

$$\delta J_l = -\frac{4\pi G\rho_w}{g}\cdot\frac{1 + k_l'}{2l + 1}\cdot a_{l,0} \qquad (3.2.3)$$

where G is the gravitational constant and g is the average gravitational acceleration. ρ_w is the density of water since 1 mbar is equivalent to 1 cm of water. k_l' is the surface

load deformation coefficient or load Love number [Longman,1963] of degree l and includes the effect of the solid Earth response to the load.

Table 3.2 summarizes the sensitivity of Lageos and Starlette, as predicted by equations 3.2.1, 3.2.2 and 3.2.3, to the zonal terms $a_{l,0}$ of a air pressure field $f(\phi,\lambda)$. The predicted $d\Omega/dt$ and $Re(d\Psi/dt)$ due to each zonal harmonic degree is expressed in milliarcseconds (mas) $year^{-1}$ $millibar^{-1}$ (mbar) of pressure anomaly. Starlette's lower orbit makes it much more sensitive to the higher degree geopotential terms than Lageos. Unfortunately, Starlette's lower orbit also increases its sensitivity to non–gravitational influences such as atmospheric drag and Earth radiation pressure. Table 3.2 shows that Lageos' response is largely sensitive to degrees 2 through 5 while Starlette is sensitive to much higher spherical harmonic degrees.

3.3 Data

3.3.1 WMO Station Pressures

The National Center for Atmospheric Research (NCAR) climatology tape contains world monthly surface station climatological data for over 3700 World Meteorological Organization (WMO) stations. Mean monthly surface pressures and temperatures recorded from January, 1976 through December, 1985 were read from the NCAR climatology tape. These data represented sampled records from between 847 to 1141 stations during this time interval.

Inevitably some WMO station records had a month or several months missing. If a station had more than two months of data missing within a year, the data for that entire year was not used. If only one or two months were missing, then an average surface pressure (or temperature) was computed for that calender month from the other years of station data and was substituted for the missing month. For example, some far

Table 3.1 Orbit Parameters

satellite	a (km)	e	i (degees)	P (hours)
Lageos	12270.0	.0044	109.94	3.758
Starlette	7330.0	.020	49.8	1.735

Table 3.2 Lageos and Starlette Sensitivity to Air Pressure Zonals* in mas year^{-1} mbar^{-1}

	$d\Omega/dt$			Real($d\Psi/dt$)	
Even zonals	Lageos	Starlette	Odd zonals	Lageos	Starlette
2	-49.35	567.27	3	-6.15	131.47
4	-12.72	15.70	5	1.21	96.99
6	-1.96	-160.31	7	0.73	-37.17
8	-0.10	-33.61	9	0.19	-45.60
10	0.06	51.88	11	0.03	5.88
12	0.02	24.09	13	0.00	20.93
14	0.01	-16.78	15	0.00	1.98
16	0.00	-6.69	17	0.00	-9.20
18	0.00	4.47	19	0.00	-3.03
20	0.00	7.78			

*unnormalized

Table 3.3 Number of WMO Stations and Interpolated Missing Months

Year	1976	1977	1978	1979	1980	1981	1982	1983	1984	1985
WMO stations										
before interpolation:	782	796	869	826	846	669	703	704	690	507
after interpolation:	1052	1060	1141	1128	1088	951	935	957	1011	847
missing months:	399	352	352	424	330	364	334	365	440	499

northern hemisphere stations seemed to be regularly unoccupied during one or two months of each winter. For stations reporting only one year of data, values for missing months were calculated from annual and semi-annual sine and cosine functions least–squares fit to that one year of station pressure (or temperature) data.

Table 3.3 shows the number of WMO stations that were available each year, the number of WMO stations available after interpolating missing months and the number of missing months that were interpolated per year. Figure 3.2 shows the location of all WMO stations used during 1976 through 1985. There are significantly more stations in the Northern Hemisphere than in the Southern Hemisphere, and very few stations in the ocean areas, especially the South Pacific and the Antarctic regions.

WMO station pressures were adjusted to the regional elevation using the station temperature, station elevation, average elevation in the surrounding 1° x 1° block, and the relationship:

$$\text{Regional surface pressure} = \text{Station pressure} \cdot \exp(-\Delta\text{elevation} \cdot g/R \cdot T^\circ)$$

where Δelevation is the difference between the station and regional elevation, g is gravitational acceleration, R is the gas constant and T° is the temperature in Kelvin. This adjustment is appropriate for a hydrostatic atmosphere. A mean station pressure was computed from all the elevation adjusted pressure values for that station, and then subtracted creating a time series of pressure deviations from the mean, i.e. pressure anomalies, for each WMO station. The resulting set of pressure values had a zero mean and a standard deviation σ_{WMO} of 4.11 mbar.

3.3.2 Navy Sea Level Pressures

The second set of barometric pressures values consisted of twice–daily sea level pressure estimated by an atmospheric model of the Navy Fleet Numerical Oceanographic Center. These sea level pressure values were provided by NCAR on a

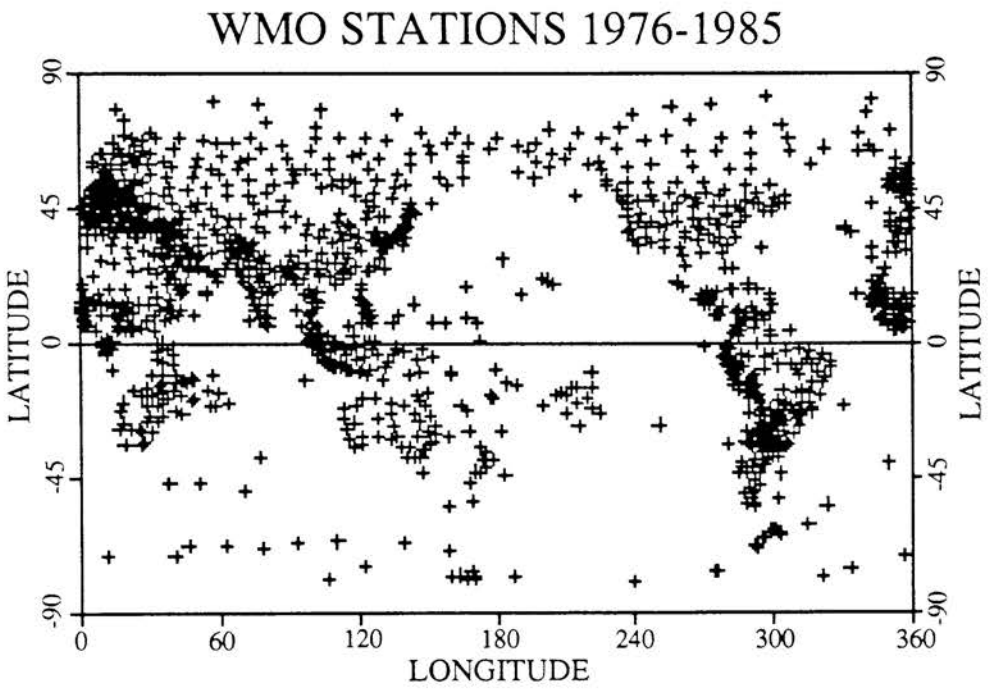

Figure 3.2. Distribution of all WMO stations used in this study for 1976 through 1985. Stations are scarce in ocean areas, especially in the southern hemisphere.

global 5° x 5° grid for the time period January, 1976 through June, 1983 with a five month gap (February–June) in 1980. The WMO and Navy pressures values are not completely independent because the WMO data are one part of the data set used to drive the Navy atmospheric model.

The sea level pressure values that fell on land, where average elevation for that 5° x 5° block is above sea level, were adjusted to the average regional elevation in the same manner as the WMO station pressures. A mean pressure was computed for each grid node, and then subtracted from all the elevated adjusted pressure values for that grid node creating a time series of pressure anomalies with a zero mean value.

3.3.3 Satellite Orbit Residual Data

Lageos and Starlette orbit residuals were generated by the University of Texas Center for Space Research (CSR). Continuous, dynamically consistent long arcs were fit to satellite laser range observations from ground-based tracking sites using the University of Texas Orbit Processor (UTOPIA) program running on a Cray X-MP/24.

For Lageos, nearly 100 stations provided over 300,000 3–minute SLR normal points spanning the period from May, 1976 through January, 1988. The long arc was fit using a dynamical force model which included the GEM–L2 geopotential model out to degree and order 20, solid Earth tides, a Lageos-derived ocean tide model based on the Schwiderski MERIT standard [Melbourne et al., 1983], the gravitational effects of the moon, sun and planets (Venus through Saturn) using the JPL DE-200 planetary ephemeris, direct solar and Earth radiation pressure, an empirical along–track acceleration ("drag") and relativistic perturbations due to the Earth. The nominal measurement model included corrections for atmospheric refraction, crustal plate motion based on the Minster–Jordan AM1-2 plate velocities [Minster and Jordan, 1978], Earth precession and nutation based on the International Astronomical Union

precession and Wahr nutation series, and Earth rotation based on the CSR's Lageos–derived series for the polar coordinates (x and y) and VLBI measurements of UT1. The resulting root mean squared (rms) error for orbit fit of the Lageos 1976–1988 long arc is 18 cm [Stolz et al., 1989]. For this study we used unsmoothed time series of orbit parameter residuals, including perturbations of Ω and Ψ, with an approximately 6–day sampling interval.

A Starlette 5–year long arc was computed using over 176,008 20–second SLR normal points from 36 tracking stations spanning 1983 through 1988. Force and measurement models similar to the Lageos models were used but with the substitution of the CSR developed PTGF–3A gravity field for the GEM–L2 and the addition of the 18.6–year lunar, the S_a, T_2, R_2, ψ_1, S_1 tides, and the 18.6–year lunar tide modulation of the K_1 and K_2 tides to the tide series. The rms orbit fit error for the Starlette 5–year long arc was 4.45m when estimating satellite state vector, and 5–day drag coefficient and global solar radiation parameters. The resulting residual series of the perturbations of Ω and Ψ had a sample interval of approximately 5 days.

3.4 Data Analysis

3.4.1 Spatial Integration of Navy Data

In analyzing global air pressure it is important to consider the ocean's response to a variation in air pressure. If the oceans respond isostatically to changes in atmospheric pressure, sea level will be depressed approximately 1 cm as local atmospheric pressure increases by 1 mbar. This so-called inverted barometer (ib) behavior means that the net change in pressure at the ocean bottom, which is a measure of the total mass of air and water overhead, is the average atmospheric pressure change over all oceans [Jeffreys,

1916]. Similarly, in an isostatic ocean the water received in any ocean basin will be distributed uniformly over all oceans.

The isostatic ocean assumption appears to be reasonable for annual and semi-annual periods, however, it would be desirable to test it observationally. Therefore, we computed unnormalized zonal spherical harmonic coefficients, degrees 2 through 20, from the adjusted Navy sea level pressure grids by numerical integration for both non–isostatic and isostatic oceans:

$$a_{l,0} = \frac{(2l+1)}{4\pi} \int_0^{2\pi} \int_0^{\pi} f(\phi,\lambda)\, P_l(\sin\phi) \cos\phi \, d\phi \, d\lambda$$

$f(\phi,\lambda)$ is the air pressure as a function of latitude and longitude and $P_l(\sin\phi)$ is the Legendre polynomial for $m = 0$. Calculating a second set of zonal coefficients using the inverted barometer assumption first involved computing an average pressure anomaly for the entire ocean area and then substituting it for the observed pressure anomaly at each ocean grid point before conducting the numerical integration. This second set of zonal coefficients is referred to as Navy inverted barometer (ib) coefficients.

3.4.2 Spatial Integration of WMO Data

Conventional zonal spherical harmonic coefficients, $a_{2,0}$ through $a_{20,0}$, were simultaneously fit to all the WMO stations by weighted least–squares for each of the 120 months of WMO pressure anomalies. The pressure anomaly at the i^{th} WMO station was represented as a sum of zonal surface spherical harmonics:

$$f(\phi_i,\lambda_i) = \sum_{l=2}^{20} a_{l,0} P_l(\sin\phi_i)$$

or, in matrix form: [f] = [G][a]. [f] was a column vector containing $f(\phi,\lambda)$ and having a length n equal to the number of WMO stations. [G] was a n x 19 coefficient matrix

with elements $G_{l,i} = P_l(\sin\phi_i)$ where 19 was the number of coefficients estimated. [a] was a column vector of zonal coefficients $a_{l,0}$ of length 19.

The NCAR climatology tape contains values that are obviously erroneous and an effort was made to find and remove them. In addition, a diagonal weighting matrix [W] was introduced to minimize the influence of any unedited erroneous values. Surface pressures anomalies were weighted either by 1, 0.1 or 0.001 if the magnitude of the pressure anomaly was within $3\sigma_{WMO}$ of the zero mean, between $3\sigma_{WMO}$ and $5\sigma_{WMO}$ of the mean or greater than $5\sigma_{WMO}$, respectively; see section 3.3.1. The variances of the Navy zonal coefficients were used as the elements of a diagonal *a priori* covariance matrix [S]: $S_{l,l} = \sigma^{-1}_{Navy,l}$. Standard deviations of the Navy zonal coefficients are shown in Figure 3.4a. The weighted, minimum variance, least–squares fit of the WMO pressure anomalies involved solving the following expression for the set of zonal coefficients [a]:

$$\{[G]^T[W][G]+[S]\}[a] = [G]^T[W][f]$$

The effect of [S] is to stabilize the least–squares estimation of the higher degree coefficients. WMO zonal coefficients estimated with and without this conditioning were not significantly different except for those in 1985, when the distribution of WMO stations was poor in the southern hemisphere.

3.4.3 Comparison of WMO and Navy Results by Spherical Harmonic Degree

Figures 3.3a and 3.3b compare the variation in the WMO $a_{2,0}$ and $a_{3,0}$ coefficients from 1976 through 1985 with monthly average Navy and Navy(ib) $a_{2,0}$ and $a_{3,0}$ coefficients. Both WMO and Navy $a_{2,0}$ and $a_{3,0}$ show seasonal variations near 2 and 5 mbars respectively. The Navy(ib) values of $a_{2,0}$ and $a_{3,0}$ have about half the amplitude but nearly the same phase as the Navy $a_{2,0}$ and $a_{3,0}$. The corresponding

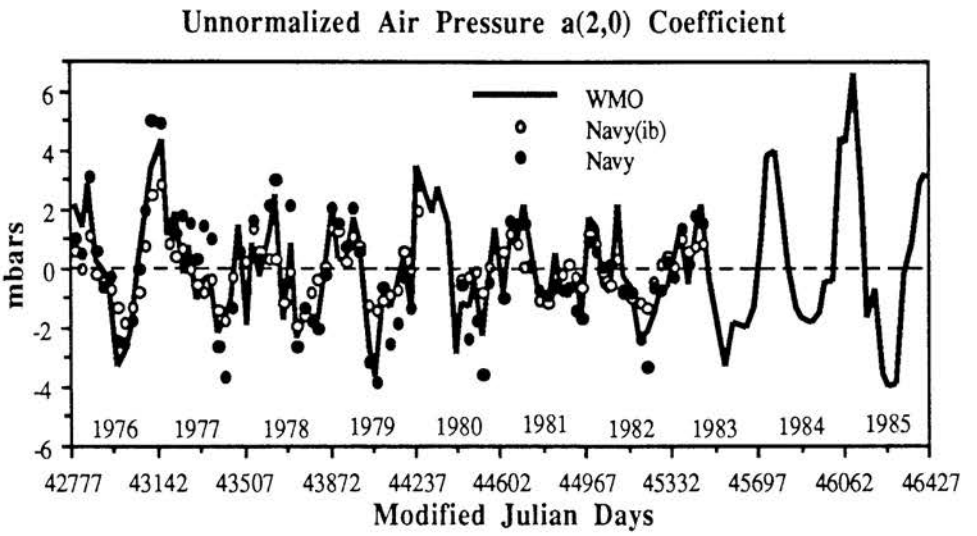

Figure 3.3a. Variation in the WMO monthly mean air pressure $a_{2,0}$ zonal harmonic coefficients, 1976 through 1985. Monthly mean values for the Navy and Navy(ib) air pressure $a_{2,0}$ harmonic coefficients from January, 1976 to June, 1983 are plotted over the WMO curve.

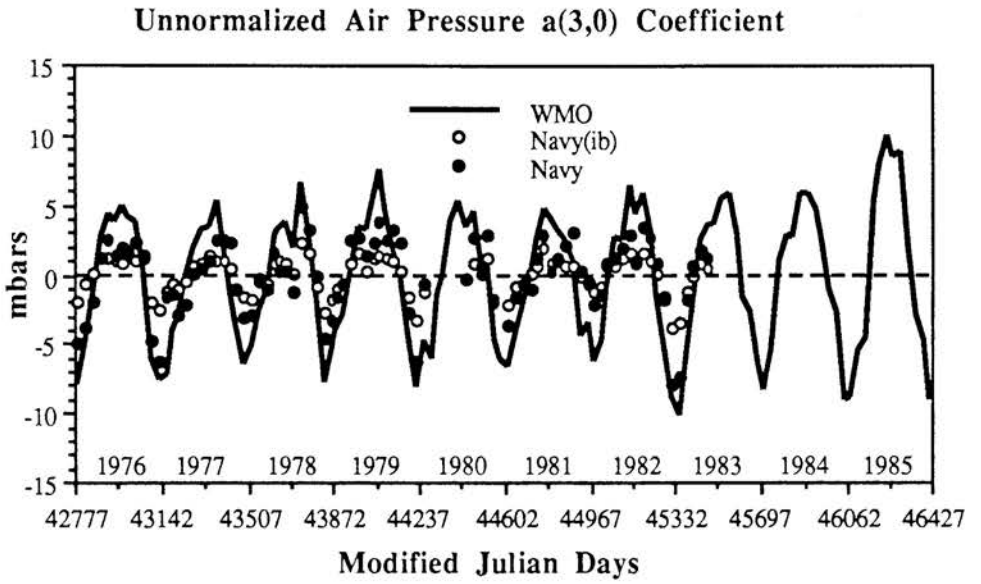

Figure 3.3b. Variation in the WMO monthly mean air pressure $a_{3,0}$ zonal harmonic coefficients, 1976 through 1985. Monthly mean values for the Navy and Navy(ib) air pressure $a_{3,0}$ harmonic coefficients from January, 1976 to June, 1983 are plotted over the WMO curve.

seasonal fluctuations in the geopotential are almost 5 parts in 10^8 for J_2 and 5 parts in 10^5 for J_3.

Changes in $a_{2,0}$ are caused, in large part, by a shift from generally negative pressure anomalies within ±30° of the equator during the first half of the year to generally negative anomalies in both hemispheres above 30° latitude during the second half of the year. Seasonal variation in $a_{3,0}$ is controlled by alternating positive–negative pressure anomalies across the equator within ±45° latitude and, to a lesser extent, between the 0°–45° and 45°–90° latitude bands within hemispheres.

Figure 3.4a show the standard deviation (σ) as a function of spherical harmonic degree for the monthly mean series σ_{WMO}, σ_{Navy} and $\sigma_{Navy(ib)}$. The standard deviations are largest for the low degree zonals, 2 through 9, and decrease smoothly with increasing degree. This is simply because air pressure anomalies are large in areal extent. The σ_{WMO} and σ_{Navy} are quite comparable except for degrees 3 and 9 for which the σ_{WMO} values are much larger than the corresponding σ_{Navy}. The $\sigma_{Navy(ib)}$ are smaller by 50% at lower degree than either σ_{WMO} or σ_{Navy} and vary more smoothly with degree. At higher degrees σ_{WMO}, σ_{Navy} and $\sigma_{Navy(ib)}$ tend to be similar since pressure variations over land, where the inverted barometer effect is absent, tend to be more spacially complex than over oceans and thus contribute more to the higher degree coefficients.

Figures 3.4b and 3.4c show the standard deviation of each zonal coefficient in Figure 3.4a multiplied by Lageos's and Starlette's $d\Omega/dt$ and $Re(d\Psi/dt)$ sensitivities from Table 3.3. These figures show which zonal degrees will contribute most to the perturbation in Ω and Ψ. Figure 4b shows that $a_{2,0}$, $a_{3,0}$ and $a_{4,0}$ variations have the largest effect on Lageos Ω and Ψ. For Starlette, Figure 3.4c shows a greater sensitivity to coefficients up through degree 10 because of its lower altitude.

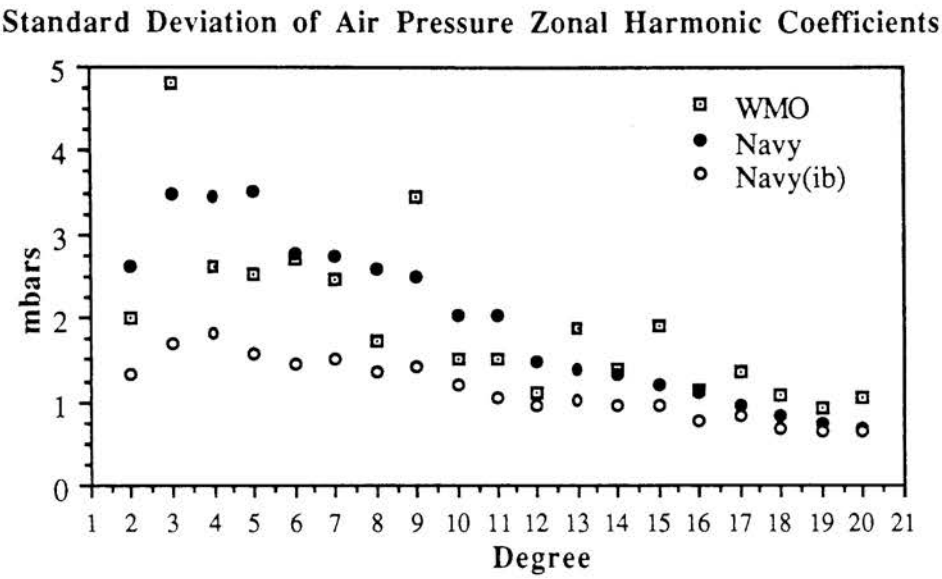

Figure 3.4a. Standard deviation of the unnormalized WMO, Navy and Navy(ib) zonal harmonic coefficients in millibars.

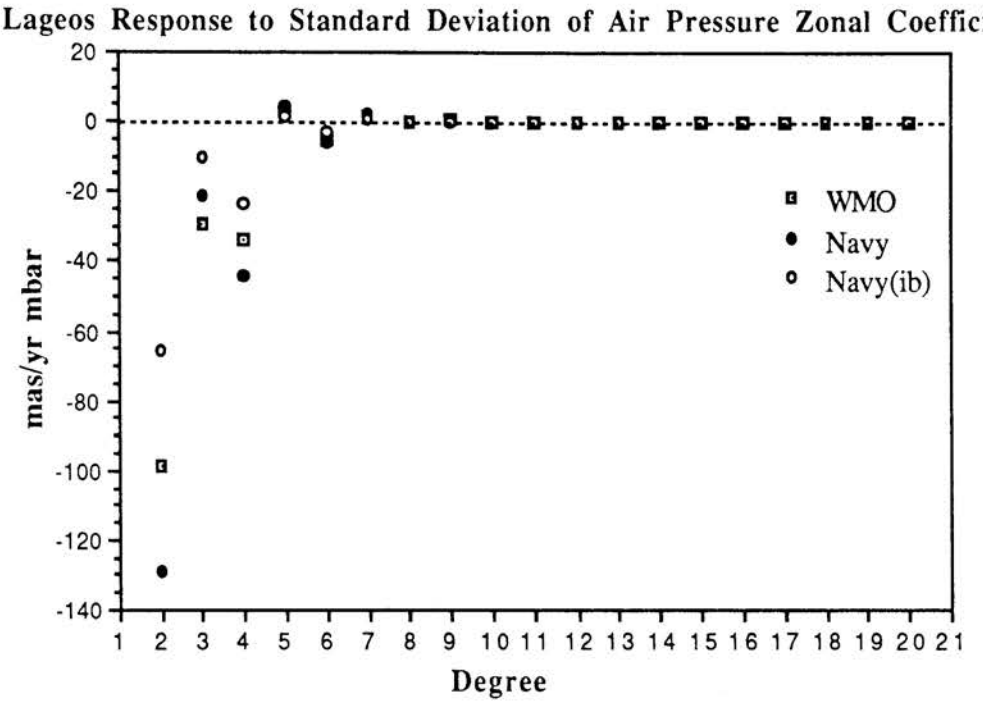

Figure 3.4b. Standard deviation of the zonal harmonic coefficients multiplied by the sensitivity of Lageos' Ω and Ψ excitation to perturbation, from Table 3.2.

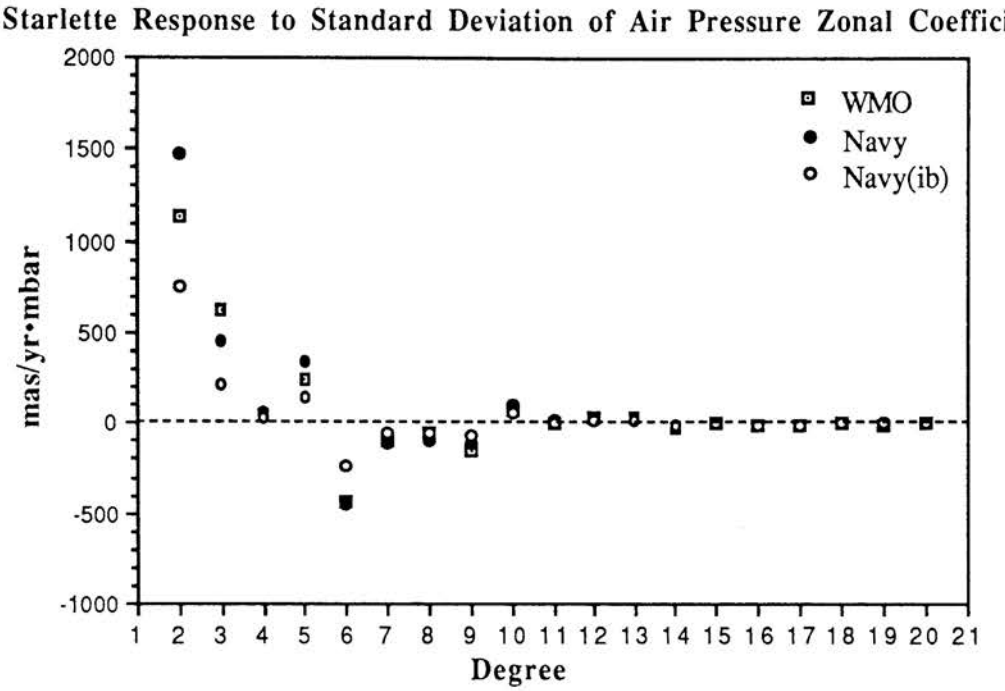

Figure 3.4c. Standard deviation of the zonal harmonic coefficients multiplied by the sensitivity of Starlette's Ω and Ψ excitation.

3.4.5 Comparison with Observed Orbit Residuals

Monthly time series of predicted $d(\delta\Omega)/dt$ and $Re(d\Psi/dt)$ were computed from the WMO zonal coefficients for Lageos via the orbit parameters in Table 3.1 and equations 3.2.1, 3.2.2 and 3.2.3. Predicted $d(\delta\Omega)/dt$ and a $Re(d\Psi/dt)$ time series were similarly computed through 1983 for Lageos using both the Navy and Navy(ib) zonal coefficients. Predicted Lageos $\delta\Omega$ time series were then calculated by numerically integrating the $d\delta\Omega/dt$ series. For Starlette, monthly $d\delta\Omega/dt$, $\delta\Omega$ and $Re(d\Psi/dt)$ series were computed for January, 1983 through December, 1985 from the WMO zonal coefficients. Figures 3.5 and 3.6 show both the observed and predicted Lageos and Starlette $\delta\Omega$ and $Re(d\Psi/dt)$. Annual and semi-annual components were then estimated for the observed and predicted $\delta\Omega$ and $Re(d\Psi/dt)$ from the best least–squares fit sinusoids. Table 3.4 and Figures 3.7 and 3.8 show the results.

Fourier spectral analysis of the observed and predicted $\delta\Omega$ residuals was also undertaken. Spectral analysis was performed on the $d(\delta\Omega)/dt$ series rather than the $\delta\Omega$ because the $d(\delta\Omega)/dt$ spectra, being more nearly white (i.e. flat), were more suitable to Fourier methods. A first–difference estimate of $d(\delta\Omega)/dt$ was computed from the observed Lageos and Starlette $\delta\Omega$. The least–squares fit annual and semi–annual sinusoids in Table 3.4 were subtracted from each Lageos and Starlette $d(\delta\Omega)/dt$ series to further whiten the spectra. Figure 3.10 shows the Lageos and Starlette $d\delta\Omega/dt$ series minus their annual and semi–annual components. The spectral comparison between the WMO and observed Lageos $d(\delta\Omega)/dt$ was limited to 1979 through 1984 because of the lower quality of the observed node residuals before 1979 and the poorer distribution of WMO stations in 1985.

The amplitude spectra, the coherence and phase were estimated for the appropriate pairs of predicted and observed $d(\delta\Omega)/dt$ using a discrete, multi–taper FFT routine.

The multi–taper FFT involves windowing a time series with a set of eight orthogonal prolate spheriodal wave functions [Thompson, 1982]. Each wave function has an associated adaptive weight λ_k, k = 1 to 8. For this application, the λ_k were 1, 1, 1, 1, 0.99995, 0.9938, 0.9457 and 0.7275. In the frequency domain, the prolate spheriodal data windows give rise to a set of spectral windows whose weighted sum is a rectangular window with very low sidelobes. The advantage of multi–taper over conventional windowing is that the prolate spheriodal functions are chosen so that all the data have equal weight in the resultant spectrum.

Writing the discrete Fourier tranforms of the observed $d(\delta\Omega)/dt$ and predicted $d(\delta\Omega)/dt$ as Ω_o and Ω_p and denoting the complex conjugate with an asterisk; then the amplitude spectrum $\Omega\Omega^*$ and the cross–spectrum $\Omega_o\Omega_p^*$ are:

$$\Omega\,\Omega^* = \frac{1}{\sum_{k=1}^{8}\lambda_k}\sum_{k=1}^{8}\lambda_k\,\Omega_k\Omega_k^* \qquad\qquad \Omega_o\Omega_p^* = \frac{1}{\sum_{k=1}^{8}\lambda_k}\sum_{k=1}^{8}\lambda_k\Omega_{o,k}\Omega_{p,k}^*$$

and the squared coherence γ^2 and phase φ are:

$$\gamma^2 = \frac{\left|\Omega_o\Omega_p^*\right|^2}{(\Omega_o\Omega_o^*)(\Omega_p\Omega_p^*)} \qquad \varphi = \arg(\Omega_o\Omega_p^*)$$

Estimated coherence is shown in Figure 3.10 plotted against a 90% confidence limit estimated for 14 degrees of freedom. A 90% confidence limit for coherence is that value which 10% of the estimates will exceed when the true coherence is zero [Koopmans,1974]. We expect significant coherence to also have near zero phase.

Table 3.4 Annual and Semi–annual Components of $\delta\Omega^{\dagger}$ and Re($d\Psi/dt$)*

	Annual				Semi–annual			
	cosine	sine	(amp	phase)	cosine	sine	(amp	phase)
Lageos (1976-1985)								
Observed $\delta\Omega$	15.0	-4.6	(15.7	17°)	-4.3	-0.6	(4.3	172°)
WMO $\delta\Omega$	12.2	-9.2	(15.3	37°)	-0.02	-1.0	(1.0	91°)
Observed ReΨ	41.3	-59.2	(72.2	55°)	11.9	14.5	(18.7	309°)
WMO ReΨ	37.5	2.5	(37.6	356°)	4.2	-3.9	(5.8	43°)
Lageos (1979-1985)								
Observed $\delta\Omega$	14.6	-9.7	(17.5	34°)	-4.4	-2.6	(5.5	141°)
WMO $\delta\Omega$	12.4	-9.0	(15.3	36°)	-0.2	0.5	(0.5	294°)
Observed ReΨ	47.7	-59.5	(76.2	51°)	4.4	-2.4	(5.0	28°)
WMO ReΨ	38.3	2.4	(38.4	356°)	4.2	-1.8	(4.5	24°)
Lageos (1980-1983)								
Observed $\delta\Omega$	10.8	-10.3	(14.9	44°)	-4.75	-2.5	(5.4	152°)
Navy $\delta\Omega$	11.4	-2.5	(11.6	12°)	-0.7	-0.3	(0.7	157°)
Navy(ib) $\delta\Omega$	4.0	-3.2	(5.1	39°)	0.3	0.6	(0.7	297°)
Observed ReΨ	45.2	-63.9	(78.2	55°)	-1.0	-12.2	(12.2	95°)
Navy ReΨ	17.3	5.6	(18.1	342°)	9.4	0.4	(9.4	358°)
Navy(ib) ReΨ	8.3	0.5	(8.3	357°)	3.4	-0.2	(3.4	3°)
Starlette (1983–1985)								
Observed $\delta\Omega$	-241.0	163.1	(291.0	214°)	34.3	26.0	(43.1	322°)
WMO $\delta\Omega$	-138.7	124.5	(186.4	222°)	-15.2	-1.6	(15.3	174°)
Observed ReΨ	-194.3	-109.9	(223.2	151°)	-70.1	26.9	(75.1	201°)
WMO ReΨ	-803.3	210.9	(830.5	195°)	-196.2	-66.1	(207.1	161°)

† in mas,* in mas/yr

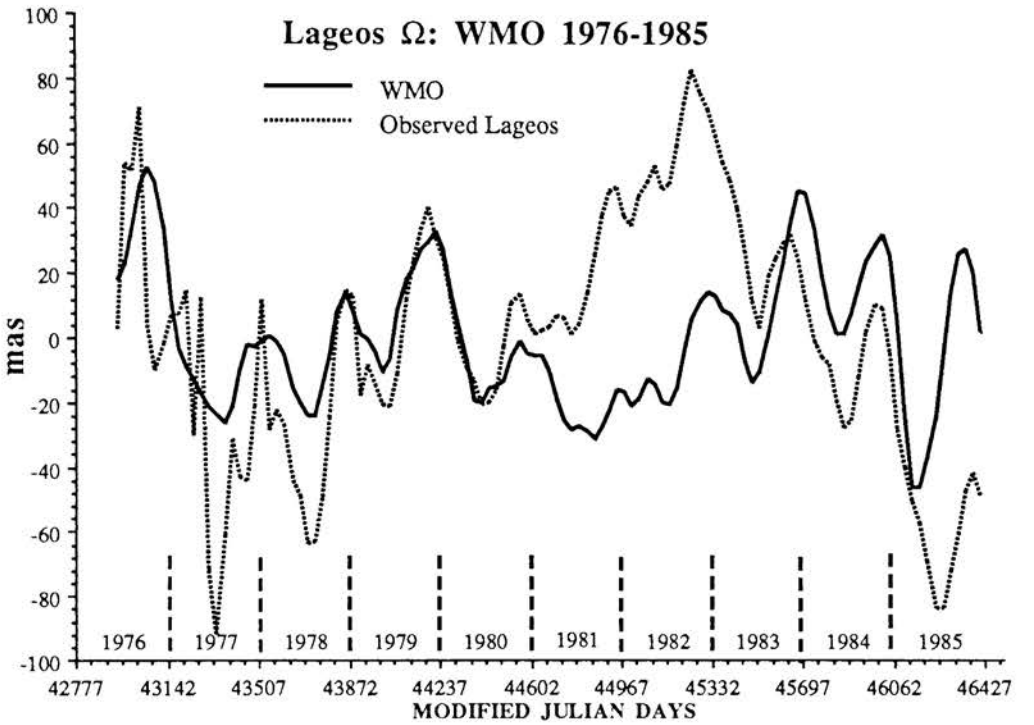

Figure 3.5a. Observed Lageos $\delta\Omega$ is shown with the WMO predicted $\delta\Omega$ for 1976 through 1985. All time series in Figures 3.5a, 3.5b, and 3.5c have had a mean and best–fit trend removed. The large El Niño event which began in late 1982 is apparently preceded by a major anomaly in global air mass distribution.

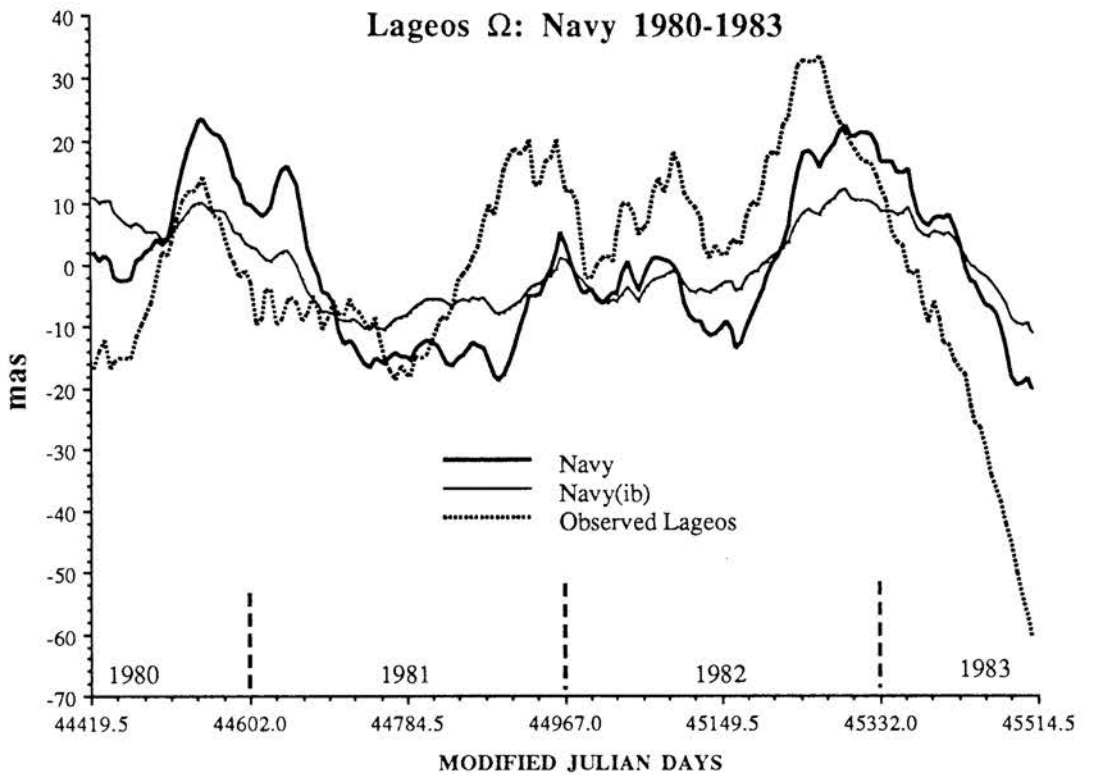

Figure 3.5b. Observed Lageos $\delta\Omega$ is shown together with the Navy and Navy(ib) predicted $\delta\Omega$ for 1980–1983. The 1982 El Niño anomaly is visible in the Navy data.

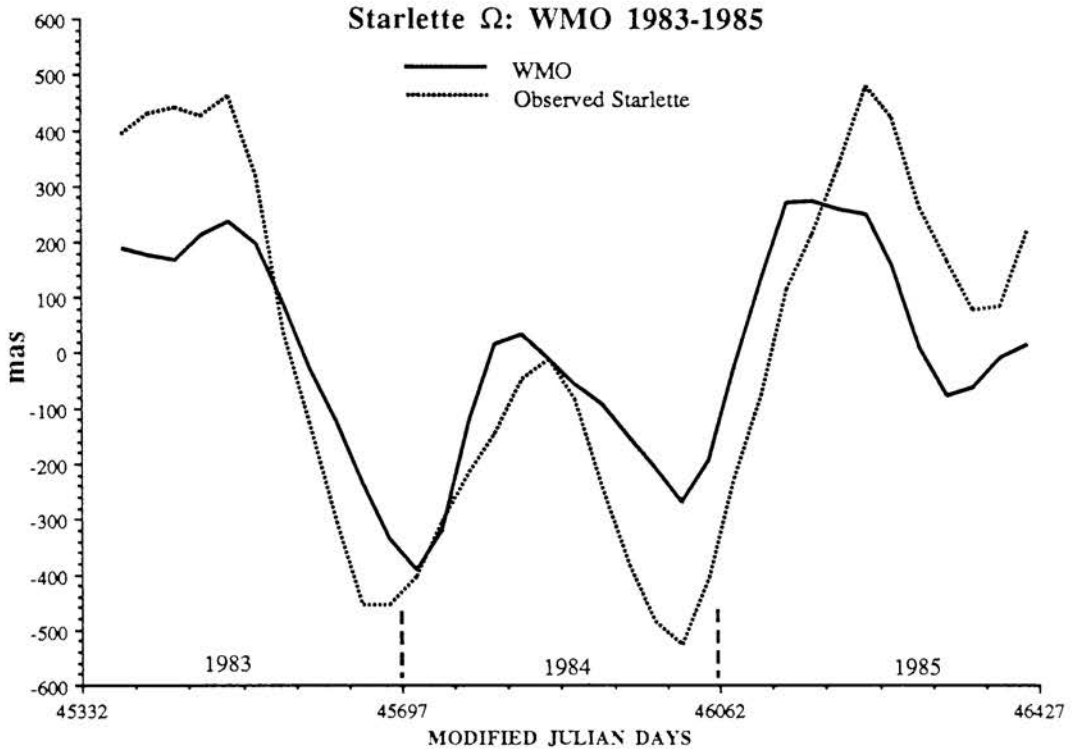

Figure 3.5c. Observed Starlette $\delta\Omega$ plotted against the WMO predicted $\delta\Omega$ for 1983–1985. Observed Starlette $\delta\Omega$ contains a strong quadratic signature, attributable to secular variation in even δJ_l, and tide and drag model errors. This strong quadratic component makes estimating $\bar{J}_2$ difficult [Cheng et al, 1989].

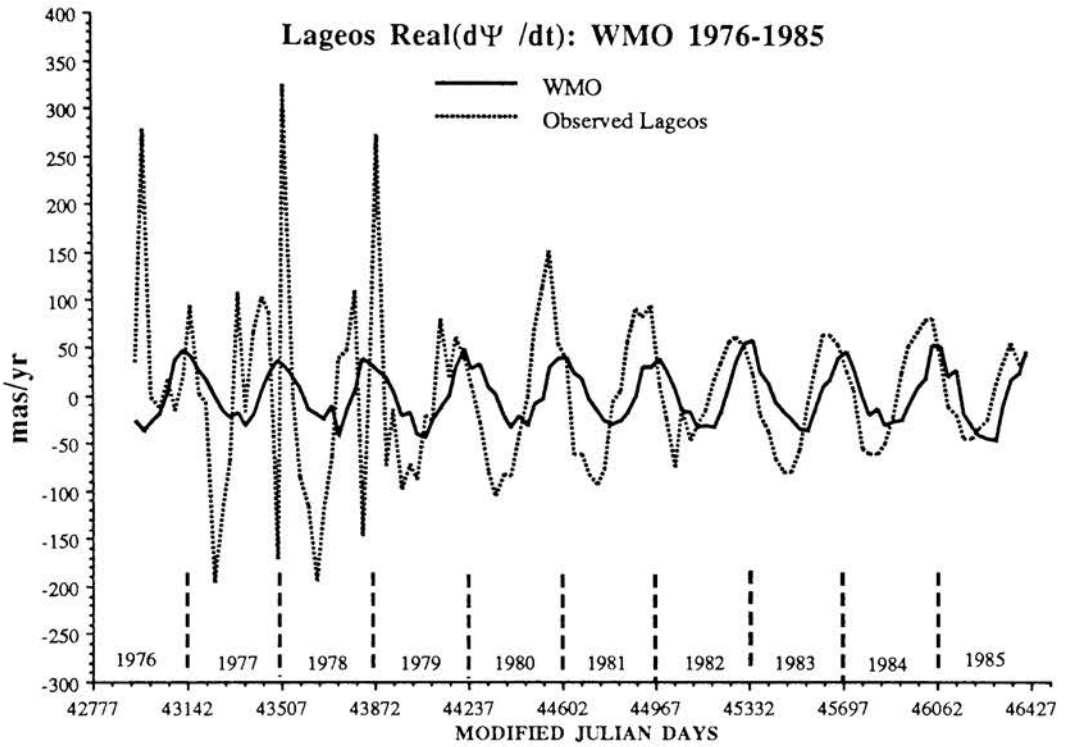

Figure 3.6a. Observed Lageos Re(dΨ/dt) shown with the WMO predicted Re(dΨ/dt) for 1976 through 1985. All time series in Figures 3.6a, 3.6b and 3.6c have had a mean removed. Re(dΨ/dt) does not show an obvious El Niño signature in 1982 as did $\delta\Omega$, suggesting that air mass fluctuations between latitude bands and not across the equator is responsible for the anomaly.

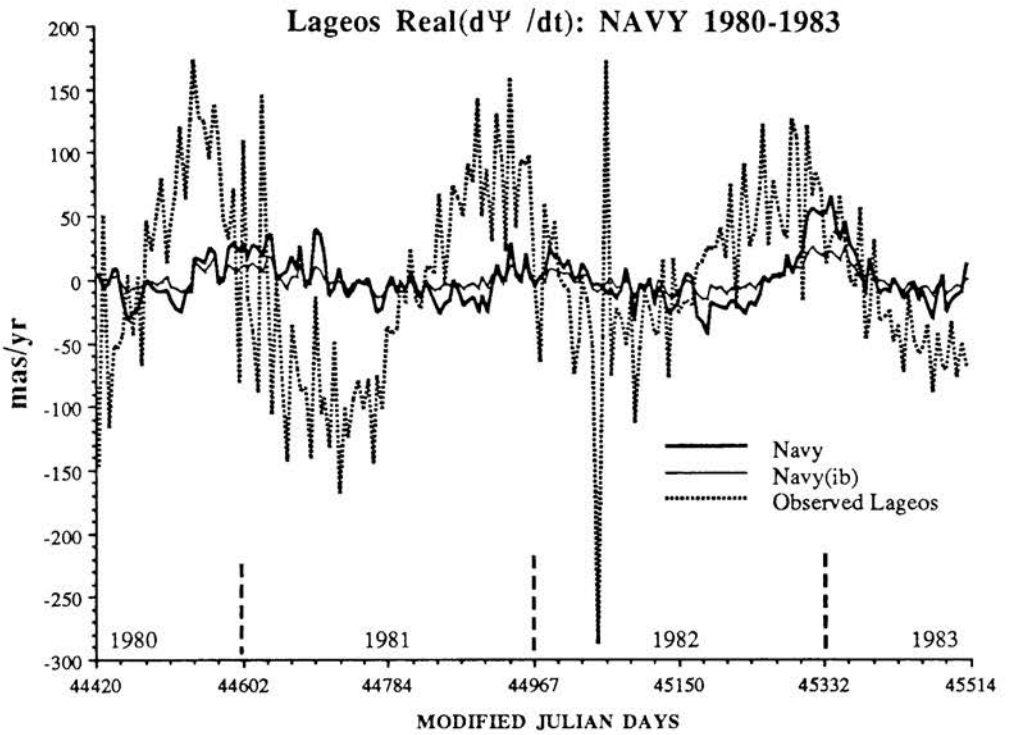

Figure 3.6b. Observed Lageos Re(dΨ/dt) plotted with both Navy and Navy(ib) predicted Re(dΨ/dt) for 1980–1983.

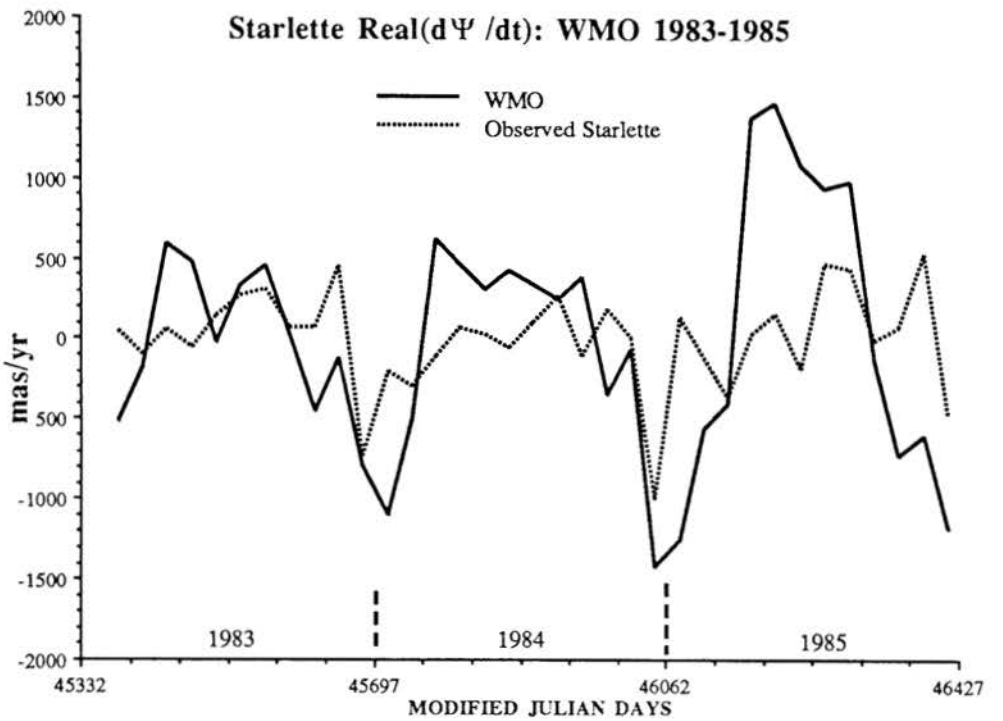

Figure 3.6c. Observed Starlette Re(dΨ/dt) shown with the WMO predicted Re(dΨ/dt) for 1983–1985.

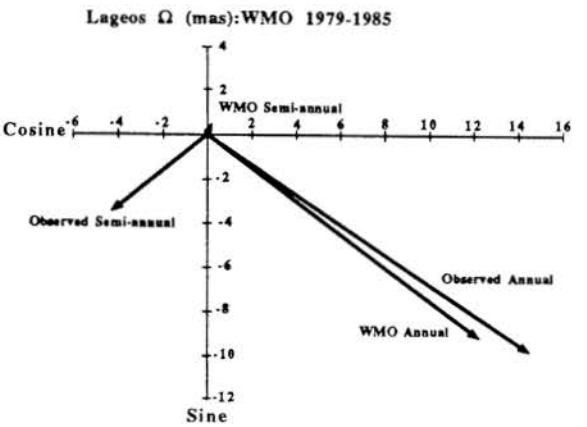

Figure 3.7a. Least–squares fit annual and semi–annual sinusoids of $\delta\Omega$ for Lageos plotted against the $\delta\Omega$ prediction derived from WMO data for 1976–1985. WMO 1976–1985 and Navy 1980–1983 (Figure 3.7b) have about 97% and 80% of the observed annual Lageos $\delta\Omega$ amplitude and agree in phase with the observed $\delta\Omega$ to within 20° and 32°, respectively. Navy(ib) prediction of annual Lageos $\delta\Omega$ differs in phase by only 5° with the observed annual Lageos $\delta\Omega$, but has only 1/3 of the observed amplitude. Starlette annual $\delta\Omega$ and the 1983–1985 WMO prediction differ by 8° in phase, but the WMO prediction has only 2/3 of the observed amplitude; see Figure 3.7c. WMO and Navy predicted semi–annual $\delta\Omega$ are about 1/10 of the observed Lageos amplitude and 1/3 of the observed Starlette amplitude. Discrepancies between predicted and observed phase are over 100° in all but one case.

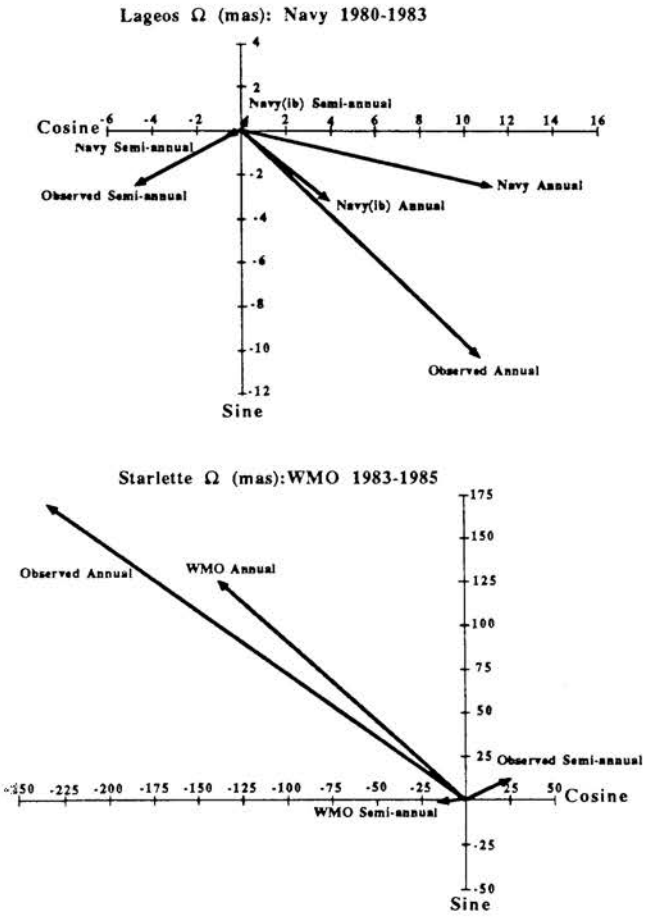

Figure 3.7b. Least–squares fit annual and semi–annual sinusoids of $\delta\Omega$ for Lageos shown with the $\delta\Omega$ prediction from Navy air pressure data for 1980–1983.

Figure 3.7c. Least–squares fit annual and semi–annual sinusoids of $\delta\Omega$ for Starlette shown with the $\delta\Omega$ prediction from WMO data for 1983–1985.

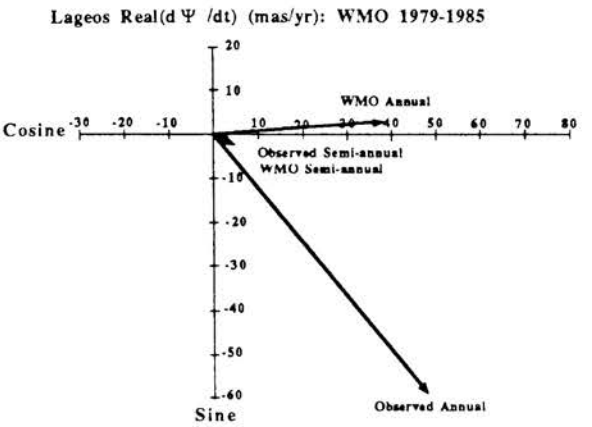

Figure 3.8a. Least–squares fit annual and semi–annual sinusoids for observed Lageos Re(dΨ/dt) shown with WMO predicted Re(dΨ/dt) for 1979–1985. WMO, Navy and Navy(ib) predictions of Lageos annual Re(dΨ/dt) contain only 1/2 to 1/10 of the observed amplitude and differ in phase with the observed annual Re(dΨ/dt) by 60° to 70°; see Figure 3.8b. By 1985, the observed and WMO predicted Lageos Re(dΨ/dt) agree in phase to within 20° and about 10 mas/yr in amplitude. The observed and predicted Lageos semi–annual Re(dΨ/dt) are comparable in amplitude, but they differ in phase by over 90° except for the 1979–1985 WMO semi–annual Re(dΨ/dt) which overlies the observed Lageos semi–annual Re(dΨ/dt). Both the WMO annual and semi–annual Starlette Re(dΨ/dt) have nearly 4 times the amplitude of the observed, and disagree in phase with observed Re(dΨ/dt) by about 40°; see Figure 3.8c.

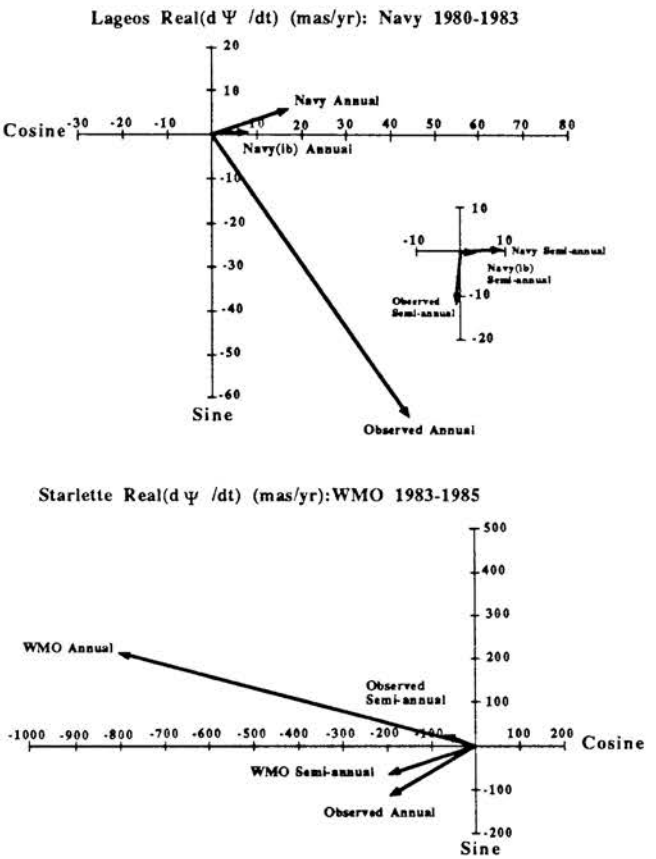

Figure 3.8b. Least–squares fit annual and semi–annual sinusoids of Re(dΨ/dt) for Lageos shown with Navy and Navy(ib) predicted Re(dΨ/dt) for 1980–1983.

Figure 3.8c. Least–squares fit annual and semi–annual sinusoids of Re(dΨ/dt) for Starlette shown with WMO predicted Re(dΨ/dt) for 1983–1985.

3.5 Discussion of Results

Figure 3.5a displays both the WMO predicted $\delta\Omega$ and the observed Lageos $\delta\Omega$. Figure 3.5b shows the Navy and Navy(ib) predicted $\delta\Omega$ from 1980 through 1983 together with the observed Lageos $\delta\Omega$. Year–to–year variability in the observed Lageos $\delta\Omega$ is in reasonable agreement with the predicted $\delta\Omega$. Figure 3.5a shows that during the end of 1981-beginning of 1982, the first year of a severe El Niño event [Rasmussen and Wallace, 1983], the WMO prediction follows the observed Lageos $\delta\Omega$ particularly well. Navy(ib) $\delta\Omega$ in Figure 3.5b is much lower in amplitude than either the Navy $\delta\Omega$, the WMO $\delta\Omega$ or the observed Lageos $\delta\Omega$. The observed Starlette $\delta\Omega$ and the WMO predicted $\delta\Omega$, in Figure 3.5c, also agree very well.

The longer period variations in Lageos $\delta\Omega$, which are most obvious in the 1976–1985 time series, are not well correlated with the meteorological predictions of $\delta\Omega$ and may arise from a number of different sources. At long periods, Lageos $\delta\Omega$ should show the influence of the 18.6 year lunar tide as well as secular changes in the Earth's shape [Yoder et al., 1983]. Long period variations in the WMO zonal coefficients may be due in part to the year–to–year variation in the number and distribution of WMO stations or may reflect real, long term shifts in air mass distribution. The long period variations in the Navy air pressure zonals is likely to be an artifact of the numerical model since the main contribution to these lie at latitudes near 60°S, where there are very few data.

As shown in Table 3.4 and Figure 3.7a, the WMO 1976–1985 and Navy 1980–1983 estimates of Lageos $\delta\Omega$ agree very well with the observed $\delta\Omega$ in both amplitude and phase. If we delete the noisier Lageos data prior to 1979 then Table 3.4 and Figure 3.7 show an even closer agreement in phase between the observed annual Lageos $\delta\Omega$ and the WMO prediction. The Navy(ib) estimate of annual Lageos $\delta\Omega$ is

very close in phase to the observed annual Lageos $\delta\Omega$, but has much smaller amplitude. The Starlette annual $\delta\Omega$ and the 1983–1985 WMO prediction agree very well in phase and moderately well in amplitude. In contrast to the annual $\delta\Omega$, the agreement between the observed and predicted semi-annual $\delta\Omega$ for both Lageos and Starlette are poor in both amplitude and phase.

Table 3.4, and Figures 3.6 and 3.8 show large disagreements between the observed and predicted Re($d\Psi/dt$) for both Lageos and Starlette. The WMO, Navy and Navy(ib) predictions of Lageos annual Re($d\Psi/dt$) are much smaller than the observed amplitude and differ significantly in phase with the observed annual Re($d\Psi/dt$). The large disagreement for the annual and semi–annual components of Re($d\Psi/dt$) belie an interesting convergence, shown in Figure 3.6a, between the observed Re($d\Psi/dt$) and the WMO prediction from 1979 to 1985. There is a similar convergence between the observed Lageos Re($d\Psi/dt$) and the Navy/Navy(ib) predicted Re($d\Psi/dt$).

Figure 3.6c and Table 3.4 show the observed Starlette Re($d\Psi/dt$) to be much smaller in amplitude than the WMO predicted Re($d\Psi/dt$). The amplitude, coherence and phase for the observed and WMO predicted Starlette Re($d\Psi/dt$) were estimated in the manner described in section 3.4.5 and are shown in Figure 3.9. The comparable amplitudes and nearly in–phase coherence between observed and predicted Starlette Re($d\Psi/dt$) over the frequency range 3 to 5 cycles per year (cpy) underscores the effect of interannual air pressure variations on Starlette Ψ irregardless of the disagreement at longer periods.

The WMO and Lageos $d(\delta\Omega)/dt$ time series in Figure 3.10 show strong similarities despite the removal of their annual and semi–annual components. The near–flat amplitude spectra of the WMO and Lageos $d(\delta\Omega)/dt$ series in Figure 3.11a confirm that neither time series contain any significant periodicities while their

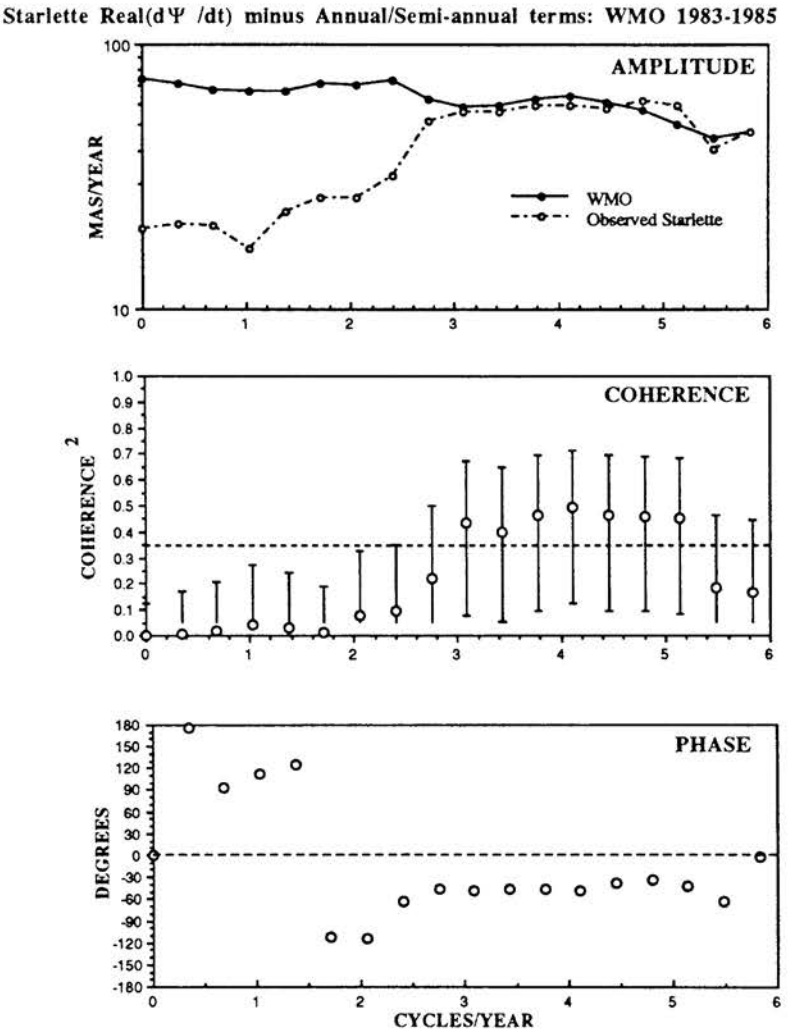

Figure 3.9. Amplitude (square root of the modulus), coherence^2 and phase for observed and WMO predicted Starlette Re(dΨ/dt). Coherence^2 values are plotted against 90% confidence limit and with error bars representing the range of coherence^2 which has a 90% probability of including the true coherence^2 value [Koopman, 1974]. For monthly mean data, ±30° is equivalent to zero phase at the annual frequency.

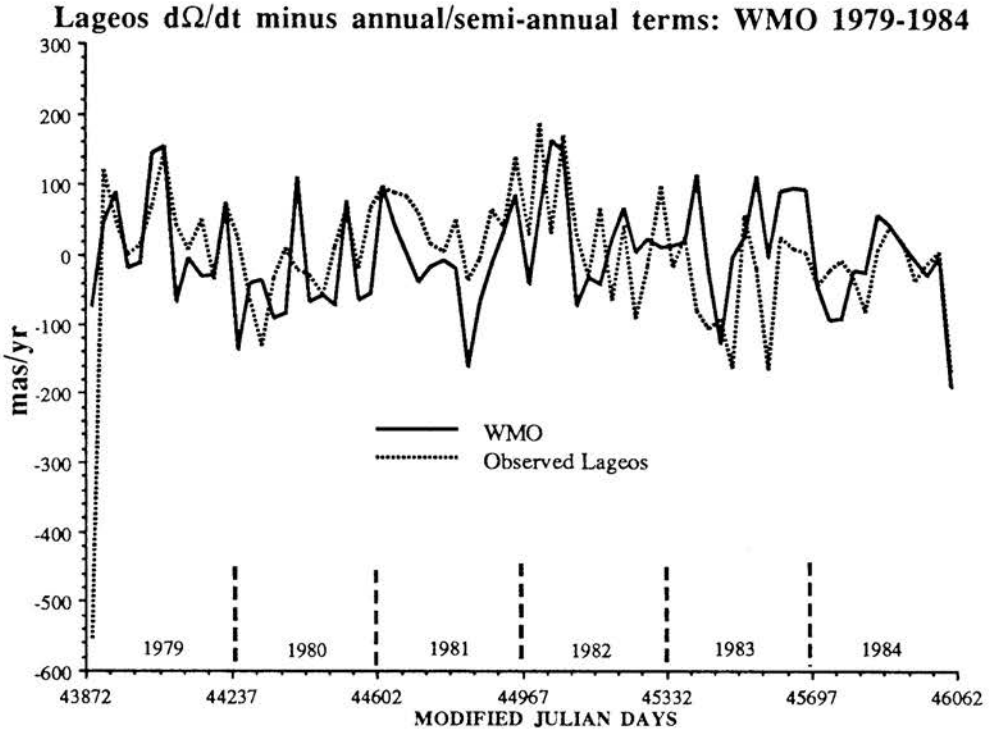

Figure 3.10a. Observed Lageos dΩ/dt is compared to the WMO predicted dΩ/dt over the period 1979–1984. The mean has been removed from all time series shown in Figures 3.10a through 3.10d.

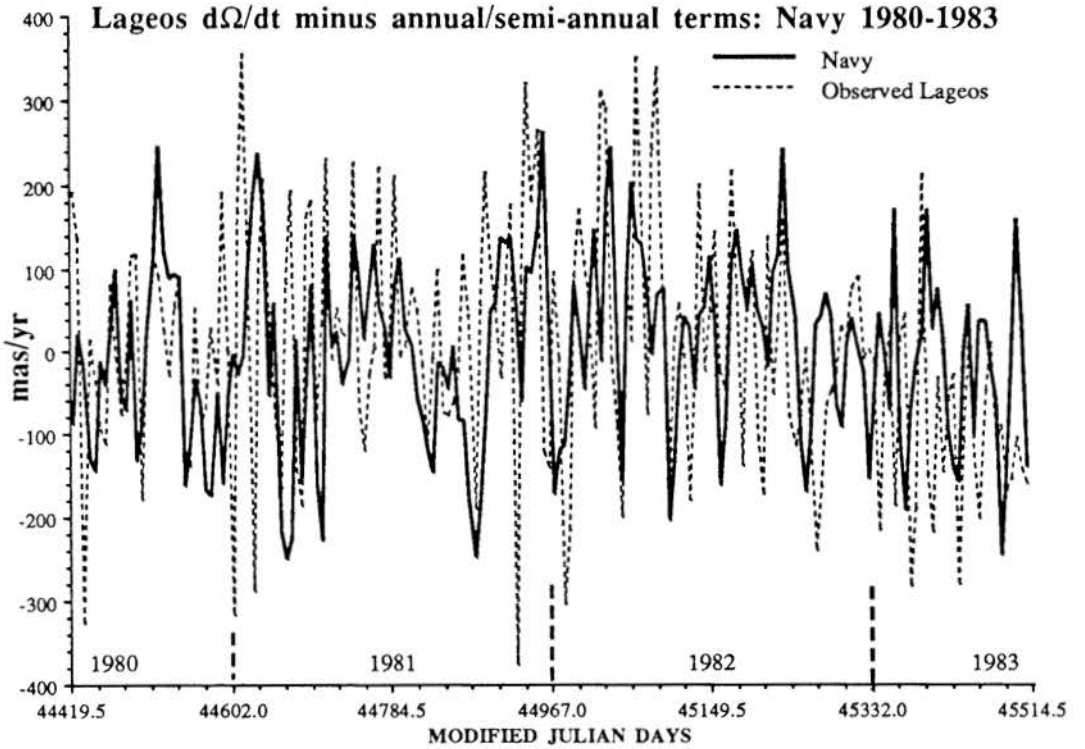

Figure 3.10b. Observed Lageos dΩ/dt compared to the Navy predicted dΩ/dt over the period 1980–1983.

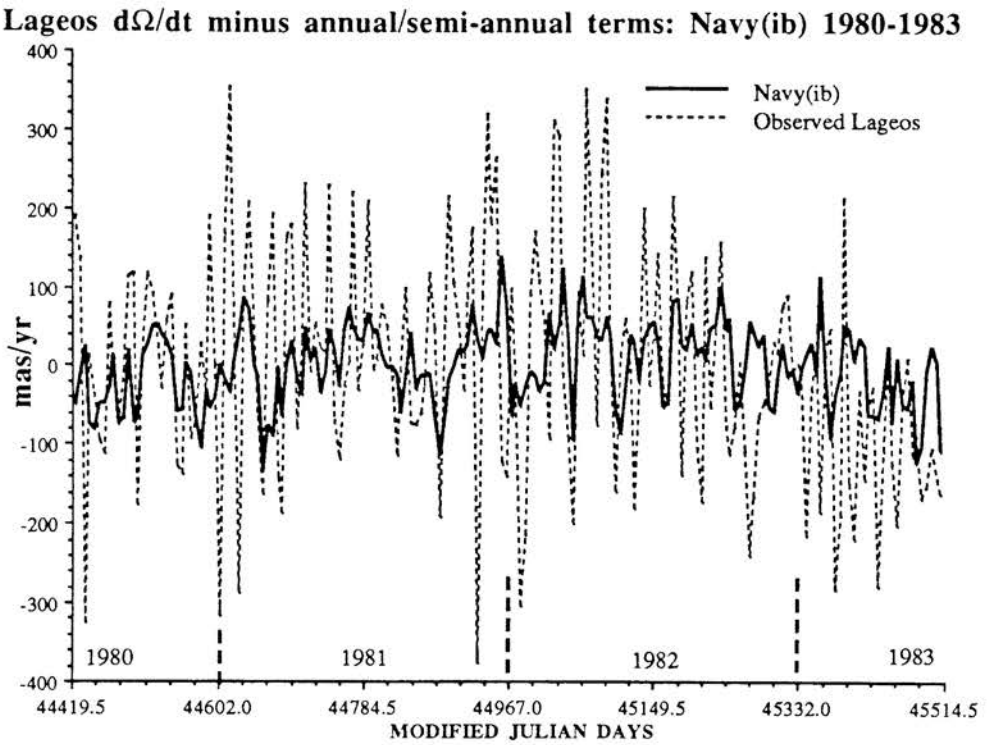

Figure 3.10c. Observed Lageos dΩ/dt compared to the Navy(ib) predicted dΩ/dt over the the period 1980–1983.

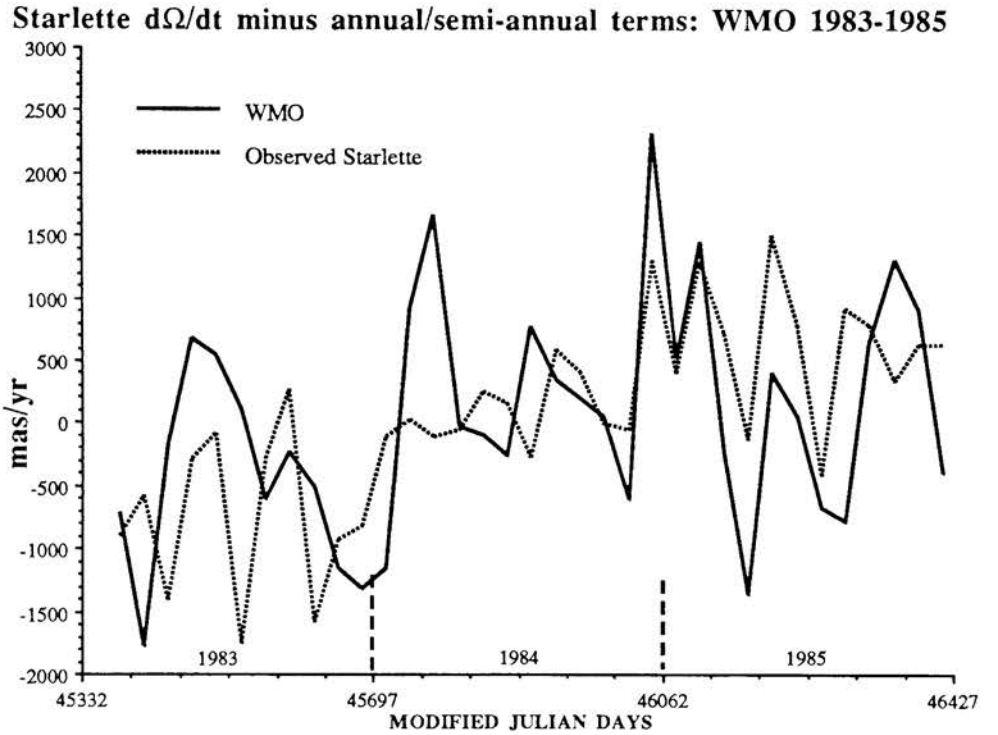

Figure 3.10d. Observed Starlette dΩ/dt plotted against the WMO predicted dΩ/dt for the period 1983 through 1985.

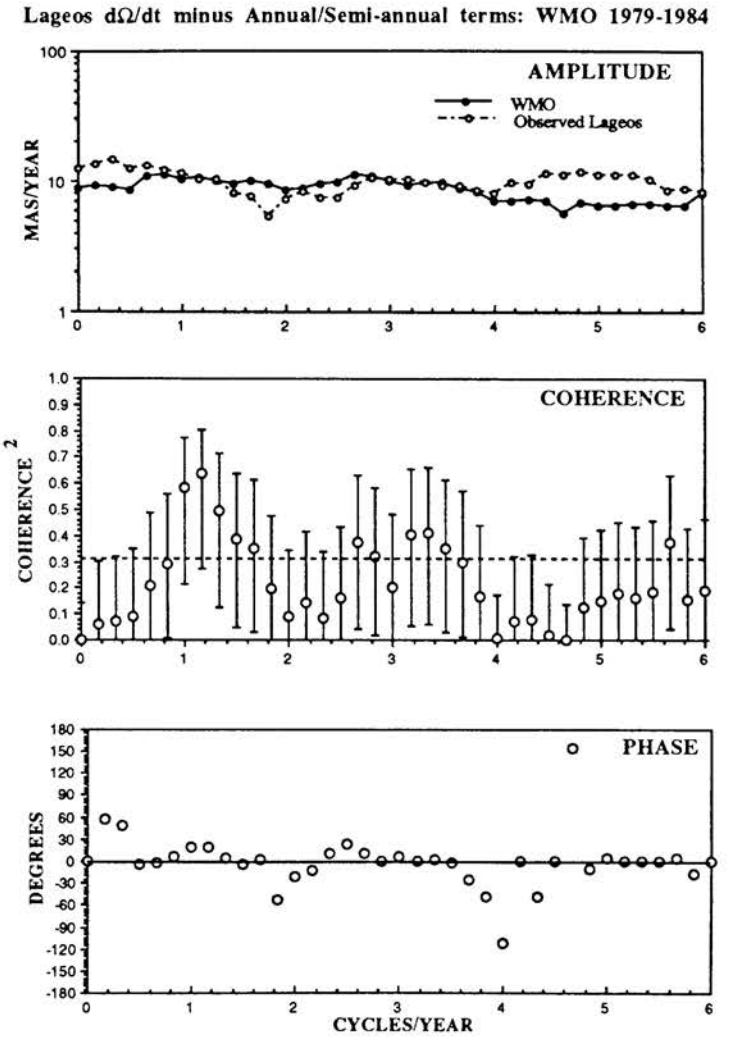

Figure 3.11a. Amplitude (square root of the modulus), coherence^2 and phase for observed Lageos and WMO predicted dΩ/dt over the period 1979–1984.

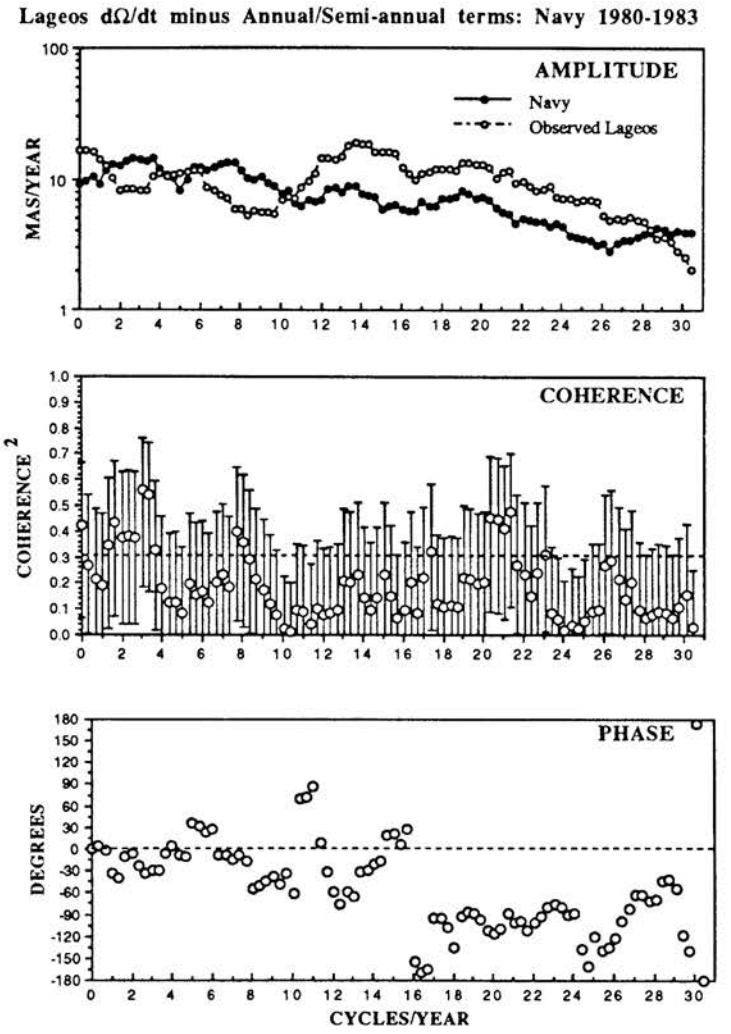

Figure 3.11b. Amplitude, coherence^2 and phase for observed Lageos and Navy predicted dΩ/dt over the period 1980–1983..

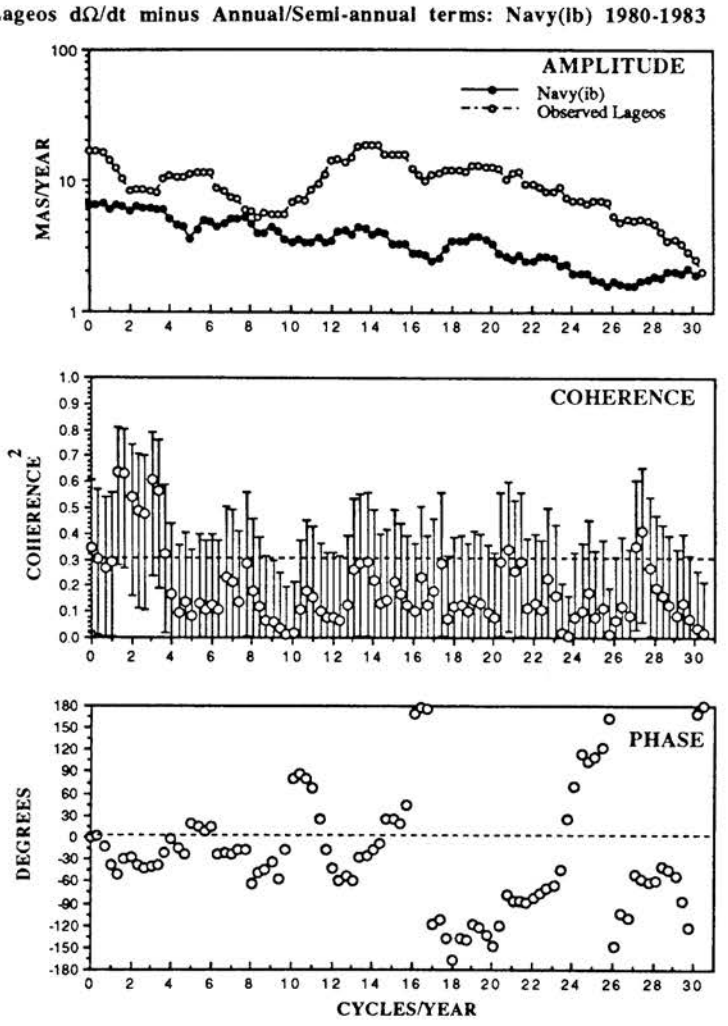

Figure 3.11c. Amplitude, coherence^2 and phase for observed Lageos and Navy(ib) predicted dΩ/dt over the period 1980–1983.

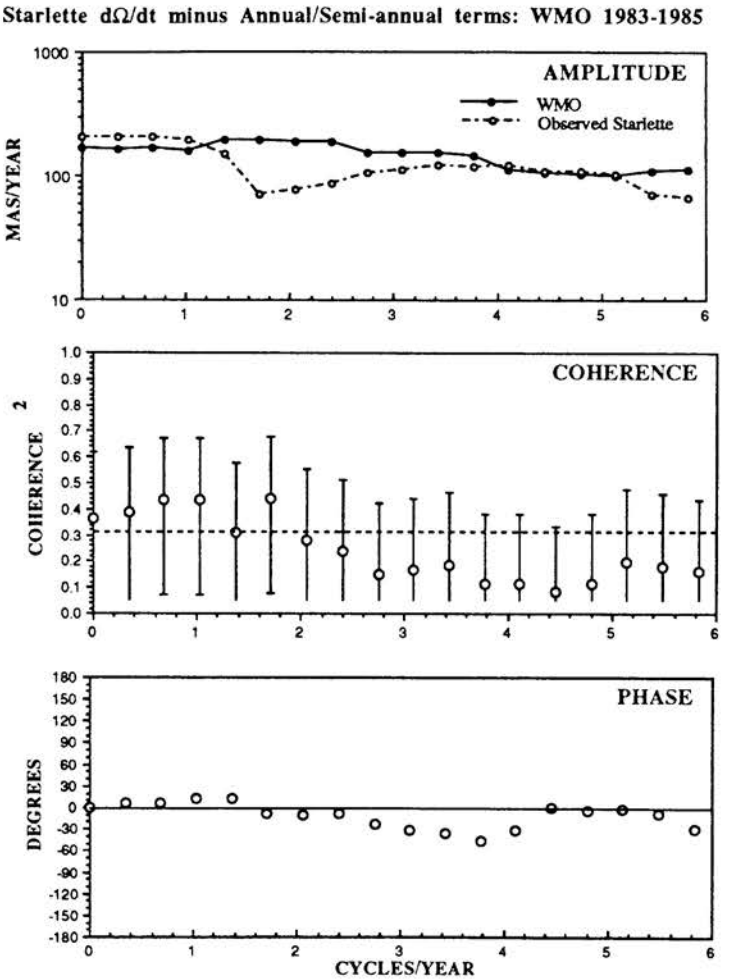

Figure 3.11d. Amplitude, coherence^2 and phase for observed Starlette and WMO predicted dΩ/dt over the period 1983–1985.

coherence and phase spectra demonstrate a significant level of in–phase coherence between 1 and 4 cpy. Figures 3.11b and 3.11c show that the Navy and Navy(ib) coherence and phase spectra show a similar agreement in coherence and phase with the observed Lageos $d(\delta\Omega)/dt$ over the same frequency range of 1 to 4 cpy. In Figure 3.11d, the WMO and Starlette $d(\delta\Omega)/dt$ for 1983–1985 show in–phase coherence between zero and 2 cpy.

3.6 Conclusions

Aside from long period trends, both the WMO $\delta\Omega$ and the Navy $\delta\Omega$ time series appear very similar to the observed Lageos $\delta\Omega$ from 1976 through 1985. The air pressure–predicted $\delta\Omega$ agree very well, both in phase and amplitude, with the observed annual $\delta\Omega$ at the annual frequency. In addition, the WMO, Navy and the observed Lageos $d(\delta\Omega)/dt$ time series show significant in–phase coherence after the removal of annual and semi–annual components. These results demonstrate that global air pressure variations are a significant contribution to the variability in annual and interannual geopotential to which Lageos is most sensitive: the even, low order zonals. The degree of similarity between the observed Starlette $\delta\Omega$ and the WMO predicted $\delta\Omega$ reinforces this interpretation, though it is obvious that additional gravitational and non–gravitational forces, besides the low order, even zonals, affect Starlette.

The dissimilarity between the semi–annual component of air pressure–derived $\delta\Omega$ and the observed $\delta\Omega$ indicates that air pressure variations are not a significant source of the observed semi–annual $\delta\Omega$ perturbation for Lageos and Starlette. Possible sources for the observed semi–annual $\delta\Omega$ include an incompletely modeled semi–annual tide or non–tidal fluctuations in ocean mass distribution.

The contributions of the odd zonal harmonics of global air pressure to Lageos and Starlette is not as well resolved in this study as are the contributions of the even zonal harmonics. The observed perturbations of Lageos' eccentricity are much larger than expected by about a factor of three and analysis at the UT CSR has focused on non–gravitational sources such as the Yarkovsky effect. However, the Yarkovsky effect appears to cause a significant perturbation of Lageos' Ψ only at a 512 day period. The rather enigmatic convergence of the air pressure–derived and observed Lageos Re($d\Psi/dt$) toward 1985 suggests that the observed seasonal perturbations of Ψ may be due to a combination of time–varying sources including global air mass. The observed Starlette Re($d\Psi/dt$) and the WMO prediction differ widely, however their elements of similarity and in–phase coherence at short periods suggests that air pressure variations are also an important contributor to the perturbations of Starlette Ψ.

The WMO/Navy and Navy(ib) air pressure zonals can be interpreted, respectively, as the upper and lower bounds of the range of geopotential variations possible for varying degrees of ocean–atmosphere interaction: completely non–isostatic to completely isostatic. The fact that Ω and Ψ perturbations are more successfully predicted when we ignore the isostatic response of the oceans suggests that there may be another mass redistribution process in the ocean linked to global air pressure which partially mitigates the inverted barometer behavior. This apparent non–isostatic behavior may be due to wind–driven, seasonal variations in ocean mass redistribution.

In conclusion, laser geodetic satellites exhibit a coherent and accurately measureable response to fluctuations in global atmosphere and ocean mass distribution at a variety of time scales. This makes them a potentially useful tool for the study of both weather and climate. In addition, because satellites respond to the ocean mass distribution rather than sea level, this type of data may permit the separation of sea level

variations, as observed by satellite altimetry and tide gauges, into steric and non–steric components. Conversely, oceanographic and meteorological data may become an important element in force models for high precision orbit determination.

4. Geodetic Effects of the Seasonal Redistribution of Ocean Mass

Abstract. We estimate the effect of wind–stress driven ocean mass redistribution on annual polar motion, and on annual and semi–annual variations in the zonal geopotential coefficients. The Hellerman and Rosenstein wind stress field for world oceans is used in combination with the Gill–Niiler bottom pressure equation to estimate annual and semi–annual ocean mass redistribution. Comparision of predicted polar motion with ILS polar motion data suggests that the effect of ocean mass redistribution may be second to air pressure in magnitude. Comparison of predicted gravity variations with gravity variations inferred from Lageos orbital motion indicates that ocean mass redistribution is readily observable by satellite laser ranging.

4.1 Introduction

Observations of polar motion and geodetic satellites like Lageos, Starlette and Ajisai provide sensitive measures of the variations in mass distribution on Earth. At the annual and semi–annual periods, such mass redistribution is almost certainly due to the seasonal movements of air and water. Discrepancies still exist between observed polar motion and the estimated contributions of the atmosphere and continental water storage. In addition, the seasonal gravity variations inferred from satellite orbital motion are not adequately accounted for by the predicted effects of continental water storage and air mass redistribution. This indicates that ocean mass redistribution (variations in non–isostatic sea level) may have a major effect on both polar motion and the seasonal gravity field and that polar motion may also be influenced by ocean current angular momentum and seamount torques.

The annual wobble is a prograde nearly circular motion of the rotation axis relative to geographical coordinates, which is forced by annual motion of air and water. Some important contributors to annual wobble excitation have been identified, including the redistribution of atmospheric mass and associated isostatic adjustment of the oceans [Wilson and Haubich, 1976; Wahr, 1983]. However, there is a significant unexplained portion of annual wobble which implies a lack of understanding of annual variability on Earth. We estimate the contribution to the annual wobble excitation of non–isostatic ocean mass redistribution due to wind stress forcing. Because the effect in question probably contribute only a small fraction of the total seasonal variation in sea level, it would be difficult to detect using tide gauge observations. Therefore, we estimate them indirectly, as in two previous studies [O'Connor, 1980; Wahr, 1983], using a prescribed wind stress field over the oceans.

Atmospheric mass redistribution is apparently a major cause of the seasonal orbital perturbations observed for geodetic satellites like Lageos and Starlette. Predicted satellite orbital perturbations derived from global air pressure differ significantly in amplitude (though not in phase) depending on whether or not oceans are assumed to respond isostatically to air pressure fluctuations. Much of the observed seasonal orbital perturbations can be accounted for by global air mass redistribution if the isostatic response of the oceans is ignored [Gutiérrez and Wilson, 1987]. This suggests that sea level variations due to the oceans' inverted barometer behavior are at least partially mitigated by wind–driven Ekman flow. Therefore, seasonal variations in the gravity field should be more accurately represented by combining variations in global air pressure, corrected for the inverted barometer effect, with the wind stress–driven variations in ocean bottom pressure. We predict the seasonal variations in the zonal spherical harmonic components of the Earth's geopotential due to wind

stress–driven ocean mass redistribution, use them to estimate the average seasonal orbital perturbation for Lageos' ascending node and then compare them to the satellite's observed behavior.

We employ the wind stress field of Hellerman and Rosenstein [1983], as in O'Connor [1980] and Wahr [1983]; but use the ocean response theory developed by Gill and Niiler [1973], rather than a constant–depth barotropic numerical model as in these two earlier studies. The Gill–Niiler theory allows the explicit consideration of bathymetric variations, which Greatbatch and Goulding [1989] have shown to have an important influence on ocean circulation. The Gill–Niiler theory permits an estimate of both the effects of changes in mass distribution and changes in the mountain pressure torque acting on the bottom and sides of the ocean basins. Aside from the use of ocean bottom topography, our methodology also differs from Wahr [1983] in that we modeled individual basins (like O'Connor), and from O'Connor [1980] in that we use both zonal and longitudinal components of wind stress instead of only the zonal component.

4.2 Polar Motion Excitation

Motions within the fluid envelope formed by air and water surrounding the Earth cause small variations in the position of the rotation axis within the Earth. This phenomenon is called wobble or polar motion and consists of the annual wobble, the 14–month Chandler wobble, plus other irregular variations. There is a small pole tide produced by the variable centrifugal force as the rotation axis moves, but it is usually assumed to have a negligible effect on the main features of atmospheric and oceanic motion. Polar motion is routinely observed using the methods of space geodesy, including satellite and lunar laser ranging, and Very Long Baseline Interferometry

(VLBI). Pole positions are reported at five-day intervals by the International Earth Rotation Service and observations of polar motion have been available from the International Latitude Service (ILS) at monthly intervals since the turn of the century.

Three dimensionless parameters (m_1, m_2, m_3) describe the variable elements of the Earth rotation vector $\Omega = (m_1, m_2, 1+m_3)\Omega$ where Ω is the average angular velocity, and Ω is measured relative to Earth-fixed coordinates. The complex variable $\mathbf{m} = (m_1 + im_2)$ describes the location of the point where the rotation axis intersects the Earth's surface, relative to a complex plane defined with real axis along the Greenwich Meridian, and imaginary axis along 90° East longitude. The modulus of **m** is the angle between the rotation axis and the geographic axis, and is expressed in units of milli–arcseconds (mas). The equation governing **m** is, from Lambeck [1980],

$$\frac{i}{\sigma}\cdot\frac{d\mathbf{m}}{dt} + \mathbf{m}(t) = \psi(t)$$

$$\sigma = 2\pi F_c(1 + i/2Q_c)$$

where **m** and ψ are both time variable and complex. The excitation function $\psi(t)$ depends upon the variation in mass distribution and motion of the fluid, corrected for the Earth's response to surface loads. σ is the complex Chandler frequency which describes the dissipation of the Earth at the resonant Chandler frequency F_c in terms of the quality factor Q_c. The digital filter of Wilson [1985] is used with a F_c of 0.843 cycles/yr and a Q_c of 175 to calculate discrete time samples of $\psi(t)$ from the polar motion data, from which the annual sinusoidal component is determined.

ψ is proportional to the torques exerted by the fluid on the earth, which are divided into effects of vertical traction (pressure) and effects of horizontal tractions. Horizontal tractions are further separated into friction and mountain torque contributions:

$$(C - A)\psi = -1.12\,(a_e^4/g)\int p\cdot\cos^2\phi\cdot\sin\phi\cdot e^{i\lambda}\,d\phi\,d\lambda$$
$$+ -1.61\,(a_e^2/\Omega^2)\int p\cdot(\cos\phi\cdot\partial H/\partial\phi + i\sin\phi\cdot\partial H/\partial\lambda)\,e^{i\lambda}\,d\phi\,d\lambda$$
$$+ -1.61\,(a_e^3/\Omega^2)\int(\tau_y + i\sin\phi\cdot\tau_x)\cos\phi\cdot e^{i\lambda}\,d\phi\,d\lambda \quad (4.2.1)$$

= vertical traction (pressure)

+ mountain torque

+ surface friction torque

where integration is over the surface of the Earth. C is the principle moment of inertia about the mean rotational axis; A is the equatorial moment of inertia; g is the surface gravitational acceleration; ϕ and λ are latitude and east longitude; p is the surface pressure; τ_x and τ_y are the eastward and northward tractions; a_e is the mean Earth radius, and H is the topographic height.

In this study, we calculate the first term of expression 4.2.1. The second term, the mountain torque, represents a partial contribution to the time rate of change of angular momentum contained in the horizontal motion of ocean currents, estimated by Wahr [1983] using a numerical ocean model.

4.3 Orbit Perturbation Theory

The spherical harmonic representation of the Earth's gravitational potential V, with respect to satellite orbital dynamics, is [after Kaula, 1966]

$$V = \frac{\mu}{r}\left\{1 - \sum_{l=1}^{\infty}\sum_{m=0}^{l}\left(\frac{a_e}{r}\right)^l P_{lm}(\sin\phi)\left[C_{lm}\cos m\lambda + S_{lm}\sin m\lambda\right]\right\}$$

where C_{lm} and S_{lm} are the coefficients in the expansion, $P_{lm}(\sin\phi)$ are the associated Legendre functions and where r is the distance from the satellite to the Earth's center of

mass. The even zonal terms $C_{l,0}$ cause the satellite's nodes (see Figure 4.1) to precess. The precession rate $d\Omega/dt$ is proportional to a weighted sum of the even zonal terms;

$$\frac{d\delta\Omega}{dt} = \delta J_2 f_2 + \delta J_4 f_4 + \ldots \qquad (4.3.1)$$

$$f_2 = -n.(a_e/a)^2.\frac{3}{2}.\frac{1}{(1-e^2)^2}.\cos i$$

$$f_4 = -n.(a_e/a)^4.\left(\frac{105}{16}\sin^2 i - \frac{15}{4}\right).\frac{(1+3e^2/2)}{(1-e^2)^4}.\cos i$$

$\delta\Omega$ is a small change in the longitude of the ascending node and δJ_l is a small variation in the l^{th} degree zonal coefficient J_l which, by convention, equals $-C_{l,0}$.

A bottom pressure field $p(\phi,\lambda)$ can be described as a sum of surface spherical harmonics with a_{lm} and b_{lm} representing the conventional (unnormalized) spherical harmonic coefficients:

$$p(\phi,\lambda) = \sum_{l=0}^{\infty}\sum_{m=0}^{l} P_{lm}(\sin\phi)\left[a_{lm}\cos m\lambda + b_{lm}\sin m\lambda\right]$$

In turn, the zonal coefficients of barometric pressure can be translated into unnormalized zonal geopotential coefficients using the relationship from McCarthy et al.[1989]:

$$\delta J_l = -\frac{4\pi G\rho_w}{g}.\frac{1+k_l'}{2l+1}.a_{l,0} \qquad (4.3.2)$$

where G is the gravitational constant and g is the average gravitational acceleration. ρ_w is the density of water. k_l' is the surface load deformation coefficient or load Love number [Longman,1963] of degree l and corrects for the effect of the solid Earth response to the surface load. Conventional zonal spherical harmonic coefficients, $a_{2,0}$ through $a_{20,0}$, were least–squares fit to the annual and semi–annual variations in ocean bottom pressure. We then used them with equations 4.3.1 and 4.3.2 to estimate the annual and semi–annual perturbation in Lageos' node, $\delta\Omega$.

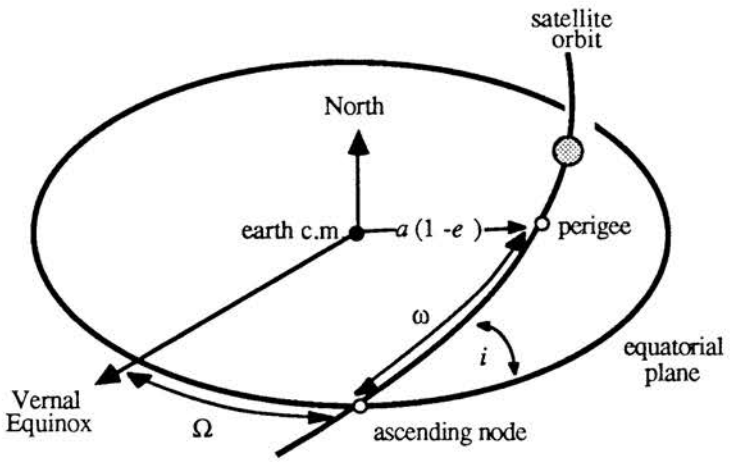

Figure 4.1. Geometrical relationships of the orbital elements: the satellite orbit is an ellipse with the earth at one of the foci, and with a semi-major axis a and eccentricity e. The orientation of the orbit is determined by the longitude of the ascending node Ω and by its inclination. Ω is the angle measured from the direction to the Vernal Equinox and the point where the satellite crosses the equatorial plane in the northernly direction. The inclination i is the angle between the equatorial and orbital planes. The argument of the perigee ω is the angle measured from the ascending node to the satellite's point of closest approach to the earth.

4.4 Gill–Niiler Bottom Pressure Equation

The ocean bottom pressure p_b was estimated from the wind stress τ_s and the ocean bathymetry H, using the Gill and Niiler [1973] bottom pressure equation (GNBPE):

$$\nabla_h (H \cdot \text{cosec}\ \phi) \times \nabla_h(p_b) = \nabla_z \times (\tau_s \cdot \text{cosec}\ \phi) = F \qquad (4.4.1)$$

where ∇_h is the horizontal gradient operator. The horizontal wind stress vector τ_s has northward and eastward components: τ_x and τ_y. The GNBPE ignores bottom friction but is a suitable approximation for long period (e.g seasonal) variations in bottom pressure over large areas (e.g. ocean basins). In addition, the GNBPE is restricted to latitudes greater than about ±15° where flow is predominantly controlled by the pressure gradient rather than the slope of the pyncnocline. Equivalent expressions for 4.4.1 are

$$\frac{\partial H}{\partial \phi} \cdot \text{cosec}\phi \cdot \frac{\partial p_b}{\partial \lambda} - \frac{\partial H}{\partial \lambda} \cdot \text{cosec}\phi \cdot \frac{\partial p_b}{\partial \phi} = F \qquad (4.4.2)$$

or

$$\nabla_z \times [H \cdot \text{cosec}\phi \cdot \nabla_h(p_b)] = \nabla_z \times (\tau_s \cdot \text{cosec}\ \phi) = F \qquad (4.4.3)$$

Using Stokes' theorem, we can evaluate equation 4.4.3 as a line integral about a surface S defined in terms of ϕ and λ. The line integral eventually leads to

$$\int_l H \cdot \text{cosec}\phi \cdot \nabla_h(p_b)\, dl = \iint_s F\, ds = \int_l \tau_s \cdot \text{cosec}\ \phi\, dl = \iint_s \nabla_z \times (\tau_s \cdot \text{cosec}\phi)\, ds \qquad (4.4.4)$$

Values for p_b are solved for on a latitude–longitude grid using the 2°x 2° gridded wind stress data of Hellerman and Rosenstein [1983] and the 1°x 1° gridded bathymetry.

Consider the set of grid points shown in Figure 4.2. Application of equation 4.4.4 to this region suggests that the line integral around the set of 4 points can be written approximately as:

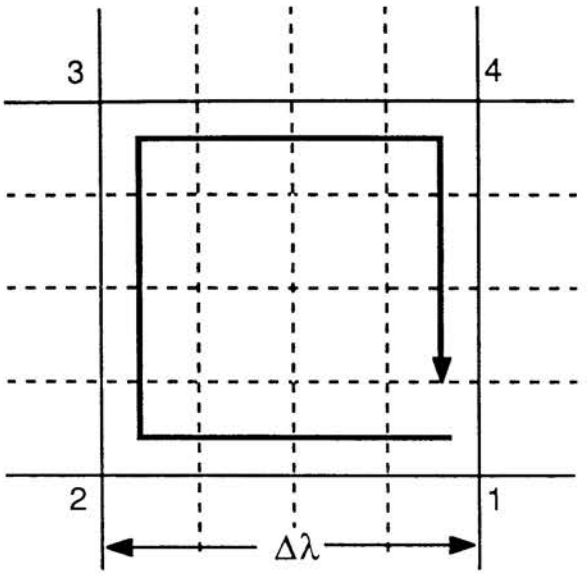

Figure 4.2. Heavy lines represent the grid over which the line integral $\int \tau_s \cdot \text{cosec}\phi \cdot d\lambda$ is evaluated. Dashed lines represent the gridding interval for wind stress and bathymetry data. $\Delta\lambda$ is the longitudinal spacing between the grid nodes.

$$(p_b^2-p_b^1)\int_1^2 H\cdot\mathrm{cosec}\phi + (p_b^3-p_b^2)\int_2^3 H\cdot\mathrm{cosec}\phi + (p_b^4-p_b^3)\int_3^4 H\cdot\mathrm{cosec}\phi + (p_b^1-p_b^4)\int_4^1 H\cdot\mathrm{cosec}\phi$$
$$= \int \tau_s\cdot\mathrm{cosec}\phi \, d\lambda$$

where superscripts denote gridpoint locations. The integrals along the line segments joining the the corners can be evaluated using a grid spacing which is smaller than the separation of points 1–4. Using the areal integral of $\mathrm{curl}_z(\tau_s\ \mathrm{cosec}\phi)$ for the right hand side instead of the line integral in equation 4.4.4 reduces to the method of characteristics used by Gill and Niiler [1973], when the grid points are chosen to lie along contours of constant values of $H\cdot\mathrm{cosec}\phi$. The line integral on the right hand side of equation 4.4.4 is theoretically equivalent to the surface integral, but may not make full use of the wind stress data when large grid spacing is used. We obtained results using both the surface and line integral formulations of the wind stress forcing and found them comparable.

The resulting linear equation in the unknown values of p_b at four grid points can be solved simultaneously with equations from adjacent grid points to obtain the values for an entire basin. To implement this scheme, two additional matters must be addressed. The first is to determine appropriate boundary conditions. The GNBPE is first order in two spatial variables, requiring conditions along only two boundaries. These are chosen to be the eastern edge of the basin, and the equatorial boundary at 15° latitude, following Gill and Niiler [1973]. The eastern boundary has a prescribed value for p_b of zero. For the equatorial boundary, either $p_b = 0$ or a prescribed zero flux, proportional to spatial gradients of p_b, is used. A zero flux condition along the equatorial boundary is determined in the following way. In local cartesian coordinates

$$M_x\,(2\Omega \sin\phi) = -H\,\frac{\partial P_b}{\partial y} + \tau_y$$

$$M_y (2\Omega \sin\phi) = -H \frac{\partial P_b}{\partial x} + \tau_x$$

where M_x and M_y are the vertically integrated components of the horizontal flux. The zero flux across the boundary ($M_y = 0$) implies a linear relationship between two adjacent grid points (e.g, points 4 and 1 in Figure 4.2)

$$p_b^4 - p_b^1 = \tau_x (a_e \cos\phi \, \Delta\lambda/H)$$

where τ_x is taken as an average for the two gridpoints and $\Delta\lambda$ is the longitudinal spacing of the points.

There are two numerical problems to address in the solution of the GNBPE. One arises when the gridpoints include the Antarctic circumpolar region which is connected to itself. In this case, referring to Figure 4.2, points 2 and 3 are the same physical locations as points 1 and 4, requiring that the line or area integrals of wind stress (equation 4.4.1) must vanish, a condition unlikely to be obeyed by real data. We avoid this problem by excluding the circumpolar region from our study.

A second problem appears in regions having closed contours of H·cosecϕ, as discussed by Gill and Niiler [1973]. Because closed contours imply a local maximum or minimum, the horizontal gradient of H·cosecϕ approaches zero, causing the entire left hand side of equation 4.4.1 to approach zero. The right hand side, proportional to the wind stress curl, is generally non-zero, causing the horizontal gradient of bottom pressure to become indeterminately large. One probable solution to this problem would be to include a bottom friction term; the largest of the terms discarded in the derivation of the GNBPE. An alternative is simply to use the GNBPE as it is, but to discard the poorly determined features of the bottom pressure field which are generated under such conditions. We do this using a singular value decomposition of the relevant coefficient matrix to rank and winnow the features of the bottom pressure.

The general form of the equations to be solved is [C][p] = [F] where the coefficient matrix [C] contains the line integrals of H·cosecϕ between grid points, as well as boundary conditions on p_b. [p] is the column vector of grid point pressure values, and [F] is the column vector containing line integrals of τ_s or surface integrals of its curl. To discard the poorly determined features of the bottom pressure field, we use the singular value decomposition to factor [C] into the form

$$[C] = [U][\Lambda][V]^t$$

with [Λ] a diagonal matrix containing positive eigenvalues, the columns of [U] forming an orthonormal set of "data space" eigenvectors, and the rows of $[V]^t$ forming another set of orthonormal "model space" eigenvectors [Menke, 1984]. A representation of model vector p in terms of model space eigenvectors is simply $[p'] = [V]^t[p]$, while the representation of the data F in terms of the data space eigenvectors is $[F'] = [U]^t[F]$, so that simplified equations may be written as

$$[\Lambda][p'] = [F']$$

Because [Λ] is diagonal, this can be written in terms of individual elements as

$$\lambda_i \, p_i' = F_i'$$

In this form, the poorly determined features of [p'] correspond to small or zero eigenvalues and the corresponding elements of [p'] are discarded.

The size of the eigenvalues can be measured by the size of the terms that were discarded in the derivation of the GNBPE. The largest discarded term is probably the bottom stress τ_b. It is common practice in oceanographic theory to assume that bottom stress τ_b is linearly related to horizontal velocity. Using the geostrophic relationship to relate horizontal velocity to gradients in p_b, this implies that $|\tau_b|$ is on the order of $(r/2a_e\Omega)|\partial p_b/\partial\phi$ or $\partial p_b/\partial\lambda|$, where the parameter r is typically assigned values between 10^{-3} and 10^{-4} m/sec [Webster, 1985]. Thus the product $a_e k = (r/2\Omega)$ takes on values

between roughly 10m and 100m. Because p_b varies about a mean value of zero, the magnitude of the spatial derivatives of p_b (differences between adjacent grid points) are of the same order as p_b itself (or the elements of p' as well). We conclude that when λ_i is less than k, it is effectively zero, because kp_i' is of a size considered to be insignificant compared to F_i'. Thus, the associated features of the pressure field are neglected by setting p_i' to zero for all eigenvalues smaller than k.

4.5 Discussion of Results

Annual and semi–annual variations in ocean bottom pressure were computed for three major regions: the north Atlantic, the north Pacific, and the contiguous south Atlantic, south Pacific and southern Indian ocean basins. Table 4.1 shows the estimated real and imaginary components for the prograde (ψ^+) and retrograde (ψ^-) annual polar motion excitation vectors for each of these basins at different values of k. Using k values of 10 and 100 result in very comparable excitation vectors, as does using k values of 30, 50 or 70. Excitation vectors for a k of 10 or 100, $\psi^+_{k=10,100}$, are much larger in amplitude than the excitation vectors for k of 30–70, $\psi^+_{k=30-70}$, and differ in phase by about 90°. These differences do not directly correspond to a variation in any physical ocean parameter since k is a rather ad hoc parameter used to suppress the ill–determined portions of the solution.

Table 4.2, and Figures 4.3 and 4.4 show the summed ocean basin bottom pressure vectors, the ILS excitation poles, the estimated excitation due to air pressure and water storage [Kuehne, 1989], and the bottom pressure excitation vectors from O'Connor [1980] and Wahr [1983]. The $\psi^+_{k=30-70}$ agree in phase with ψ^+ estimated by Wahr [1983], but have about twice the amplitude. The $\psi^+_{k=10,100}$ are similar in phase to the ψ^+ of O'Connor [1980] but are much larger in amplitude.

Table 4.1 Annual Polar Motion Excitation Vector Amplitudes in mas for Ocean Basins

		Prograde		Retrograde	
		real	imag	real	imag
$a_e k = 10$	N. Atlantic	-2.41	-0.75	0.14	1.63
	N. Pacific	7.33	-2.45	8.36	1.27
	S. Oceans	5.27	-3.25	3.46	0.43
	sum	10.19	-6.45	11.96	3.33
$a_e k = 30$	N. Atlantic	-0.20	-0.01	-0.09	0.14
	N. Pacific	-1.45	-0.54	-0.37	-1.25
	S. Oceans	-0.94	-2.43	0.49	-2.32
	sum	-2.58	-2.98	0.03	-3.43
$a_e k = 50$	N. Atlantic	-0.16	0.02	-0.10	0.10
	N. Pacific	-1.01	-0.65	-0.13	-0.85
	S. Oceans	-1.30	-1.47	0.01	-1.37
	sum	-2.47	-2.10	-0.22	-2.12
$a_e k = 70$	N. Atlantic	0.01	0.19	-0.21	-0.11
	N. Pacific	-0.90	-0.57	-0.13	-0.75
	S. Oceans	-1.21	-1.41	0.04	-1.31
	sum	-2.10	-1.80	-0.29	-2.17
$a_e k = 100$	N. Atlantic	-2.40	-0.58	-0.05	1.53
	N. Pacific	6.76	-2.49	7.93	1.02
	S. Oceans	4.13	-4.78	3.54	-1.00
	sum	8.49	-7.85	11.42	1.55
$a_e k = 200$	N. Atlantic	0.02	0.19	-0.21	-0.07
	N. Pacific	-0.10	-0.09	-0.06	-0.02
	S. Oceans	-0.12	-0.82	0.73	-0.49
	sum	-0.20	-0.72	0.46	-0.59

Table 4.2 Annual Polar Motion Excitation Amplitudes in mas

Excitation	Source	Prograde		Retrograde	
		real	imag	real	imag
ILS	Yumi and Yokoyama [1980]	7.14	-14.36	-15.08	-12.15
Air pressure	Kuehne [1989]	-3.16	-17.30	-1.26	-16.43
Water storage	Kuehne [1989]	1.65	-0.69	-6.82	0.59
ILS - air - water		8.65	3.63	-7.00	3.69
bottom pressure, $a_e k = 10$	this study	10.19	-6.45	11.96	3.33
$a_e k = 30$		-2.58	-2.98	0.03	-3.43
$a_e k = 50$		-2.47	-2.10	-0.22	-2.12
$a_e k = 70$		-2.10	-1.80	-0.29	-2.17
$a_e k = 100$		8.49	-7.85	11.42	1.55
$a_e k = 200$		-0.20	-0.72	0.46	-0.59
	O'Connor [1980]	2.48	-1.69	1.69	2.48
	Wahr [1983]	-0.83	-1.84	-0.41	0.66

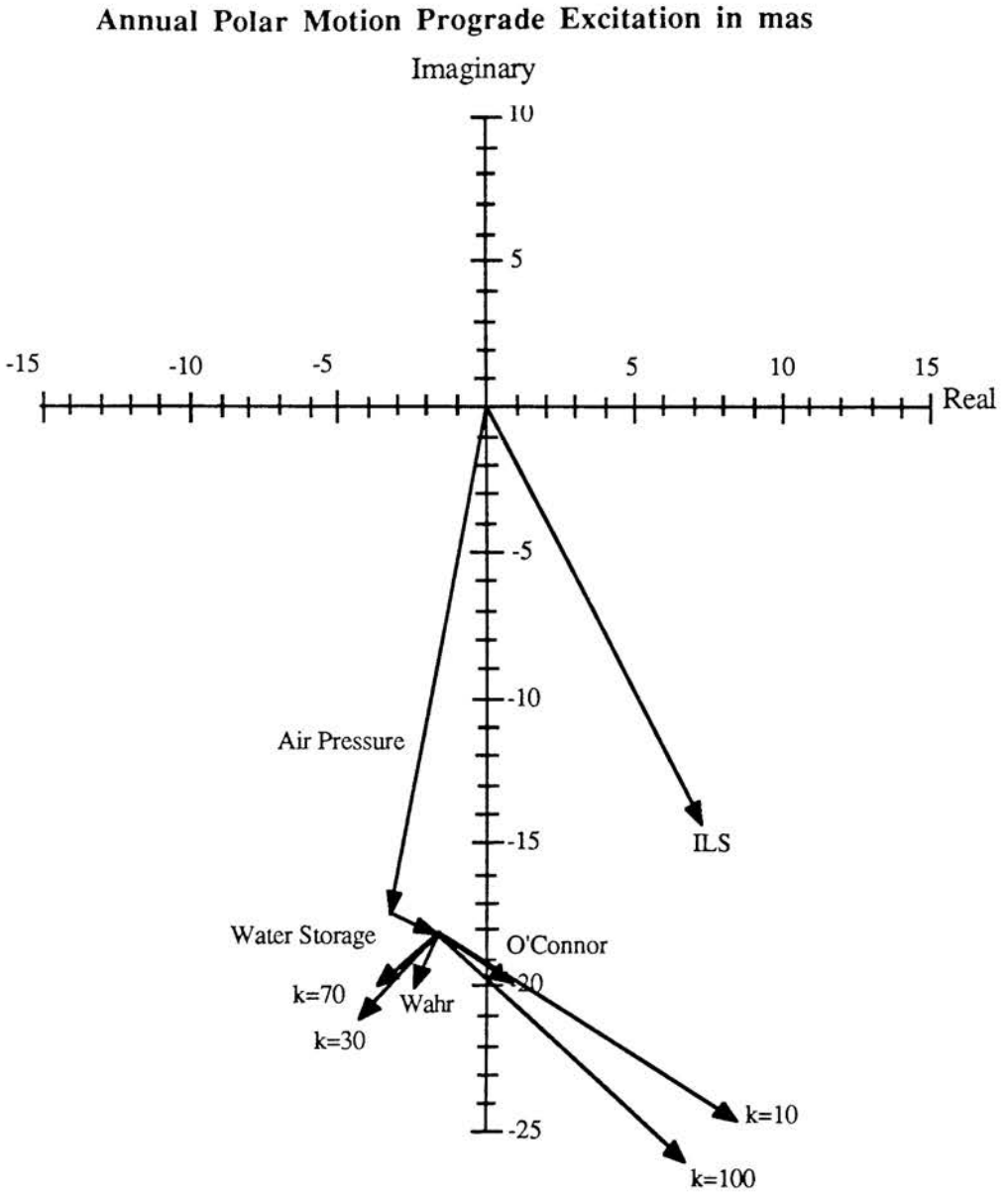

Figure 4.3. Prograde vectors for annual bottom pressure variations for k values of 10, 30, 70 and 100. Also shown are prograde vectors from the ILS, estimated air pressure and water storage [Kuehne, 1989] and the ocean bottom pressure of O'Connor [1980] and Wahr [1983].

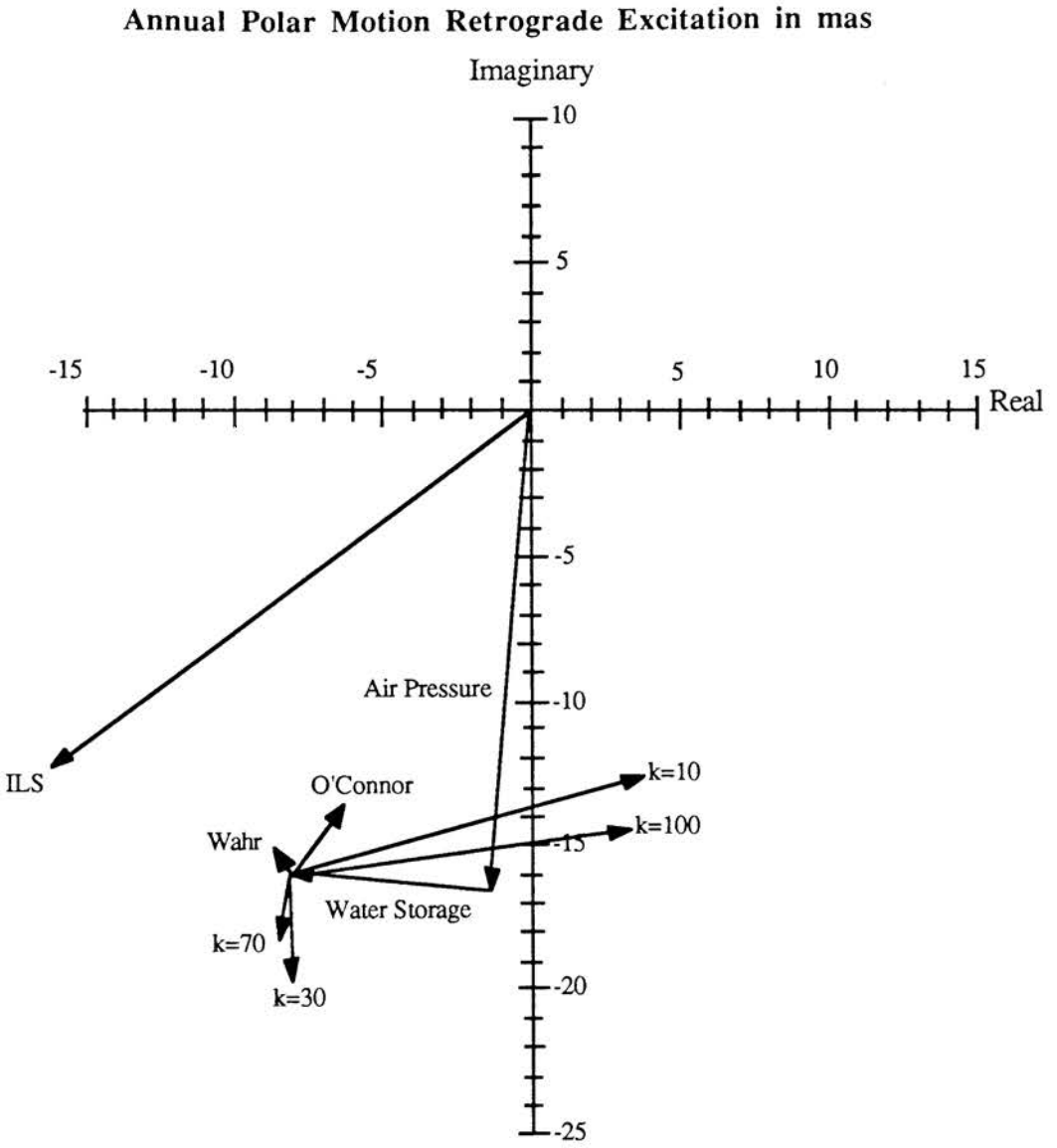

Figure 4.4. The real and imaginary components of the retrograde annual polar motion excitation vectors due to variations in ocean bottom pressure at k values of 10, 30, 70 and 100.

Table 4.3 and Figures 4.5 and 4.6 show the predicted cosine and sine components for annual and semi–annual Lageos $\delta\Omega$ due to ocean bottom pressure and global air mass, and the observed Lageos $\delta\Omega$ for 1980–1983. None of the predicted annual $\delta\Omega$ vectors bridge the gap between the observed $\delta\Omega$ and the air mass $\delta\Omega$. As the case for polar motion excitation vectors, Lagoes $\delta\Omega_{k=10,100}$ vectors differ significantly from the $\delta\Omega_{k=30-70}$; they are respectively much larger and smaller. The wide variation between predicted $\delta\Omega$ for different values of k is no doubt due, in part, to the difficulty in estimating zonal spherical harmonic coefficients from ocean basins that exclude large portions of the polar and equatorial regions. The rather coarse grid size is another additional cause of the wide divergence in the results for different k values. To save computation time, an 8°x 8° grid was used to evaluate the line integral $\int\tau_s\cdot\mathrm{cosec}\phi\cdot d\lambda$. A finer grid may make our implementation of the GNBPE less sensitive to the editing of eigenvalues. Taken as a whole, however, the bottom pressure predictions for $\delta\Omega$ indicate that seasonal gravity variations due to non-isostatic ocean mass redistribution are probably not insignificant and should be readily observable by geodetic satellites like Lageos.

The non–isostatic sea level anomaly for k values of 10, 50 and 100 in the north Atlantic and north Pacific during January and July is shown in Figures 4.7a and 4.7b. Setting k equal to 10 causes non–isostatic sea level to fluctuate by 10 cms or more in some areas. Higher values of k reduce the size of the predicted sea level variations. For k set to either 50 or 100, sea level variations are generally below 2.5 cms in amplitude. For all k, however, the pattern of sea level fluctuation is broadly similar except for the north Pacific basin. The sea level anomaly for most of the north Pacific is negative during the fall and winter, and positive during the spring and summer for k values of 10 and 100. The opposite pattern is exhibited in the north Pacific if k is set to

Table 4.3 Observed and Predicted* Lageos $\delta\Omega$ in mas

Excitation	Source	Annual		Semi–annual	
		cosine	sine	cosine	sine
observed 1980-83		10.8	-10.3	-4.8	-2.5
air mass 1980-83		4.0	-3.2	0.3	0.6
observed - air pressure		6.8	-7.1	-5.1	-3.1
bottom pressure, $a_e k$ = 10	this study	25.0	14.6	-0.9	-3.0
$a_e k$ = 30		-2.1	-5.0	-1.5	-0.5
$a_e k$ = 50		-1.5	-3.7	-0.6	0.3
$a_e k$ = 70		-1.1	-3.2	-0.6	0.4
$a_e k$ = 100		0.9	-0.9	-0.1	0.5

* assuming inverted barometer behavior

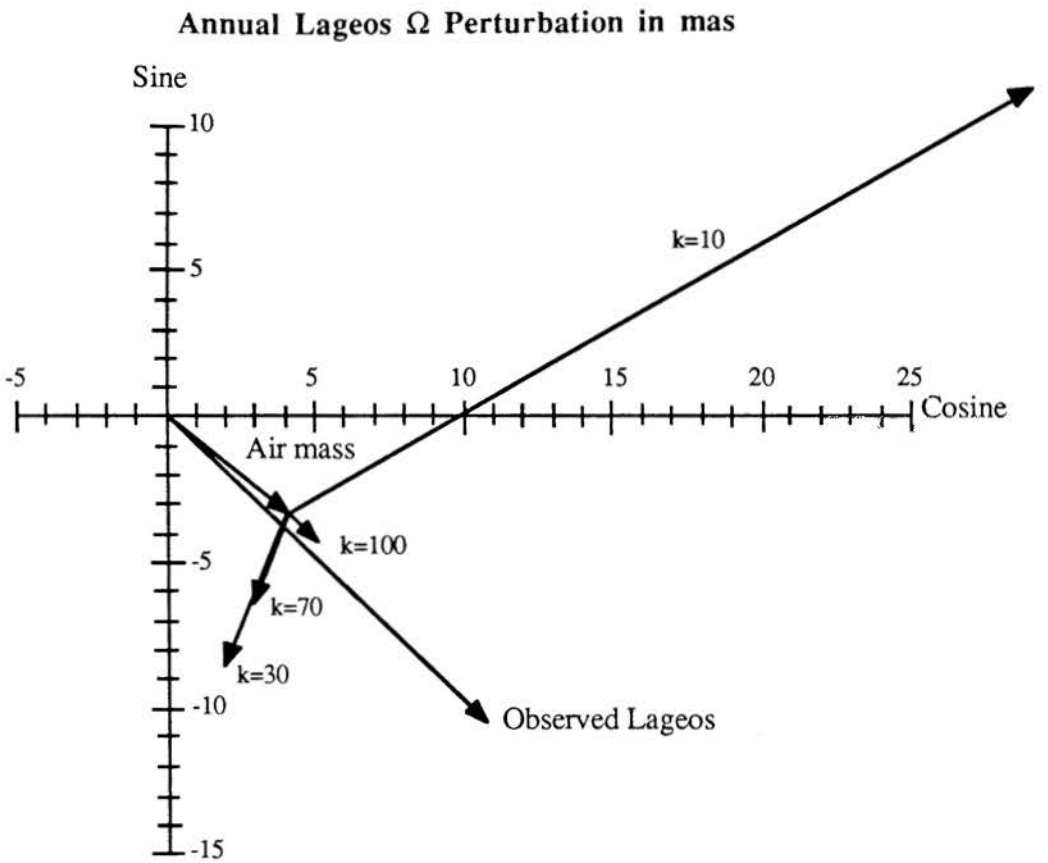

Figure 4.5. Cosine and sine components of the observed annual Lageos $\delta\Omega$ during 1980-1983 and the estimated contribution of air mass to the annual Lageos $\delta\Omega$ assuming isostatic oceans. Annual air mass $\delta\Omega$ was predicted from twice–daily global air pressure fields computed by a U.S. Navy atmospheric model for 1980-1983. Predictions of Lageos' annual $\delta\Omega$ due to ocean bottom pressure at different values of k are plotted from the air mass vector.

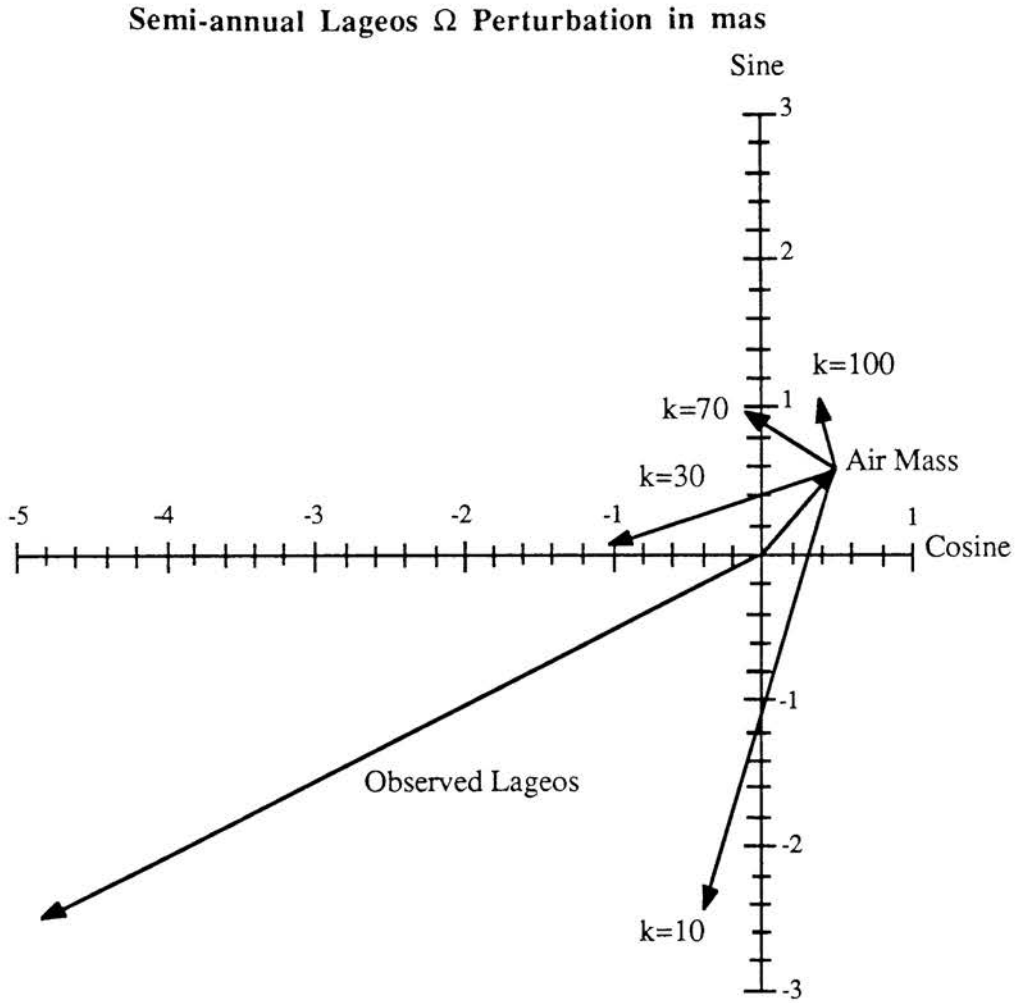

Figure 4.6. Observed cosine and sine components of the semi–annual Lageos $\delta\Omega$ and the estimated air mass contribution to semi–annual Lageos $\delta\Omega$. Plotted from the air mass vector are the predictions of semi–annual Lageos $\delta\Omega$ due to bottom pressure for various values of k.

30–70: positive anomaly during the fall and winter, and negative during the spring and summer. This k–dependency in the north Pacific sea level pattern is probably responsible for the phase differences between predicted ψ and $\delta\Omega$ vectors.

The large amplitudes of the $\psi_{k=10,100}$ excitation vectors and the similarity between the $\psi_{k=30-70}$ excitation vectors and Wahr's [1983] might understandably lend more credence to $\psi_{k=30-70}$ and Lageos $\delta\Omega_{k=30-70}$ than for $\psi_{k=10,100}$ and Lageos $\delta\Omega_{k=10,100}$. However, the non–isostatic sea level fluctuations for a k of 10 are comparable to sea level oscillations measured at mid–ocean islands. Figure 4.8a and 4.8b show average monthly sea level variations measured at Bermuda, Guam, the Aleutians and Samoa [Patullo et al., 1955]. Observations at Bermuda and Guam, adjusted for barometric and steric effects (the inverted barometer response, and water temperature and salinity), are quite comparable to predicted non–isostaic sea level for a k of 10, and much larger than predicted sea level for k of 50 and 100. Observations at the Aleutians and Samoa, which are corrected only for barometric and thermal effects, are more poorly matched by predicted sea level for all values of k.

4.6 Conclusions

The excitation vectors estimated in this study for intermediate values of k, $\psi_{k=30-70}$ seem to indicate that ocean bottom pressure is not a major contributor to annual polar motion. This is what Wahr [1983] decided. Although these annual excitation vectors are twice as large as Wahr's, they still do not account for the difference between the observed ILS excitation and the air pressure and water storage excitations. Likewise, the bottom pressure predictions of Lageos $\delta\Omega$ for k greater than 10 do not have sufficient amplitude to account for the difference between the observed Lageos $\delta\Omega$ and the air mass prediction, assuming isostatic oceans.

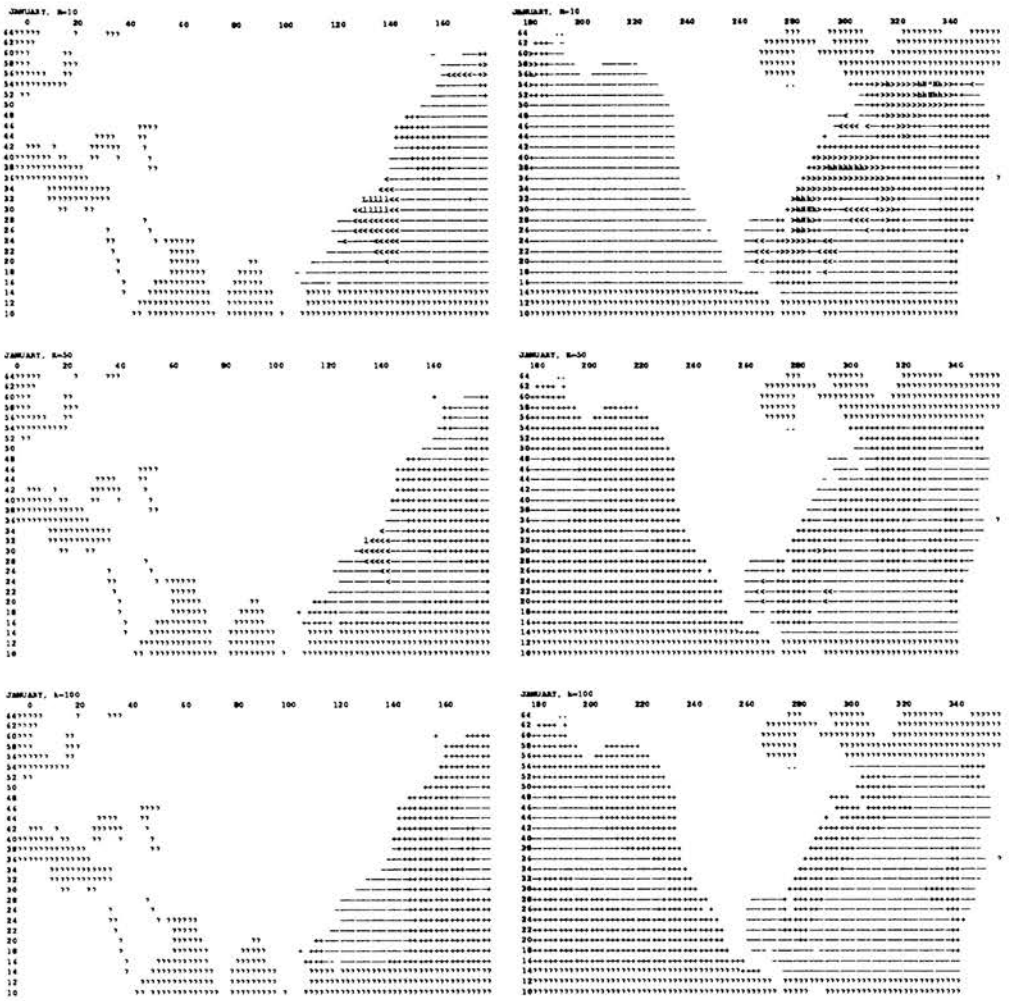

10.0 cm	<*			! < -10.0 cm	
7.5 cm	<H≤	10.0 cm	-7.5 cm	>L≥ -10.0 cm	
5.0 cm	<h ≤	7.5 cm	-5.0 cm	>l ≥	-7.5 cm
2.5 cm	<>≤	5.0 cm	-2.5 cm	>< ≥	-5.0 cm
0.0 cm	<+ ≤	2.5 cm	0.0 cm	> - ≥	-2.5 cm

Figure 4.7a. Annual component of non–isostatic sea level in the north Atlantic and Pacific for January; estimated for k values of 10, 50 and 100 .

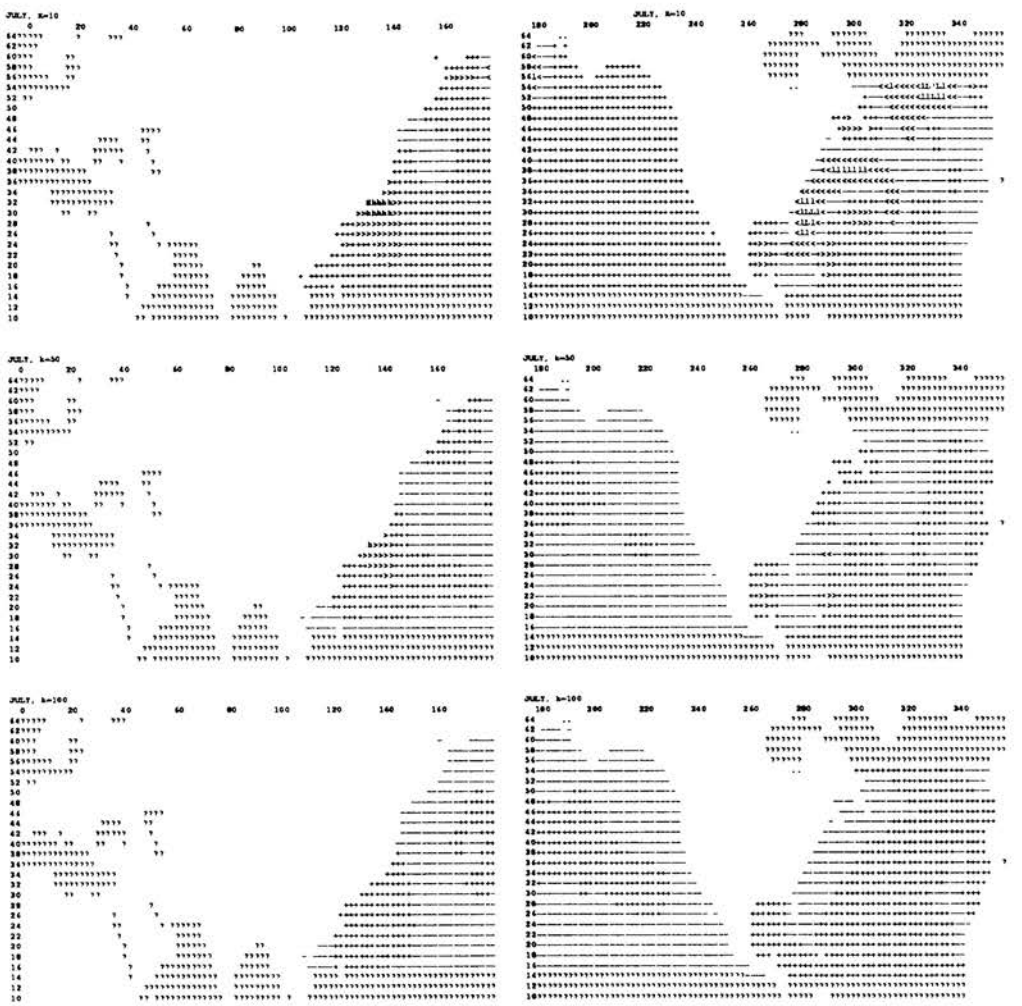

10.0 cm	<*			! < -10.0 cm	
7.5 cm	<H≤	10.0 cm	-7.5 cm	>L≥	-10.0 cm
5.0 cm	<h ≤	7.5 cm	-5.0 cm	>I ≥	-7.5 cm
2.5 cm	<>≤	5.0 cm	-2.5 cm	>< ≥	-5.0 cm
0.0 cm	<+ ≤	2.5 cm	0.0 cm	> - ≥	-2.5 cm

Figure 4.7b. Annual component of non–isostatic sea level in the north Atlantic and Pacific for July; predicted using k values of 10, 50 and 100.

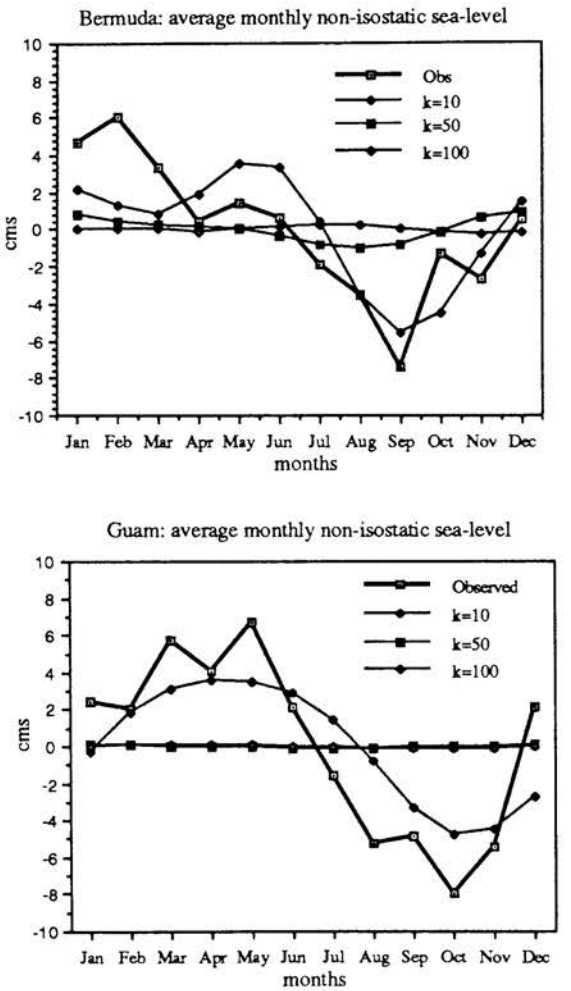

Figure 4.8a. Average monthly sea level variations for Bermuda (32°N, 64°W) and Guam (18°N, 148°E) corrected for thermal and haline fluctuations, and the inverted barometer effect [Patullo et al., 1955]. Predicted sea level variations, annual plus semi–annual components, at these locations for k of 10, 50 and 100 are shown for comparison.

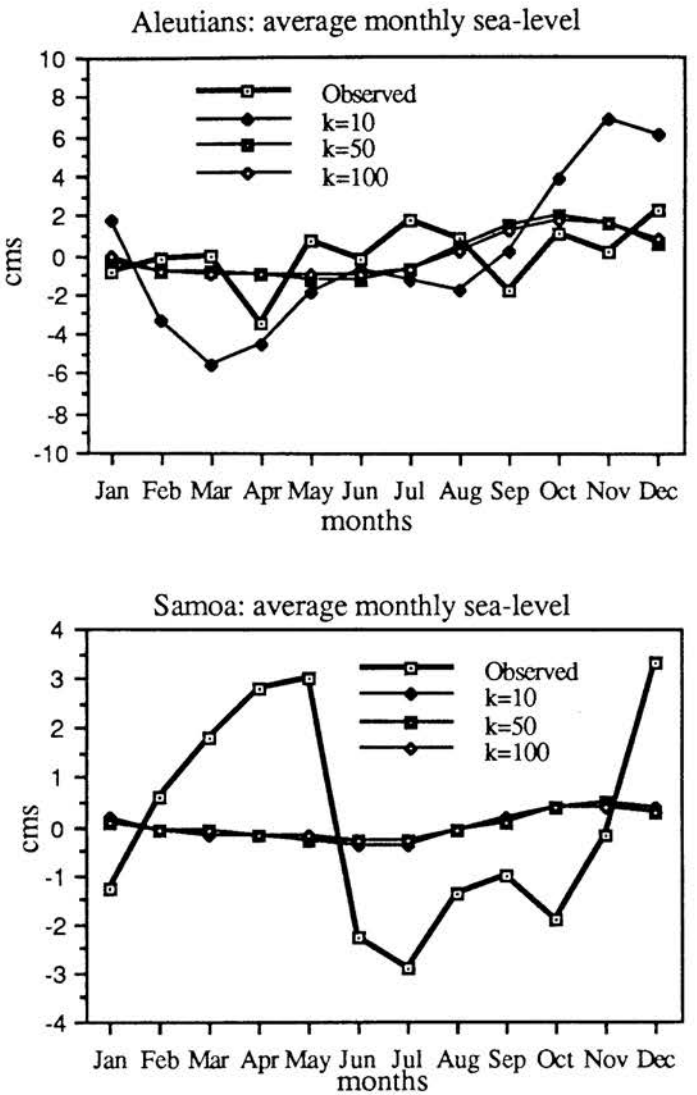

Figure 4.8b. Average monthly sea level at the Aleutians Islands (52°N, 180°E) and Samoa (16°S, 172°W) corrected for water temperature and the inverted barometer effect [Patullo et al., 1955]. Also shown are the predicted sea level, annual plus semi–annual components, at these locations for different k values.

For k equal to 10, the resulting $\psi_{k=10}$ and Lageos $\delta\Omega_{k=10}$ are certainly large enough to make ocean mass redistribution a likely source for the unaccounted component of annual polar motion and Lageos $\delta\Omega$. Also, the agreement between observed and predicted sea level at Bermuda and Guam tend to make these larger ψ and Lageos $\delta\Omega$ vectors more credable. Unfortunately, neither the $\psi_{k=10}$ nor the $\delta\Omega_{k=10}$ vectors have the required phase. The summed ψ vectors for air pressure, water storage and ocean mass do not agree in phase with the ILS ψ vector. The annual air pressure $\delta\Omega$ vector plus the ocean mass $\delta\Omega_{k=10}$ vector do not match the observed Lageos $\delta\Omega$ in phase and are too large in amplitude.

Nonetheless, we feel that the results from the application of the Gill–Niiler bottom pressure equation to the problem of polar motion and Lageos' $\delta\Omega$ are rather encouraging, because they are certainly not conclusive. These results suggest that the effect of ocean mass redistribution to annual polar motion is at least twice as large as water storage and it may be second only to air pressure in magnitude. In addition, the predicted Lageos $\delta\Omega$ indicate that ocean mass redistribution should be readily observable using geodetic satellites like Lageos. By coupling a more comprehensive description of wind–driven ocean flow within a global ocean basin model with constraints from space geodetic observations, we may be able to accurately predict ocean currents, mass redistribution and their effect on polar motion.

Appendix A: Satellite Laser Ranging

In satellite laser ranging, a target satellite is illuminated with a very short pulse (a few hundred picoseconds) of laser light and the time required for the reflected light to return is measured. This two–way travel time is a function of the distance from the ground–based laser to the satellite and the speed of light. A special class of satellites have been designed and launched to serve as passive SLR targets for geodetic and geodynamic applications. These SLR satellites are spherical and constructed of a dense core within an aluminum–alloy shell inlayed with small corner-cube reflectors. Their high mass to cross–sectional area ratio minimizes the effects of non–gravitational forces; e.g. atmospheric drag and solar/Earth radiation pressure.

The LAser GEOdynamics Satellite (Lageos) was placed in orbit on May 4, 1976 by NASA on a three–stage Delta–2913 launch vehicle. Lageos has a cylindrical, copper–beryllium core enclosed within an aluminum sphere of 0.29994 m radius. It has a total mass of 407.821 kg and is embedded with 426 corner–cube reflectors. Starlette was launched by Frances' Centre National d'Etudes Spatiale (CNES) in February, 1975. The satellite is a spherical, aluminum shell with a radius of 0.12 m, and covered with 60 corner–cube reflectors. A depleted uranium core helps bring Starlette's mass up to 47.295 kg.

The SLR laser systems are designed to provide 1 or 5 range measurements per second. This high data acquisition rate allows the compression of 2 to 3 minutes of data into laser "normal points" to improve the signal–to–noise ratio. Analysis has shown that this compression produces nearly noise–free data while adequately preserving all the geodetic information [Smith et al., 1985].

The range measurements are corrected for a number of factors; atmospheric refraction, light speed in the atmosphere, the distance from the satellite's center of mass to the reflection point on the satellite, optical path lengths of the sending/receiving telescopes and location of the laser relative to the station benchmark. Besides the range, the azimuth and elevation of the target satellite relative to the ground station are also noted and the range rate is estimated from the Doppler shift of the returning laser light. The station position is adjusted for Earth rotation, precession and nutation, for solid Earth tides and plate tectonic motion. The current accuracy of laser ranging is 1 cm though it varies from station to station.

Appendix B: Discussion of the Eccentricity Vector Ψ

If we define the eccentricity vector Ψ as $e \exp(-j\omega)$ [Yoder et al., 1983] then the time rate of change of Ψ, or the Ψ excitation, is:

$$\frac{d\Psi}{dt} = \frac{d\Psi}{de}\frac{de}{dt} + \frac{d\Psi}{d\omega}\frac{d\omega}{dt}$$

The Lagrangian planetary equations from Kaula [1966] for $d\omega/dt$ and de/dt are:

$$\frac{d\omega}{dt} = \frac{\cos i}{na^2(1-e^2)\sin i}\frac{\partial F}{\partial i} + \frac{(1-e^2)^{1/2}}{na^2 e}\frac{\partial F}{\partial e}$$

$$\frac{de}{dt} = \frac{(1-e^2)}{na^2 e}\frac{\partial F}{\partial M} - \frac{(1-e^2)^{1/2}}{na^2 e}\frac{\partial F}{\partial \omega}$$

where F is the force function. The force function is the difference between the satellite's kinetic energy T and the negative of potential energy V : $F = V - T$ [Kaula,1966]. If we are only interested in the long period orbital variations, i.e. variations with periods that are much longer than the orbital period, then we can ignore any dependence on M, the mean anomaly. Therefore we can take the $\partial F/\partial M$ term in de/dt to be zero. If the eccentricity is small, we can ignore the $\partial F/\partial i$ term in $d\omega/dt$ because the $\partial F/\partial \omega$ and $\partial F/\partial e$ terms are multiplied by e^{-1} and are thus much larger than the $\partial F/\partial i$. If the inclination is near 90°, the $\partial F/\partial i$ term is even less significant relative to $\partial F/\partial \omega$ and $\partial F/\partial e$ because it is multiplied by cos i. We can write the Ψ excitation as the combination of two major terms; the first derived from the expression for de/dt and the second derived from $d\omega/dt$:

$$\frac{d\Psi}{dt} = \left(-\frac{\left(1-e^2\right)^{1/2}}{na^2 e}\frac{\partial F}{\partial \omega}\right)\exp(-j\omega) \; - j\left(\frac{\left(1-e^2\right)^{1/2}}{na^2 e}\frac{\partial F}{\partial e}\right) e\exp(-j\omega) \qquad \text{(A1)}$$

The potential V is conventionally expressed as a series of spherical harmonic functions where an element of V is

$$V_{lm} = \frac{\mu a_e^l}{r^{l+1}} P_{lm}(\sin\phi)\left(C_{lm}\cos m\lambda + S_{lm}\sin m\lambda\right)$$

Kaula[1966] then rewrites V_{lm} into a form based on Keplerian orbital elements,

$$V_{lm} = \frac{\mu a_e^l}{a^{l+1}} \sum_{p=0}^{l} F_{lmp}(i) \sum_{q=-\infty}^{\infty} G_{lpq}(e)\, S_{lmpq}(\omega, M, \Omega, \theta)$$

where θ is Greenwich sidereal time. F, excluding the central body force, can be expressed in terms of the orbit elements and spherical harmonic coefficients as a product of three terms; $F_{lmp}(i)$, $G_{lpq}(e)$ and $S_{lmpq}(\omega, M, \Omega, \theta)$. The expression for $F_{lmp}(i)$ is

$$F_{lmp}(i) = \sum_{t} \frac{(2l-2t)!}{t!\,(l-t)!\,(l-m-2t)!\,2^{2l-2t}} \sin^{l-m-2t} i \sum_{s=0}^{m} \binom{m}{s} \cos^{s} i \sum_{c} \binom{l-m-2t+s}{c} \binom{m-s}{p-t-c} (-1)^{c-k}$$

where k is the integer part of $(l-m)/2$, t is summed from 0 to the lesser of p or k, and c is summed over all values that make the binomial coefficients nonzero. The binomial expansion is

$$\binom{m}{s} = \frac{m!}{s!\,(m-s)!}$$

$G_{lpq}(e)$ is

$$G_{lpq}(e) = (-1)^{|q|}\left(1+\beta^2\right)^{l} \beta^{|q|} \sum_{k=0}^{\infty} P_{lpqk}\, Q_{lpqk}\, \beta^{2k}$$

$$\beta = \frac{e}{1+\sqrt{1-e^2}}$$

$$P_{lpqk} = \sum_{r=0}^{h} \binom{2p' - 2l}{h-r} \frac{(-1)^r}{r!} \left(\frac{(l - 2p' + q')e}{2\beta} \right)^r$$

$$Q_{lpqk} = \sum_{r=0}^{h} \binom{-2p'}{h-r} \frac{1}{r!} \left(\frac{(l - 2p' + q')e}{2\beta} \right)^r$$

and $S_{lmpq}(\omega,M,\Omega,\theta)$ is

$$S_{lmpq} = \begin{bmatrix} C_{l,m} \\ -S_{l,m} \end{bmatrix}_{l-m\ \text{odd}}^{l-m\ \text{even}} \cos\left[(l-2p)\omega + (l-2p+q)M + m(\Omega-\theta)\right] + \begin{bmatrix} S_{l,m} \\ C_{l,m} \end{bmatrix}_{l-m\ \text{odd}}^{l-m\ \text{even}} \sin\left[(l-2p)\omega + (l-2p+q)M + m(\Omega-\theta)\right]$$

where $p' = p$ for $p \le l/2$ and $p' = l - p$ for $p \ge l/2$.

Because we are only interested in the long period variation, we must remove dependence of $S_{lmpq}(\omega,M,\Omega,\theta)$ on M. This occurs if the expression $(l - 2p + q)$ is equal to zero, i.e. when $2p - l$ is equal to q. In addition, we are only interested in the effect of the zonal harmonic coefficients; therefore m equals 0. Given these conditions, the expressions for $F_{lmp}(i)$, $G_{lpq}(e)$ and $S_{lmpq}(\omega,M,\Omega,\theta)$ simplify to

$$F_{l,0,p}(i) = \sum_{t} \frac{(2l-2t)!}{t!(l-t)!(l-2t)!\,2^{2l-2t}} \sin^{l-2t} i \sum_{c} \frac{(l-2t)!(-1)^{c-l/2}}{c!(l-2t-c)!(p-t-c)!(c+t-p)!} \quad \text{(A2)}$$

$$G_{l,p,2p-l}(e) = \frac{1}{(1-e^2)^{l-1/2}} \sum_{d=0}^{p'-1} \binom{l-1}{2d+l-2p'} \binom{2d+l-2p'}{d} \left(\frac{e}{2}\right)^{2d+l-2p'} \tag{A3}$$

$$S_{l=\text{even},0,p,2p-l}(\omega) = C_{l=\text{even},0} \cos(l-2p)\omega \tag{A4}$$

or

$$S_{l=\text{odd},0,p,2p-l}(\omega) = C_{l=\text{odd},0} \sin(l-2p)\omega \tag{A5}$$

Equation A1, the excitation of Ψ, can then be expanded into the expression:

$$\frac{d\Psi}{dt} = \left(-\frac{\left(1-e^2\right)^{1/2}}{na^2e} \frac{\mu}{a} \sum_{l=2}^{\infty} \left(\frac{a_e}{a}\right)^l \sum_{p=0}^{l} F_{l,0,p}(i)\, G_{l,p,2p-l}(e)\, \frac{\partial}{\partial \omega} S_{l,0,p,2p-l}(\omega) \right) \exp(-j\,\omega)$$

$$-j \left(\frac{\left(1-e^2\right)^{1/2}}{na^2e} \frac{\mu}{a} \sum_{l=2}^{\infty} \left(\frac{a_e}{a}\right)^l \sum_{p=0}^{l} F_{l,0,p}(i)\, \frac{\partial}{\partial e} G_{l,p,2p-l}(e)\, S_{l,0,p,2p-l}(\omega) \right) e\, \exp(-j\omega) \tag{A6}$$

The constraint that $2p - l$ is equal to q restricts the values that p can take for a degree l. In the summation for $V_{l,0}$, the limits for p run from 1 to $l-1$ because a $(-1)!$ appears in $G_{l,p,2p-l}(e)$ if p equals 0 or l. Consequently, restricting p to the interval 1 to $l-1$ constrains q to the interval $2-l$ to $l-2$. Table B shows $F_{l,0,p}(i)$, $G_{l,p,2p-l}(e)$ and $S_{l,0,p,2p-l}(\omega)$ for these conditions.

If eccentricity is very small then e^2 and higher powers of e are nearly zero and $(1-e^2) \approx 1$. The $(e/2)^{2d+l-2p'}$ expression in $G_{l,p,2p-l}(e)$ causes all terms in the $V_{l,0}$ summation to be very small except for those having $2d + l - 2p'$ equal 0 or 1; see equation A3 and Table B. For the odd degrees, the very small eccentricity also allows us to set as equivalent,

$$e\frac{\partial}{\partial e} G_{l,p,2p-l}(e) \approx G_{l,p,2p-l}(e)$$

because we can ignore all parts of $G_{l,p,2p-l}(e)$ that contain powers of e above 1.

A small eccentricity minimizes the even zonal harmonic contribution to the de/dt portion of dΨ/dt. Table B shows that all even degree terms in $V_{l,0}$ are scaled by powers of e except those with $p = l/2$ for which $S_{l=\text{even},0,l/2,2l-p}(\omega)$ is just $C_{l=\text{even},0}$. Thus $\partial S_{l=\text{even},m,p,q}(\omega)/\partial\omega$ is effectively zero for all the even zonal harmonic components of de/dt in dΨ/dt.

The simplifications discussed above define the only important terms in dΨ/dt as l = even, $m = 0$, $p = l/2$, $q = 0$ or l = odd, $m = 0$, $p = (l \pm 1)/2$, $q = \pm 1$. We can combine the odd zonal contributions of dω/dt with the de/dt portion of dΨ/dt and use $n = \mu^{1/2} a^{-3/2}$ to rewrite equation A6 as

$$\frac{d\Psi}{dt} \approx -\frac{n}{e}\sum_{l=\text{odd}}^{\infty}\left(\frac{a_e}{a}\right)^{l}\sum_{p=(l-1)/2}^{(l+1)/2} F_{l,0,p}(i)G_{l,p,2p-l}(e)\left(\frac{\partial}{\partial\omega}S_{l,0,p,2p-l}(\omega) + j\, S_{l,0,p,2p-l}(\omega)\right)\exp(-j\,\omega)$$

$$-j\left(\frac{n}{e}\sum_{l=\text{even}}^{\infty}\left(\frac{a_e}{a}\right)^{l} F_{l,0,l/2}(i)\frac{\partial}{\partial e}G_{l,l/2,2p-l}(e)\, S_{l,0,l/2,2p-l}(\omega)\right) e\exp(-j\,\omega) \qquad \text{(A7)}$$

dΨ/dt is separated, in equation A7, into two major terms: a first term containing all the odd zonal harmonic coefficients and a second term containing only even zonal harmonic coefficients. The even zonal harmonic portion of dΨ/dt is simply the secular change in ω ($\dot{\omega}_0$) because the periodic elements in dω/dt, the sin$\pm\omega$ terms in the odd zonal harmonic contribution, have been relocated:

$$\frac{n}{e}\sum_{l=\text{even}}^{\infty}\left(\frac{a_e}{a}\right)^{l} F_{l,0,l/2}(i)\frac{\partial}{\partial e}G_{l,l/2,2p-l}(e)\, S_{l,0,l/2,2p-l}(\omega) \approx \dot{\omega}_0$$

Table B shows that the odd zonal harmonic terms with q coefficients of $(l+1)/2$ and $(l-1)/2$ are equal:

$$F_{l,0,(l+1)/2}(i)\, G_{l,(l+1)/2,1}(e)\sin -\omega = F_{l,0,(l-1)/2}(i)\, G_{l,(l-1)/2,-1}(e)\sin\omega$$

and can be combined, allowing us to rewrite equation A7 as

$$\frac{d\Psi}{dt} \approx -\frac{n}{e}\sum_{l=odd}^{\infty}\left(\frac{a_e}{a}\right)^{l} 2F_{l,0,(l+1)/2}(i)\, G_{l,(l+1)/2,1}(e)\,(C_{l,0}\cos\omega + j\, C_{l,0}\sin\omega)\exp(-j\omega) - j\dot{\omega}_0\Psi$$

Rewriting $\cos\omega + j\sin\omega$ as $\exp(j\omega)$:

$$\frac{d\Psi}{dt} \approx -\frac{n}{e}\sum_{l=odd}^{\infty}\left(\frac{a_e}{a}\right)^{l} 2F_{l,0,(l+1)/2}(i)\, G_{l,(l+1)/2,1}(e)\, C_{l,0}\exp(j\omega)\exp(-j\omega) - j\dot{\omega}_0\Psi$$

Multiplying $\exp(j\omega)$ and $\exp(-j\omega)$:

$$\frac{d\Psi}{dt} \approx -\frac{n}{e}\sum_{l=odd}^{\infty}\left(\frac{a_e}{a}\right)^{l} 2F_{l,0,(l+1)/2}(i)\, G_{l,(l+1)/2,1}(e)\, C_{l,0} - j\dot{\omega}_0\Psi$$

We can replace $C_{l,0}$ by $-J_l$ which consists of a constant part J_l plus a time–variable perturbation, δJ_l. By rearranging terms, we can rewrite Ψ excitation as

$$\frac{d\Psi}{dt} + j\dot{\omega}_0\Psi \approx \frac{n}{e}\sum_{l=odd}^{\infty}\left(\frac{a_e}{a}\right)^{l} 2F_{l,0,(l+1)/2}(i)\, G_{l,(l+1)/2,1}(e)(\bar{J}_l + \delta J_l)$$

Since e^2 and higher powers of e are very close to zero and $(1-e^2)$ is very close to one, we can simplifiy $G_{l,(l+1)/2,1}(e)$ by reducing the $(1-e^2)^{-(l-1/2)}$, binomial and exponential terms in equation A3 to 1, $(l-1)$ and $e/2$ respectively. By dropping J_l and substituting $e(l-1)/2$ for $G_{l,(l+1)/2,1}(e)$, we can arrive at equation 3.2.2 in Sec 3.2.3;

$$\frac{d\Psi}{dt} + j\dot{\omega}_0\Psi \approx n(l-1)\sum_{l=odd}^{\infty}\left(\frac{a_e}{a}\right)^{l} F_{l,0,(l+1)/2}(i)\,\delta J_l$$

where the odd zonal portion of $d\Psi/dt$ is real and the coefficients, $f_{l=odd}$, for the δJ_l are

$$f_{l=odd} = n(l-1)\left(\frac{a_e}{a}\right)^{l} F_{l,0,(l+1)/2}(i)$$

Similar expressions are presented as equations 21-23 in Yoder et al. [1983], and equations 4 and 5 in Cheng et al.[1989]; however equation 23 in Yoder et al.[1983] is incorrect. The f_l can be computed from Table B or equation A2.

Table B. $F_{l,0,p}(i)\, G_{l,p,2p-l}(e) S_{l,0,p,2p-l}(\omega)$

$l\ m\ p\ q$	$F_{l,0,p}(i)\, G_{l,p,2p-l}(e) S_{l,0,p,2p-l}(\omega)$
2 0 1 0	$\left(\frac{3}{4}\sin^2 i - \frac{1}{2}\right)\left(1-e^2\right)^{-3/2} C_{2,0}$
3 0 1-1, 3 0 2 1	$\left(\frac{15}{16}\sin^3 i - \frac{3}{4}\sin i\right) e\left(1-e^2\right)^{-5/2} C_{3,0} \sin\omega$
4 0 1-2, 4 0 3 2	$\left(-\frac{35}{32}\sin^4 i + \frac{15}{16}\sin^2 i\right)\frac{3}{4}e^2\left(1-e^2\right)^{-7/2} C_{4,0} \cos 2\omega$
4 0 2 0	$\left(\frac{105}{64}\sin^4 i - \frac{15}{8}\sin^2 i + \frac{3}{8}\right)\left(\frac{3}{2}e^2+1\right)\left(1-e^2\right)^{-7/2} C_{4,0}$
5 0 1-3, 5 0 4 3	$\left(-\frac{315}{256}\sin^5 i + \frac{35}{32}\sin^3 i\right)\frac{1}{2}e^3\left(1-e^2\right)^{-9/2} C_{5,0} \sin 3\omega$
5 0 2-1 5 0 3 1	$\left(\frac{315}{128}\sin^5 i - \frac{105}{32}\sin^3 i + \frac{15}{16}\sin i\right)\left(\frac{3}{2}e^3+2e\right)\left(1-e^2\right)^{-9/2} C_{5,0} \sin\omega$
6 0 1-4, 6 0 5 4	$\left(\frac{693}{512}\sin^6 i - \frac{315}{256}\sin^4 i\right)\frac{5}{16}e^4\left(1-e^2\right)^{-11/2} C_{6,0} \cos 4\omega$
6 0 2-2, 6 0 4 2	$\left(-\frac{3465}{1024}\sin^6 i + \frac{315}{64}\sin^4 i - \frac{105}{64}\sin^2 i\right)\left(\frac{5}{4}e^4+\frac{5}{2}e^2\right)\left(1-e^2\right)^{-11/2} C_{6,0} \cos 2\omega$
6 0 3 0	$\left(\frac{1155}{256}\sin^6 i - \frac{945}{128}\sin^4 i + \frac{105}{32}\sin^2 i\right)\left(\frac{15}{8}e^4+5e^2+1\right)\left(1-e^2\right)^{-11/2} C_{6,0}$
7 0 1-5, 7 0 6 5	$\left(\frac{3003}{2048}\sin^7 i - \frac{693}{512}\sin^5 i\right)\frac{3}{16}e^5\left(1-e^2\right)^{-13/2} C_{7,0} \sin 5\omega$
7 0 2-3, 7 0 5 3	$\left(-\frac{9009}{2048}\sin^7 i + \frac{3465}{512}\sin^5 i - \frac{315}{128}\sin^3 i\right)\left(\frac{15}{16}e^5+\frac{5}{2}e^3\right)\left(1-e^2\right)^{-13/2} C_{7,0} \sin 3\omega$

Table B(con't). $F_{l,0,p}(i)\ G_{l,p,2p-l}(e)S_{l,0,p,2p-l}(\omega)$

$l\ m\ p\ q$	$F_{l,0,p}(i)\ G_{l,p,2p-l}(e)S_{l,0,p,2p-l}(\omega)$
7 0 3-1, 7 0 4 1	$\left(\frac{15015}{2048}\sin^7 i - \frac{3465}{256}\sin^5 i + \frac{945}{128}\sin^3 i - \frac{35}{32}\sin i \right)\left(\frac{15}{8}e^7 + \frac{15}{2}e^5 + 3e \right)$ $\left(1 - e^2\right)^{-13/2} C_{7,0}\sin\omega$

Appendix C: Error Analysis of Zonal Coefficients

Zonal spherical harmonic coefficients of degree 2 and higher are estimated from various air pressure data, but this does not imply that the atmosphere has no degree 1 component. The most distinct seasonal air pressure anomalies are the winter–summer pressure fluctuations in the northern and southern hemispheres and over Eurasia, North America and the northern Pacific. The resulting variations in air mass across the equator, and between the eastern and western hemispheres create $a_{1,0}$, $a_{1,1}$ and $b_{1,1}$ coefficients with amplitudes comparable to the higher degree zonals. Average monthly values for $a_{1,0}$, $a_{1,1}$ and $b_{1,1}$, estimated from Navy surface pressure anomalies, are shown in Table C1. Also shown are the associated shifts in the earth's center of mass and changes in the mass of the atmosphere due to water vapor content.

Navy Sea Level Pressure Long Period Trend

When using the output from a computer model a paramount concern is whether the model results are a reasonable estimation of a real phenomena. Since I was interested in seasonal variations I was concerned about long period biases in the sea level pressure values. To search for biases in the Navy pressure values I computed the zonal pressure anomalies (average pressure anomaly at each latitude) by averaging pressure values along lines of constant latitude. Each latitude band was then weighted by its relative area; 1 at the equator diminishing to zero at the poles. I then low pass filtered this time series of zonal pressure anomalies from 1976–1983 by integrating along time. See Figure C. If unbiased, the integrated zonal pressure series should be near zero through time. Figure C shows, however, that the integerated Navy pressure values contain a marked trend in the southern hemisphere with a period of roughly ten

Table C1. Navy Average Monthly 1st Order Spherical Harmonic Coefficients, Change in Earth Center of Mass and Variation in Atmospheric Mass

	a(1,0) mbar	a(1,1) mbar	b(1,1) mbar	δZ meter	δX meter	δY meter	Airmass kg
Jan	1.59804	0.01018	1.94621	0.00291	0.00002	0.00354	0.62983E+15
Feb	0.89434	-0.00162	1.57640	0.00163	0.00000	0.00287	1.45240E+15
Mar	0.62869	-0.00979	0.73704	0.00114	-0.00002	0.00134	0.97428E+15
Apr	0.49570	-0.01259	-0.69162	0.00090	-0.00002	-0.00126	0.45542E+15
May	-0.03476	-0.00210	-1.51336	-0.00006	0.00000	-0.00275	-0.47718E+15
Jun	-1.66302	0.00277	-1.94086	-0.00302	0.00001	-0.00353	-1.23130E+15
Jul	-2.60014	0.00624	-2.39166	-0.00473	0.00001	-0.00435	-0.40574E+15
Aug	-1.92969	0.00595	-1.67311	-0.00351	0.00001	-0.00304	-0.66840E+15
Sep	-0.57667	0.00293	-0.18558	-0.00105	0.00001	-0.00034	-0.35485E+15
Oct	0.79325	0.00236	0.79566	0.00144	0.00000	0.00145	-0.52250E+15
Nov	1.04716	-0.00139	1.40458	0.00190	0.00000	0.00255	-0.05971E+15
Dec	0.98088	-0.00432	1.87038	0.00178	-0.00001	0.00340	0.37906E+15

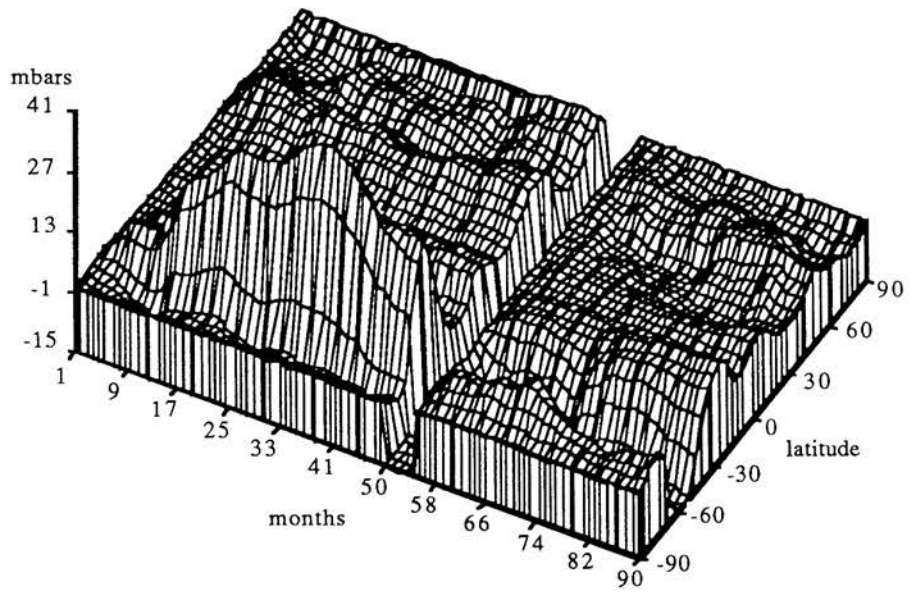

Figure C. The integrated zonal Navy surface pressure for 1976–1983 in mbar. Zonal pressures were computed by averaging surface pressures along latitude. The annual and semi–annual components of the pressure field have been removed and the oceans are assumed to non–isostatic. Resulting time series of zonal pressure variations was integrated to bring out any bias in zonal pressure. Large fluctuation in zonal pressure is evident along the 60°S latitude.

years and an amplitude of about 25 mbars. This trend, an apparent artifact of the model, is centered on latitude 60°S; the circum-Antarctic region where the Navy model is constrained by few observations.

Error modeling of WMO zonal harmonic coefficients

No error analysis was attempted for the Navy zonal coefficients since the pressure values were generated by a Navy meterological model and any analysis requires an evaluation of the model. The error analysis of the WMO zonal harmonic coefficients attempted to answer two questions: If I have perfect data, how well can I recover the true zonal coefficients given the uneven distribution of WMO stations about the globe? Second, what is the contribution of noise (e.g. wrong station coordinates, bad pressure values) to the WMO zonal harmonic coefficients? To answer these questions, a Monte Carlo scheme was employed to estimate the error variance due to the uneven sampling of the sphere and the error variance due to random noise in the data.

To estimate the error due to the irregular distribution of WMO stations, I decided to see how well I could recover any arbitrary set of zonal coefficients from station pressure values computed from these zonals. This involved generating a realistic but random set of zonal coefficients J_l , computing the pressure values at each WMO station from these coefficients, estimating a second set of zonal coefficients J'_l from these perfect data and then finding the difference between the original and estimated zonal coefficients, $J_l - J'_l$. A random set zonal coefficients were created from a series of random numbers generated by the FORTRAN function RANF. RANF produces numbers which are evenly distributed between zero and 1 and with a mean of 0.5. The variance of such a series of random numbers is:

$$\sigma^2 = \int_0^1 (x - \frac{1}{2})^2 \, dx = \frac{1}{12}$$

This relationship shows that by adding groups of 12 random numbers and subtracting the constant 6, one can create an approximately Gaussian set of random numbers with a zero mean and unit variance [Hamming, 1972]. Thus, a normal set of random numbers, J_l, with a zero mean and an arbitrary variance σ^2_l can be approximated using the algorithm:

$$J_l = \sum_{n=1}^{12\sigma_l^2} r_n - 6\sigma_l^2$$

where r_n is a random number generated by RANF and σ^2_l has been rounded to the nearest whole number. 101 random sets of zonal coefficients, J_2 through J_{20}, were generated so that each series of 101 zonal coefficients would have the same variance, σ^2_l, as the corresponding Navy zonal coeffficients. This constrained the random coefficients to realistic values. Table C2 lists the standard deviation and mean of the WMO, Navy and Navy(ib) zonal coefficients. The surface pressure was computed at each WMO station location from each set of random zonal coefficients using the Legendre coefficients, P(cosθ):

$$\text{Pressure}(\theta,\lambda) = \sum_{l=2}^{20} J_l \bullet P(\cos\theta)$$

A set of zonal coefficients, J'_2 through J'_{20}, were then solved for using these pressure values and the difference between the original J_l and the estimated J'_l was computed. With 101 samples of $J_l - J'_l$, the variance of the sampling error for each degree is $\sigma^2_{S(l)} = (J_l - J'_l)^2/100$. If I assume a normal distribution for $J_l - J'_l$, then the 95% confidence interval for $\sigma^2_{S(l)}$ can be computed from a table of the chi–square distribution. For (n -1) degrees of freedom, in this case 100, the probability is 95% that the true value of $\sigma^2_{S(l)}$ lies in the interval:

$$0.772\sigma^2_{S(l)} \leq \sigma^2_{S(l)} \leq 1.348\sigma^2_{S(l)}.$$

Table C2. Standard Deviation of Air Pressure Zonal Coefficient Time Series in mbar

	WMO (1976–1985)		Navy (1976–1983)		Navy(ib) (1976–1983)	
l	σ_l	Mean	σ_l	Mean	σ_l	Mean
2	2.0042	.0084	2.6127	-.0440	1.3223	-.0261
3	4.8115	-.1185	3.4941	-.0589	1.6954	-.0418
4	2.6333	-.0077	3.4699	-.0557	1.8273	-.0306
5	2.5440	-.0667	3.5084	-.0146	1.5745	.0081
6	2.7248	.0487	2.7927	-.0049	1.4422	.0269
7	2.4545	-.1016	2.7547	.0336	1.5075	.0330
8	1.7316	.0739	2.6042	.0513	1.3503	.0239
9	3.4650	-.1199	2.5105	.0437	1.4159	.0209
10	1.5078	.0331	2.0342	.0133	1.1886	.0086
11	1.5055	-.0057	2.0380	-.0113	1.0577	.0008
12	1.1133	-.0635	1.4905	-.0118	.9512	-.0092
13	1.8732	.0434	1.4013	-.0067	1.0060	-.0122
14	1.4016	-.1368	1.3390	-.0083	.9430	-.0134
15	1.9272	-.0383	1.2078	.0019	.9445	-.0058
16	1.1386	-.1985	1.1154	.0122	.7755	-.0021
17	1.3449	.1029	.9700	.0172	.8308	.0027
18	1.0661	.0261	.8204	.0018	.6703	-.0006
19	.9407	.0708	.7514	-.0023	.6494	-.0005
20	1.0487	-.0123	.6790	-.0024	.6480	-.0038

Since about $99^{3/4}\%$ of the values in a normal distribution will lie within the $\pm 3\sigma$ interval, there is about a 95% probability (the product of 95% and $99^{3/4}\%$) that $\pm 3(1.348\sigma^2_{S(l)})^{1/2}$ or $\pm 3.5\sigma_{S(l)}$ defines the range of the zonal coefficient error due to uneven data sampling on the sphere, assuming sampling errors are normally distributed.

The noise error was similarly estimated. Since the noise level in the WMO data is unknown, I modelled the worst case whereupon the WMO station pressures within any given month are spatial uncorrelated. I created a spatially uncorrelated series of pressure values for a set of WMO stations by taking a series of random numbers generated by the RANF function and mapping them into the probability distribution function (the integral of the probability density function) for the actual WMO surface pressures. This mapping was done in the following manner: The RANF–generated random numbers have a flat distribution between zero and 1, therefore the value of the probability distribution function F(x) for any RANF–generated random number x is simply x itself; F(x) = x. To convert x to an air pressure, x was matched with nearest value of $F_{WMO}(p)$ (the WMO probability distribution) in Table C3. The corresponding pressure value, p, was then interpolated from Table C3. This resulted in a series of random pressure values with the same probability density function as the real WMO station pressures. Zonal coefficients were estimated for 101 sets of these values and the variance, $\sigma^2_{N(l)}$, computed for each degree. As in the analysis of sampling error, 100 degrees of freedom result in about a 95% probability that $\pm 3.5\sigma_{N(l)}$ defines the contribution of random errors in the WMO data to each zonal coefficient.

The number and distribution of WMO stations varied from year to year; therefore the sampling and noise error for each zonal coefficient was estimated at each year from 1976 to 1985. Tables C4 and C5 show the estimated standard deviation for the

sampling error $\sigma_{S(l)}$ and noise error $\sigma_{N(l)}$ for the WMO zonal coefficients. The combined sampling and noise error estimate, $\pm 3.5(\sigma_{S(l)} + \sigma_{N(l)})$, is shown in Table C6. The possible error increases as the number of stations decrease; 1985 has the fewest WMO stations and the largest estimated error limits. The error limit tends to be larger for the higher degree zonals, as one would expect, since the gaps in the WMO station distribution approach the wavelengths of the higher zonals in the southern hemisphere and the ocean regions. Keeping in mind the pessimistic assumptions used in this analysis, Table C6 shows that one can be confident in estimating $a_{2,0}$ through $a_{5,0}$ from WMO data, but that higher degrees are problematical.

Table C3. Smoothed WMO Air Pressure Probability Distribution Function, p in mbar

p	$F_{WMO}(p)$	p	$F_{WMO}(p)$	p	$F_{WMO}(p)$	p	$F_{WMO}(p)$
-50	.0000000E+00	-25	.6081018E-03	0	.5000000E+00	25	.9993919E+00
-49	.1275738E-04	-24	.6506264E-03	1	.6373672E+00	26	.9994344E+00
-48	.2551476E-04	-23	.7229182E-03	2	.7440019E+00	27	.9994940E+00
-47	.3827214E-04	-22	.7696953E-03	3	.8217199E+00	28	.9995535E+00
-46	.4677706E-04	-21	.8887642E-03	4	.8759217E+00	29	.9995918E+00
-45	.5953444E-04	-20	.1067367E-02	5	.9141811E+00	30	.9996173E+00
-44	.7229182E-04	-19	.1237466E-02	6	.9403422E+00	31	.9996598E+00
-43	.8930166E-04	-18	.1462846E-02	7	.9592019E+00	32	.9996896E+00
-42	.1020590E-03	-17	.1679722E-02	8	.9722144E+00	33	.9997193E+00
-41	.1190689E-03	-16	.1913607E-02	9	.9814890E+00	34	.9997406E+00
-40	.1488361E-03	-15	.2381378E-02	10	.9875616E+00	35	.9997576E+00
-39	.1658459E-03	-14	.3168083E-02	11	.9914568E+00	36	.9997831E+00
-38	.1786033E-03	-13	.4371529E-02	12	.9939232E+00	37	.9998086E+00
-37	.1913607E-03	-12	.6076765E-02	13	.9956285E+00	38	.9998214E+00
-36	.2168755E-03	-11	.8543192E-02	14	.9968319E+00	39	.9998342E+00
-35	.2423902E-03	-10	.1243845E-01	15	.9976186E+00	40	.9998512E+00
-34	.2594001E-03	-9	.1851096E-01	16	.9980864E+00	41	.9998809E+00
-33	.2806624E-03	-8	.2778557E-01	17	.9983203E+00	42	.9998979E+00
-32	.3104296E-03	-7	.4079810E-01	18	.9985372E+00	43	.9999107E+00
-31	.3401968E-03	-6	.5965776E-01	19	.9987625E+00	44	.9999277E+00
-30	.3827214E-03	-5	.8581890E-01	20	.9989326E+00	45	.9999405E+00
-29	.4082362E-03	-4	.1240783E+00	21	.9991112E+00	46	.9999532E+00
-28	.4465083E-03	-3	.1782801E+00	22	.9992303E+00	47	.9999617E+00
-27	.5060427E-03	-2	.2559981E+00	23	.9992771E+00	48	.9999745E+00
-26	.5655772E-03	-1	.3626328E+00	24	.9993494E+00	49	.9999872E+00
						50	.1000000E+01

Table C4. Estimated Standard Deviation of Sampling Error for WMO Zonal Coefficients

l	1976	1977	1978	1979	1980	1981	1982	1983	1984	1985
2	.018	.020	.013	.020	.014	.017	.021	.025	.020	.042
3	.024	.026	.020	.030	.019	.022	.027	.038	.034	.099
4	.044	.046	.033	.051	.028	.034	.046	.069	.060	.207
5	.048	.049	.039	.061	.036	.044	.054	.088	.072	.314
6	.071	.074	.050	.082	.042	.056	.077	.125	.103	.455
7	.071	.072	.054	.083	.053	.063	.075	.134	.106	.558
8	.087	.091	.060	.092	.054	.064	.085	.147	.119	.670
9	.074	.074	.057	.083	.055	.068	.076	.138	.105	.720
10	.090	.089	.061	.090	.054	.066	.086	.152	.123	.752
11	.078	.073	.058	.078	.052	.068	.074	.141	.108	.722
12	.105	.096	.077	.098	.069	.083	.086	.161	.126	.686
13	.090	.092	.083	.096	.073	.092	.092	.161	.119	.596
14	.105	.101	.080	.114	.074	.091	.100	.179	.137	.522
15	.093	.084	.078	.101	.074	.091	.094	.179	.136	.441
16	.109	.108	.073	.115	.073	.080	.099	.203	.158	.427
17	.100	.094	.088	.110	.083	.099	.092	.182	.145	.384
18	.125	.114	.103	.115	.094	.099	.106	.189	.156	.371
19	.111	.095	.097	.101	.096	.092	.093	.152	.127	.279
20	.097	.093	.082	.094	.082	.086	.099	.131	.121	.190
stations	1048	1058	1137	1122	1082	947	930	955	1001	845

Table C5. Estimated Standard Deviation of Noise Error for WMO Zonal Coefficients

l	1976	1977	1978	1979	1980	1981	1982	1983	1984	1985
2	.294	.330	.326	.309	.311	.290	.311	.330	.369	.438
3	.360	.442	.413	.355	.358	.383	.399	.369	.418	.749
4	.460	.527	.435	.454	.464	.402	.459	.515	.470	1.209
5	.566	.577	.597	.514	.483	.571	.457	.647	.616	1.384
6	.574	.541	.549	.667	.526	.522	.597	.698	.783	1.493
7	.736	.614	.597	.570	.544	.638	.611	.890	.843	1.358
8	.784	.785	.639	.612	.519	.756	.682	.785	.813	1.452
9	.722	.653	.654	.677	.600	.624	.729	.951	.830	1.286
10	.766	.708	.676	.677	.654	.650	.750	.951	.922	1.232
11	.752	.694	.695	.668	.764	.768	.757	.913	1.044	.984
12	.829	.872	.862	.700	.831	.788	.764	1.041	1.047	.848
13	.903	.973	.861	.770	.801	.978	.876	.925	.951	.903
14	.973	.897	.765	.782	.841	.829	.848	1.068	1.021	.919
15	.888	.774	.874	.795	.675	.783	.756	.918	.997	.911
16	.781	.828	.749	.724	.748	.738	.768	.945	.998	.844
17	.831	.915	.769	.676	.815	.833	.768	.929	.904	.907
18	.842	.813	.742	.692	.728	.886	.654	.882	1.000	.823
19	.906	.761	.751	.666	.716	.805	.879	.798	.889	.842
20	.710	.778	.653	.639	.791	.838	.743	.827	.786	.832
stations	1048	1058	1137	1122	1082	947	930	955	1001	845

Table C6. WMO Zonal Coefficient Error Limits in mbar at 95% Probability Level

Yr:	76-85	1976	1977	1978	1979	1980	1981	1982	1983	1984	1985
l	σ_l	$\pm 3.5(\sigma_{S(l)} + \sigma_{N(l)})$									
2	2.0	±1.1	±1.2	±1.2	±1.2	±1.1	±1.1	±1.2	±1.2	±1.4	±1.7
3	4.8	±1.3	±1.6	±1.5	±1.3	±1.3	±1.4	±1.5	±1.4	±1.6	±3.0
4	2.6	±1.8	±2.0	±1.6	±1.8	±1.7	±1.5	±1.8	±2.0	±1.9	±5.0
5	2.5	±2.1	±2.2	±2.2	±2.0	±1.8	±2.2	±1.8	±2.6	±2.4	±5.9
6	2.7	±2.3	±2.2	±2.1	±2.6	±2.0	±2.0	±2.4	±2.9	±3.1	±6.8
7	2.5	±2.8	±2.4	±2.3	±2.3	±2.1	±2.5	±2.4	±3.6	±3.3	±6.7
8	1.7	±3.0	±3.1	±2.4	±2.5	±2.0	±2.9	±2.7	±3.3	±3.3	±7.4
9	3.5	±2.8	±2.5	±2.5	±2.7	±2.3	±2.4	±2.8	±3.8	±3.3	±7.0
10	1.5	±3.0	±2.8	±2.6	±2.7	±2.5	±2.5	±2.9	±3.9	±3.7	±6.9
11	1.5	±2.9	±2.7	±2.6	±2.6	±2.9	±2.9	±2.9	±3.7	±4.0	±6.0
12	1.1	±3.3	±3.4	±3.3	±2.8	±3.2	±3.1	±3.0	±4.2	±4.1	±5.4
13	1.9	±3.5	±3.7	±3.3	±3.0	±3.1	±3.7	±3.4	±3.8	±3.7	±5.2
14	1.4	±3.8	±3.5	±3.0	±3.1	±3.2	±3.2	±3.3	±4.4	±4.1	±5.0
15	1.9	±3.4	±3.0	±3.3	±3.1	±2.6	±3.1	±3.0	±3.8	±4.0	±4.7
16	1.1	±3.1	±3.3	±2.9	±2.9	±2.9	±2.9	±3.0	±4.0	±4.0	±4.4
17	1.3	±3.3	±3.5	±3.0	±2.8	±3.1	±3.3	±3.0	±3.9	±3.7	±4.5
18	1.1	±3.4	±3.2	±3.0	±2.8	±2.9	±3.4	±2.7	±3.7	±4.0	±4.2
19	.9	±3.6	±3.0	±3.0	±2.7	±2.8	±3.1	±3.4	±3.3	±3.6	±3.9
20	1.0	±2.8	±3.0	±2.6	±2.6	±3.1	±3.2	±2.9	±3.4	±3.2	±3.6
stations		1048	1058	1137	1122	1082	947	930	955	1001	845

Bibliography

Chao, B. and W. O'Connor, Global surface-water-induced seasonal variations in the Earth's rotation and gravitational field, Geophys. J. R. astron. Soc., 94, 263-270, 1988.

Cheng, M. K., R. J. Eanes, C. K. Shum, B. E. Schutz and B. D. Tapely, Earth rotation solution from Starlette orbit analysis during the MERIT campaign, Proceedings of the International Conference on Earth Rotation and the Terrestrial Reference Frame, 1, 191-196, 1985.

Cheng, M. K., Time variations in the Earth's gravity field from Starlette orbit analysis, Ph.D dissertation, 193 pp., Univ. of Texas at Austin, Austin, May 1988.

Cheng, M. K., R. J. Eanes, C. K. Shum, B. E. Schutz and B. D. Tapely, Temporal variations in low degree zonal harmonics from Starlette orbit analysis, Geophys. Res. Lett.,16,393-396, 1989.

Christodoulidis, D. C., D. E. Smith, R. Kolenkiewcz, S. M. Klosko, M. H. Torrence, and P. J. Dunn, Observing tectonic plate motions and deformations from satellite laser ranging, J. Geophys. Res., 90, 9221–9233, 1985.

Ciufolini, I., Measurement of the Lense-Thirring drag on high-altitude laser-ranged artificial satellites, Phys. Rev. Lett., 56, 278-281, 1986.

Gill, A. and P. Niiler, The theory of the seasonal variability in the oceans, Deep Sea Research, 20, 141–177, 1973.

Greatbatch, R. and A. Goulding, Seasonal variations in a linear barotropic model of the North Pacific driven by the Hellerman and Rosenstein wind stress field, J. Geophys. Res., 94, 12645-12665, 1989.

Gutierrez, R. and C. R. Wilson, Seasonal air and water mass redistribution effects on Lageos and Starlette, Geophys. Res. Lett., 14, 929-932, 1987.

Hamming, R. W., Numerical Methods for Engineers and Scientist, 271pp., Dover Publishing, New York, 1972.

Hellerman, S. and M. Rosenstein, Normal monthly wind stress over the world ocean with error estimates, J. Phys. Ocean., 13, 1093-1104, 1983.

Jeffreys, H., Causes contributory to the annual variation of latitude, Mon. Not. R. astron. Soc., 76, 499, 1916.

Kaula, W. M., Theory of Satellite Geodesy, 124 pp., Blaisdell Publishing, Waltham, Mass., 1966.

Koopman, L. H., Spectral Analysis of Time Series, 360 pp., Academic Press, New York, N.Y., 1974.

Kuehne, J. W., Water storage contributions to the excitation of polar motion, M.A. thesis, 95 pp., Univ. of Texas at Austin, Austin, May 1989.

Lambeck, K., The Earth's Variable Rotation: Geophysical Causes and Consequences, 449 pp., Cambridge University Press, Cambridge, 1980.

Longman, A., Green's function for determining the deformation of the Earth under surface mass loads - 2. computations and numerical results, J. Geophys. Res., 68, 485-496, 1963.

McCarthy, D. D. and others, IERS Standards (1989), IERS Technical Note No. 3, Paris, 1989.

Melbourne, W., R. Anderle, M. Feissel, R. King, D. McCarthy, D. Smith, B. Tapley and R. Vincente, Project Merit Standards, United States Naval Observatory Circular No. 167, Washington D. C., 1983.

Merriam, J. B., Lageos and UT measurements of long-period Earth tides and mantle Q, J. Geophys. Res., 90, 9423-9430, 1985.

Minster, J. B. and T. H. Jordan, Present–day plate motions, J. Geophys. Res., 83, 533-5354, 1978.

O'Connor, W. P., Estimate of wind stressed sea level excitation of the Earth's annual wobble, Geophys. J. R. astron. Soc., 60, 187-207, 1980.

Patullo, J., W. Munk, R. Revelle and E. Strong, The seasonal oscillation in sea level, J. mar. Res., 14, 88-1955, 1955.

Peltier, W. R., The Lageos constraints on deep mantle viscosity: results from a new normal mode method for the inversion of viscoelastic relaxation spectra, J. Geophys. Res. , 90, 9411-9421, 1985.

Rasmussen, E. M. and J. M. Wallace, Meteorological aspects of the El Niño/Southern Oscillation, Science, 222,1195-1202, 1983.

Ries, J. C., R. J. Eanes, C. Huang, B. E. Schutz, C. K. Shum, B. D. Tapley, M. M. Watkins, and D. N. Yuan, Determination of the gravitational coefficient of the Earth from near–Earth satellites, Geophys. Res. Lett., 16, 271-274, 1989.

Rubincam, D. P., Lageos orbit decay due to infared radiation from Earth, J. Geophys. Res., 92, 1287-1294, 1987.

Smith, D. E., D. C. Christodoulidis, R. Kolenkiewcz, P. J. Dunn, S. M. Klosko, M. H. Torrence, S. Fricke and S. Blackwell, A global reference frame from Lageos ranging (SL5.1AP), J. Geophys. Res., 90, 9221–9233, 1985.

Stolz, A., M. A. Vincent, P. L. Bender, R. A. Eanes, M. M. Watkins, and B. D. Tapley, Rate of change of the Quincy-Monument Peak baseline from a translocation analysis of Lageos laser range data, Geophys. Res. Lett., 16, 539-542, 1989.

Tapley, B. D., B. E. Schutz and R. J. Eanes, Station coordinates, baselines and Earth rotation from Lageos laser ranging,: 1976-1984, J.Geophys. Res., 90, 9235-9248, 1985.

Tapley, B. D., B. E. Schutz, C. K. Shum, J. C. Ries and D. N. Yuan, The TOPEX gravity model: a status report (abstract), Eos Trans. AGU, 67, 261, 1986.

Thompson, D. J., Spectrum estimation and harmonic analysis, Proceed. of the IEEE, 70, 1055–1096, 1982.

Trenberth, K. E., J. R. Christy and J. G. Olson, Global atmospheric mass, surface pressure and water vapor variations, J. Geophys. Res. , 92, 14815-14826, 1987.

UNESCO, World Water Balance and Water Resources of the Earth, 65 map sheets, UNESCO Press, Paris, 1978.

Vincent, M. A., The determination of the post-Newtonian parameters in gravitational theory using laser ranging to the Lageos satellite, Ph.D. dissertation, 212 pp., Univ. of Texas at Austin, Austin, May 1984.

Wahr, J. M., The effects of the atmosphere and oceans on the Earth's rotation, Geophys. J. R. astron. Soc., 70, 349-372, 1982.

Wahr, J. M., The effects of the atmosphere and oceans on the Earth's wobble and on the seasonal variations in the length of day - II results, Geophys. J. R. astron. Soc., 74, 4511-487, 1983.

Watkins, M. M., Tracking station coordinates and their temporal evolution as determined from laser ranging to the Lageos satellite, Ph. D. dissertation, 145 pp., Univ. of Texas at Austin, Austin, May 1990.

Webster, I., Frictional continental shelf waves and the circulation response of a continental shelf to wind forcing, J. Phys. Ocean., 15, 855-864, 1985.

Wilson, C. R. and R. A. Haubich, Atmospheric contributions to the excitation of the Earth's wobble 1901-1970, Geophys. J. R. astr. Soc., 46, 745-760, 1976.

Wilson, C. R., Discrete polar motion equations, Geophys. J. R. astron. Soc., 80, 551–554, 1985.

Yoder, C. F., J. G. Williams, J. O. Dickey, B. E. Schutz, R. J. Eanes and B. D. Tapley, Secular variation of Earth's gravitational harmonic J_2 coefficient from Lageos and nontidal acceleration of Earth rotation, Nature, 303, 757-762, 1983.

This digitized document does not include the vita page from the original.